

MAY 26 1972

AEDC-TR-72-56

cy.2

Jim Uselton



**DAMPING-IN-PITCH AND DRAG CHARACTERISTICS
OF THE VIKING CONFIGURATION
AT MACH NUMBERS FROM 1.6 THROUGH 3**

Bob L. Uselton and Arthur R. Wallace

ARO, Inc.

May 1972

Approved for public release; distribution unlimited.

**VON KÁRMÁN GAS DYNAMICS FACILITY
ARNOLD ENGINEERING DEVELOPMENT CENTER
AIR FORCE SYSTEMS COMMAND
ARNOLD AIR FORCE STATION, TENNESSEE**

PROPERTY OF U.S. AIR FORCE
AEDC LIBRARY
JAN 10 1973

NOTICES

When U. S. Government drawings specifications, or other data are used for any purpose other than a definitely related Government procurement operation, the Government thereby incurs no responsibility nor any obligation whatsoever, and the fact that the Government may have formulated, furnished, or in any way supplied the said drawings, specifications, or other data, is not to be regarded by implication or otherwise, or in any manner licensing the holder or any other person or corporation, or conveying any rights or permission to manufacture, use, or sell any patented invention that may in any way be related thereto.

Qualified users may obtain copies of this report from the Defense Documentation Center.

References to named commercial products in this report are not to be considered in any sense as an endorsement of the product by the United States Air Force or the Government.

DAMPING-IN-PITCH AND DRAG CHARACTERISTICS
OF THE VIKING CONFIGURATION
AT MACH NUMBERS FROM 1.6 THROUGH 3

Bob L. Usselton and Arthur R. Wallace
ARO, Inc.

Approved for public release; distribution unlimited.

FOREWORD

The work reported herein was sponsored by the National Aeronautics and Space Administration (NASA), Langley Research Center, Hampton, Virginia. The test program was conducted for the Martin-Marietta Corporation, Denver Division, under Program Element 921E-5.

The results presented herein were obtained by ARO, Inc. (a subsidiary of Sverdrup & Parcel and Associates, Inc.), contract operator of the Arnold Engineering Development Center (AEDC), Air Force Systems Command (AFSC), Arnold Air Force Station, Tennessee, under Contract F40600-72-C-0003. The tests were conducted from June 21 to August 18, 1971, under ARO Project No. VT1170. The final data reduction was completed on November 22, 1971, and the manuscript was submitted for publication on February 7, 1972.

This technical report has been reviewed and is approved.

Emmett A. Niblack, Jr.
Lt Colonel, USAF
AF Representative, VKF
Directorate of Test

Frank J. Passarello
Colonel, USAF
Acting Director
Directorate of Test

ABSTRACT

Wind tunnel tests were conducted to substantiate earlier test results from another AEDC facility and to determine the dynamic stability characteristics of the Viking-Balloon Launched Decelerator Test (BLDT) configuration (0.0437-scale, 140-deg blunt conical model with base cover). Measurements were made with a free-oscillation dynamic balance as the model oscillated from ± 2.4 to ± 0.6 deg at angles of attack ranging from -3.5 to 15.2 deg. Data were obtained at nominal free-stream Mach numbers from 1.76 to 3 at free-stream Reynolds number, based on maximum model diameter, ranging from 0.25×10^6 to 1.49×10^6 . The effects of free-stream Mach number, Reynolds number, angle of attack, amplitude of oscillation, combined angle of attack and angle of yaw, reduced frequency parameter, sting diameter, effective sting length, and rocket motor nozzles on the damping-in-pitch derivatives are presented. The dynamic instabilities at zero angle of attack which were found during the previous tests were verified by the present tests. The sting support interference study showed significant variations of the damping derivatives with sting length and diameter at the lower Mach numbers, but the basic sting, used for the majority of the data acquisition, was judged to have little effect on the damping derivatives. The BLDT configuration was generally dynamically unstable at the lower Mach numbers for angles of attack between 0 and 2.5 deg, and the damping derivatives showed erratic behavior with variation of the test parameters at these conditions. For angles of attack of 3 to 15 deg at all Mach numbers, the BLDT configuration was dynamically stable, and the damping derivatives were generally independent of the test variables. In general, the presence of the BLDT rocket motor nozzles did not affect the damping-in-pitch derivatives. The damping derivatives also showed the same trends with yaw angle as with angle of attack. A free-flight test was also conducted on a 0.0146-scale BLDT configuration at the same free-stream test conditions as the sting support test to determine free-flight wake parameters and drag coefficients. A comparison of free-flight and sting-supported model wakes is made. The free-flight drag coefficients show good agreement with coefficients obtained from tests on a similar configuration with a sting-supported model.

CONTENTS

	<u>Page</u>
ABSTRACT	iii
NOMENCLATURE	viii
I. INTRODUCTION	1
II. APPARATUS	
2.1 Models	2
2.2 Instrumentation	3
2.3 Test Facilities	4
III. PROCEDURE	
3.1 Test Conditions	5
3.2 Test Procedure	5
3.3 Precision of Data	6
IV. RESULTS AND DISCUSSION	
4.1 Evaluation of Support Interference	8
4.2 Present Test Results	12
V. CONCLUSIONS	15
REFERENCES	16

APPENDIXES

I. ILLUSTRATIONS

Figure

1. Free-Flight Model Photographs	21
2. Nomenclature, Dynamic Stability Models	22
3. Photographs of Dynamic Stability Models	24
4. BLDT Installation Photographs (Tunnel A)	25
5. Config. 721M Model and Sting Geometry	26
6. BLDT Model and Sting Geometry	28
7. Comparison of Wind Tunnel and Approximate Flight Test Conditions	32
8. Shock and Wake Patterns in Free Flight, $\alpha \approx 0$	33
9. Typical Schlieren Photographs from Tunnel A, BLDT Config.	34

<u>Figure</u>	<u>Page</u>
10. Bow Shock Stand-Off Distance as a Function of Mach Number	38
11. Wake Diameter as a Function of Mach Number	39
12. Distance from Maximum Model Diameter to Minimum Wake Diameter as a Function of Mach Number	40
13. Damping-in-Pitch Derivatives as a Function of Sting Diameter, BLDT Config., $l_s/d = 3.55$	41
14. Damping-in-Pitch Derivatives as a Function of Sting Diameter, BLDT Config., $l_s/d = 1.50$	44
15. Effect of Sting Diameter on the Damping-in-Pitch Derivatives as a Function of Angle of Attack, $M_\infty = 1.76$, $Re_d \approx 0.26 \times 10^6$, $l_s/d = 3.55$	46
16. Effect of Sting Diameter on the Damping-in-Pitch Derivatives as a Function of Angle of Attack, $M_\infty = 1.76$, $Re_d \approx 0.26 \times 10^6$, $l_s/d = 1.50$	48
17. Damping-in-Pitch Derivatives as a Function of Sting Length, BLDT Config., $d_s/d = 0.183$	50
18. Damping-in-Pitch Derivatives as a Function of Sting Length, BLDT Config., $d_s/d = 0.530$	52
19. Effect of Sting Length on the Damping-in-Pitch Derivatives as a Function of Angle of Attack, BLDT Config., $M_\infty = 1.76$, $Re_d \approx 0.26 \times 10^6$, $d_s/d = 0.183$	54
20. Effect of Sting Length on the Damping-in-Pitch Derivatives as a Function of Angle of Attack, BLDT Config., $M_\infty = 1.76$, $d_s/d = 0.530$	56
21. Comparison of PWT and VKF Data at Various Angles of Attack, Config. 721M	57
22. Damping-in-Pitch Derivatives as a Function of Reynolds Number, Config. 721M	58
23. Comparison of PWT and VKF Data at Various Mach Numbers, Config. 721M	59
24. Drag Coefficient as a Function of Mach Number, BLDT Config.	60
25. Drag Coefficient as a Function of Reynolds Number, BLDT Config.	61

<u>Figure</u>	<u>Page</u>
26. Representative Damping Derivatives as a Function of Amplitude of Oscillation, θ	62
27. Damping-in-Pitch Derivatives as a Function of Angle of Attack, Config. 1000, $Re_d \approx 0.26 \times 10^6$	63
28. Damping-in-Pitch Derivatives as a Function of Angle of Attack, Config. 1000, $Re_d \approx 0.75 \times 10^6$	65
29. Damping-in-Pitch Derivatives as a Function of Angle of Attack, Config. 5000, $Re_d \approx 0.26 \times 10^6$	67
30. Damping-in-Pitch Derivatives as a Function of Angle of Attack, Config. 5000, $Re_d \approx 0.75 \times 10^6$	69
31. Damping-in-Pitch Derivatives as a Function of Angle of Attack, Config. 4000, $Re_d \approx 0.26 \times 10^6$	71
32. Damping-in-Pitch Derivatives as a Function of Reynolds Number, Config. 1000.	72
33. Damping-in-Pitch Derivatives as a Function of Reynolds Number, Config. 5000.	74
34. Damping-in-Pitch Derivatives as a Function of Reynolds Number, Config. 4000.	76
35. Damping-in-Pitch Derivatives as a Function of Mach Number	77
36. Damping-in-Pitch Derivatives as a Function of Reduced Frequency Parameter, BLDT Config., $\alpha \approx 0$	79
37. Damping-in-Pitch Derivatives as a Function of Reduced Frequency Parameter, BLDT Config., $\alpha \approx 6$ deg	82
38. Effect of Nozzles on Damping-in-Pitch Derivatives, BLDT Config., $Re_d \approx 0.25 \times 10^6$, $\omega d/2V_\infty \approx 0.007$	83
39. Effect of Nozzles on Damping-in-Pitch Derivatives, BLDT Config., $Re_d \approx 0.25 \times 10^6$, $\omega d/2V_\infty \approx 0.02$	85
40. Effect of Nozzles on Damping-in-Pitch Derivatives, BLDT Config., $Re_d \approx 0.75 \times 10^6$, $\omega d/2V_\infty \approx 0.02$	86
41. Damping-in-Pitch Derivatives as a Function of Yaw Angle, BLDT Config. 1090.	87

II. TABLES

I. Free-Flight Drag Data	89
II. Tunnel Conditions for Free-Flight Test	90
III. Dynamic Stability Test Summary	91
IV. Tunnel Conditions for Dynamic Stability Test	95

NOMENCLATURE

A	Reference area (based on maximum model diameter), ft ²
C _D	Drag coefficient, drag/q _∞ A
C _m	Pitching-moment coefficient, pitching moment/q _∞ Ad
C _{m_q}	$\left. \begin{array}{l} \partial C_m / \partial (qd / 2V_\infty) \\ \partial C_m / \partial (\dot{\alpha}d / 2V_\infty) \end{array} \right\}$ Damping-in-pitch derivatives, 1/radian
C _{m_{α̇}}	
d	Reference length (maximum model diameter), ft or in.
d _F	Sting-flare diameter (see Fig. 2), in.
d _S	Sting diameter (see Fig. 2), in.
d _w	Diameter of wake neck (see Fig. 8), in.
ℓ _S	Effective sting length (see Fig. 2), in.
ℓ _w	Horizontal distance from maximum model diameter to wake neck (see Fig. 8), in.
M _∞	Free-stream Mach number
p ₀	Tunnel stilling chamber pressure, psia
q	Pitching velocity, radians/sec
q _∞	Free-stream dynamic pressure, psia
Re _d	Free-stream Reynolds number based on maximum model diameter
s	Bow shock stand-off distance (see Fig. 8), in.
T ₀	Tunnel stilling chamber temperature, °R
V _∞	Free-stream velocity, ft/sec
x _{cg}	Distance from theoretical model nose to center of gravity (pivot axis) (see Fig. 2), in.

Z_{cg}	Center-of-gravity offset for free-flight models (see Table I, Appendix II), in.
Z_h	Mounting hole offset for free-flight models (see Table I, Appendix II), in.
z_{cg}	Distance from model centerline to center of gravity (pivot axis) (see Fig. 2), in.
α	Angle of attack, deg
$\dot{\alpha}$	Time rate of change of angle of attack, radians/sec
θ	Oscillation amplitude, deg
ϕ	Roll angle, deg
ψ	Yaw angle, deg
ω	Angular frequency, radians/sec
$\omega d/2V_\infty$	Reduced frequency parameter, radians

Note: Model configuration nomenclature is explained in Fig. 2.

SECTION I INTRODUCTION

During the past several years efforts have been directed toward the development of a planetary probe system capable of entering the atmosphere of Mars and landing a scientific payload. Although much of the extensive research and development effort expended on the reentry vehicles for the earth's atmosphere can be applied to the planetary exploration, major differences do exist. Primarily, these differences are the result of low atmospheric density, relative to that of the earth. Research and development groups have been engaged in evaluating the aerodynamic characteristics of the candidate shapes in air and then determining the effects of the Martian atmosphere on these aerodynamic characteristics. Several experimental tests have been conducted on planetary shapes to determine the static and dynamic aerodynamic characteristics for subsonic to hypersonic speeds (Refs. 1 through 15).

The Viking project is the NASA program for the exploration of the planet Mars using automated devices. NASA-Langley has been assigned Viking project management and also detailed responsibility for the overall spacecraft and the lander. The Martin-Marietta Corporation, Denver Division, will provide the lander and assist NASA-Langley in integrating the lander with the orbiter and the resulting spacecraft with the launch vehicle.

Previous dynamic stability tests (Ref. 16) have been completed in the Propulsion Wind Tunnel Facility (PWT) at AEDC in support of aerodynamic design programs conducted by NASA-Langley and Martin-Marietta Corporation on the blunt cone aeroshells. The test results of Ref. 16, at transonic and low supersonic Mach numbers, showed the Viking configuration to be unstable at zero angle of attack and exhibited a steep gradient of the damping coefficient over small changes in angle of attack for angles of attack near zero. In addition, a limited Reynolds number investigation showed pronounced Reynolds number effects at low angles of attack and erratic trends with Mach number. NASA-Langley also found apparent anomalies between the wind tunnel damping data and that deduced from PEPP (Planetary Entry Parachute Program) flight vehicle motion. Because of the unresolved questions concerning the data of Ref. 16 and the fact that the Balloon Launched Decelerator Test (BLDT) was planned to qualify the parachute recovery system, additional wind tunnel testing was performed. An analysis reported in Ref. 17 was also conducted on selected portions of the present data and the Ref. 16 data to extract local damping derivatives from finite amplitude data.

The present wind tunnel test program was conducted in the von Kármán Gas Dynamics Facility (VKF) in two phases. Phase I of the test program was a free-flight test of the BLDT configuration conducted in the 12-in. Supersonic Wind Tunnel (D) to determine free-flight wake characteristics. The purpose was to compare wake dimensions in the free-flight case with those for the sting-supported case in Supersonic Wind Tunnel (A) to obtain information on sting interference effects. Free-flight drag coefficients were also obtained.

Phase II of the test program consisted of sting-supported dynamic stability tests conducted in Tunnel A of VKF. There were two primary objectives. One was to test the model-sting configuration of Ref. 16 (configuration 721M) to verify that the instability at zero angle of attack did exist and was not caused by tunnel vibration. The second was to test the current BLDT configuration, which is similar to configuration 721M that was tested in PWT (Ref. 16), and to investigate the effects of Mach number, Reynolds number, angle of attack, amplitude of oscillation, reduced frequency parameter, combined angles of attack and yaw, and rocket motor nozzles on the dynamic stability derivatives.

The present tests were conducted on 140-deg included angle blunted cones at free-stream Mach numbers from 1.76 to 3 at free-stream Reynolds numbers (based on maximum model diameter) of 0.25×10^6 to 1.49×10^6 . Damping data were obtained at oscillation amplitudes of approximately ± 2.4 to ± 0.6 deg for an angle-of-attack range from -3.5 to 15.2 deg using a small-amplitude free-oscillation balance.

SECTION II APPARATUS

2.1 MODELS

2.1.1 Free Flight

The free-flight models (Fig. 1, Appendix I) were designed and fabricated at AEDC. The 2-in.-diam aluminum models were 0.0146-scale models of the Balloon Launched Decelerator Test (BLDT) vehicle, and each consisted of a 140-deg blunt cone forebody with a base cover containing four rocket motor nozzles. The models were tested with and without the rocket motor nozzles. The models had a 0.052-in.-diam transverse hole through the base cover for the support wire to pass through. Model geometry, which was the same as the BLDT dynamic stability model except for scale, can be found in the following section.

2.1.2 Dynamic Stability

The two dynamic stability models (configurations 721M and BLDT) were designed at AEDC and fabricated by an outside agency. The sting sleeves and flares were designed and fabricated by AEDC. Specific model configuration designations are shown in Fig. 2.

Configuration 721M was a 0.0435-scale model of the Viking vehicle. The 6-in. -diam stainless steel model consisted of a 140-deg blunted conical forebody with a base cover. This configuration with the sting-flare component (Fig. 3a) produced the same model-sting geometric relationship that was tested previously in the Propulsion Wind Tunnel (PWT) (Ref. 16) except for sting-model diameter ratio. The ratio of sting diameter to model diameter (d_s/d) was 0.0967 for the PWT tests and 0.183 for the present tests.

The BLDT model (Fig. 3b) was a 0.0437-scale version of the BLDT vehicle. The 6-in. -diam model was fabricated from Mallory®, a sintered tungsten alloy of high density ($\approx 0.614 \text{ lb/in.}^3$) to give a high moment of inertia, which helped to match the flight reduced frequency parameter. The BLDT model consisted of a 140-deg blunted conical forebody with a base cover which contained four rocket motor nozzles. The model was also tested without the nozzles. For the sting interference study, which was conducted without the rocket nozzles, aluminum sleeves (Fig. 4a) were fitted over the basic sting (Fig. 4b) to give d_s/d ratios of 0.350 and 0.530. The sting flare could be moved along the sting to give values of the ratio of effective sting length to model diameter (l_s/d) of 1.50 and 3.55.

Geometric details of the 721M and BLDT configurations and stings are shown in Figs. 5 and 6, respectively. For both models, provisions were made to add ballast to locate the model center of gravity at the balance pivot axis.

2.2 INSTRUMENTATION

2.2.1 Free Flight

All model data were obtained from two high-speed motion-picture cameras. Each camera was set for a frame rate of approximately 5000 per second. Timing marks were placed on the edge of the film every millisecond by an oscillator-controlled timing light so that the frame rate for each run could be determined very accurately.

One camera was set about 45 deg with respect to the tunnel center-line so that its view contained the model before and during release, as well as a portion of the free-flight path. Only qualitative data were obtained from this camera.

The second camera viewed the model flight through the tunnel schlieren system. In addition to obtaining shock and wake patterns, the film was read with a special optical reader to obtain model position. Model position was used with the timing marks to obtain velocity and acceleration.

2.2.2 Dynamic Stability

The dynamic stability balance (Ref. 18) is a small-amplitude one-degree-of-freedom, free-oscillation sting-supported system incorporating a cross-flexure pivot. A strain-gage bridge was located on the flexures to provide a voltage proportional to angular displacement. To protect the balance during injection into the airflow, the model was locked in position by a solenoid located in the aft portion of the sting.

If the model was stable, an oscillating air system was used to displace the model. The driving force was obtained from a high pressure air supply which was adjusted to the pressure level necessary to overcome the damping moment. The model was oscillated by a jet of air emitted from a tube by a remotely controlled servovalve oscillating at the natural frequency of the model balance system. The driving force could be stopped abruptly by a solenoid valve. If the model was unstable, then it was unlocked and data were recorded as the model amplitude increased.

2.3 TEST FACILITIES

Tunnel D, which was used for the free-flight tests, is an intermittent, variable density wind tunnel with a manually adjusted, flexible-plate-type nozzle and a 12- by 12-in. test section. The tunnel operates at Mach numbers from 1.5 to 5 at stagnation pressures from about 5 to 60 psia and at stagnation temperatures up to about 80°F.

Tunnel A, which was used for the dynamic stability tests, is a continuous, closed-circuit, variable density wind tunnel with an automatically driven, flexible-plate-type nozzle and a 40- by 40-in. test section. The tunnel can be operated at Mach numbers from 1.5 to 6 at maximum stagnation pressures from 29 to 200 psia, respectively, and at stagnation temperatures up to 750°R. Minimum stagnation pressures

range from about one-tenth to one-twentieth of the maximum pressure at each Mach number. Mach number changes may be made without stopping the tunnel in most instances. The model can be injected into the tunnel for a test run and then retracted for model changes without interrupting the tunnel flow.

SECTION III PROCEDURE

3.1 TEST CONDITIONS

Summaries of the model configurations and test conditions for the free-flight and dynamic stability test phases are presented in Tables I through IV of Appendix II. Comparisons of full-scale flight conditions and wind tunnel test conditions are shown in Fig. 7. The comparison indicates that data have been obtained covering the flight regime except near $M_\infty \approx 1.0$.

3.2 TEST PROCEDURE

3.2.1 Free Flight

The 2-in. -diam models were supported on the tunnel centerline upstream of the test section by a horizontal wire that ran through the model base cover. After the tunnel was started, the wire was broken at a notch inside the model. The wires were quickly and automatically withdrawn, leaving the model free. Before falling more than an inch, the model was blown past the test section where the motion was photographed through the tunnel schlieren system at approximately 5000 frames per second. The film was read to obtain model acceleration from which drag was calculated. The data reduction for the free-flight tests used the free-stream velocity referenced to the model.

3.2.2 Dynamic Stability

The test procedure for the damped oscillations was to set the forcing air pressure to a sufficiently high value, open the solenoid valve, adjust the frequency of the servovalve to the natural frequency of the model-balance system, and then, when the model amplitude reached the desired value, close the solenoid valve. The switch that closed the valve also started the high-speed scanner which read the digitized displacement signal onto magnetic tape for data reduction.

For the diverging oscillations the high-speed scanner was started after the model was unlocked.

Data reduction was accomplished by the logarithm decrement method described in Ref. 18. The logarithm of the peak amplitudes as a function of time was curve fitted with a third-degree least-square-error polynomial from 2.4 to 0.6 deg. For some data runs a condition existed such that amplitude reached a maximum value, and did not change, so the data were reduced over the amplitude range available.

3.3 PRECISION OF DATA

3.3.1 Tunnel Conditions

Uncertainties (bands which include 95 percent of the calibration data) in the basic tunnel parameters (Tunnels D and A), p_o , T_o , and M_∞ , were estimated from repeat calibrations of the instrumentation and from repeatability and uniformity of the test section flow during tunnel calibrations. These uncertainties were used to estimate uncertainties in other free-stream properties using a Taylor series method of error propagation (Ref. 19). The estimated uncertainties are shown below.

Test Condition		Uncertainty, percent					
M_∞	$Re_d \times 10^{-6}$	M_∞	p_o	T_o	q_∞	V_∞	Re_d
1.76	0.26	±0.9	±0.8	±0.4	±1.0	±0.6	±1.1
1.76	0.75	±0.9	±0.4	↓	±0.7	±0.6	±0.9
1.76	1.25	±0.9	±0.2	↓	±0.6	±0.6	±0.8
2.23	0.25	±0.5	±0.7	↓	±0.9	±0.3	±1.0
2.23	0.75	↓	±0.3	↓	±0.7	↓	±0.8
2.25	1.25	↓	±0.3	↓	±0.7	↓	±0.8
2.99	0.25	↓	±0.4	↓	±1.4	↓	±1.1
3.00	0.75	↓	±0.4	↓	±1.4	↓	±1.1
3.01	1.24	↓	±0.4	↓	±1.4	↓	±1.1

3.3.2 Free Flight

Based on the repeatability of the data and an analysis of possible errors in distance measurement, the precision of the drag coefficients is believed to be within ±6 percent. Errors from time measurement have been found to be negligible by comparison.

3.3.3 Dynamic Stability

The balance was calibrated before and after the tests, and check calibrations were made during the test. In addition, structural damping values were obtained at vacuum conditions before the tunnel entry to evaluate the still-air damping contribution. The uncertainties in the balance and data system were combined with uncertainties in the tunnel parameters, assuming a Taylor series error propagation (Ref. 19) to estimate the precision of the aerodynamic coefficients. The maximum uncertainties which occurred at the minimum Reynolds number are listed below.

M_∞	$C_{mq} + C_{m\dot{\alpha}}$	Uncertainty		
		Configs. 1BCD and 2BCD, $\Delta(C_{mq} - C_{m\dot{\alpha}})$	Configs. 3BCD, 5BCD, and 721M, $\Delta(C_{mq} + C_{m\dot{\alpha}})$	Configs. 4BCD and 6BCD, $\Delta(C_{mq} + C_{m\dot{\alpha}})$
1.76	8	± 0.11	± 0.12	± 0.13
	6	± 0.08	± 0.09	± 0.10
	4	± 0.06	± 0.06	± 0.07
	3	± 0.04	± 0.04	± 0.05
	2	± 0.03	± 0.03	± 0.04
	1	± 0.01	± 0.02	± 0.03
	0.5	± 0.007	± 0.014	± 0.031
	-0.5	± 0.009	± 0.018	± 0.035
2.25	4	± 0.05	± 0.05	± 0.06
	3	± 0.04	± 0.04	± 0.05
	2	± 0.02	± 0.03	± 0.04
	1	± 0.01	± 0.02	± 0.04
	0.5	± 0.006	± 0.017	± 0.038
	-0.5	± 0.010	± 0.022	± 0.042
3.00	-0.5	± 0.011	± 0.028	± 0.058

It should be noted that the above uncertainties do not apply to the data scatter obtained when the model was oscillating in regions where the coefficients have large gradients with angle of attack. However, the average value of the coefficients obtained during these conditions should be precise within the above uncertainties.

SECTION IV RESULTS AND DISCUSSION

4.1 EVALUATION OF SUPPORT INTERFERENCE

4.1.1 Comparison of Wakes from Free-Flight and Sting-Supported Models

Schlieren photographic coverage was obtained with the free-flight models in Tunnel D and the sting-mounted models in Tunnel A. Sketches of the bow shock and wake patterns in free flight presented in Fig. 8 were made from the high-speed schlieren motion pictures taken for drag data. The values of bow shock stand-off distance (s/d), minimum wake diameter (d_w/d), and wake length (ℓ_w/d) shown in Fig. 8 are typical, since there was virtually no effect of Reynolds number noted.

Schlieren photographs (Fig. 9) obtained in Tunnel A show the effects of sting length on the model wake geometry at Mach numbers 1.76 and 3. Similar photographs were used to obtain s , d_w , and ℓ_w , and the results are plotted with the free-flight measurements in Figs. 10, 11, and 12. As expected, there was little effect of the sting on shock stand-off distance (Fig. 10). No particular significance is attached to the slightly smaller s/d shown for the sting-mounted models, since this is within the scatter band.

As to wake diameter, the sting always forces the wake outward. The sting configuration and the Mach number had a large effect on the wake diameter (Fig. 11). The minimum sting diameter and maximum effective sting length, denoted by the squares, showed the least influence, as would be expected. At $M_\infty \approx 1.7$ sting diameter had only a small effect on wake geometry, and sting length had a large effect; at $M_\infty \approx 3.0$ sting length (within the range of the test) had no effect on the data for the large sting but had a considerable effect on the data for the small sting. Of course at $M_\infty \approx 3.0$ the wake minimum diameter in free flight was smaller than the larger sting diameter so that a considerable increase in wake diameter was necessary when the larger sting was installed. A considerable Reynolds number effect on wake diameter was found at $M_\infty \approx 2.2$ for the short sting configuration.

The free-flight wake length (Fig. 12) was substantially constant except for the lower end of the Mach number range for which a blown wake makes the length poorly defined. The slightly shorter wake lengths with the sting-mounted model occur because less length is required to contract to the larger wake diameters, assuming the same contraction angle.

The comparison of the bow shock stand-off distance, wake neck diameter, and wake length from the free-flight and sting-supported tests shows that the wake geometry was not changed substantially when the model was supported by the basic sting (Config. A000, $d_s/d = 0.183$, $\ell_s/d = 3.55$).

It is of interest to note that model instabilities occurred during the free-flight tests. The model, pre-positioned at an angle of attack of approximately zero on the support wire, would diverge in oscillation amplitude until a limit cycle was reached. The divergence usually occurred sometime during the tunnel start, but in some cases after the transients were over the model would be steady and then start to oscillate. The models that were positioned and released at an angle of attack did not diverge in amplitude during the tunnel start and also remained steady as tunnel stagnation pressure was raised.

4.1.2 Sting Effects on Pitch-Damping Coefficient

The sting interference study was conducted with the nozzles off. However, it is shown in Section 4.2.7 that the nozzles had no significant effect on the damping derivatives. Therefore, both nozzle-on ($A = 1, 4, 5$) and nozzle-off ($A = 2, 3, 6$) data are used for the sting effects data comparison. The stability derivatives at zero angle of attack for the BLDT configuration are shown in Fig. 13 as a function of the ratio of sting diameter to model diameter (d_s/d) and reduced frequency parameter for the longest effective sting length ($\ell_s/d = 3.55$). At $M_\infty = 1.76$, increasing d_s/d from 0.183 to 0.530 generally changed the dynamics of the BLDT configuration from an unstable configuration to a slightly stable configuration. At $M_\infty = 2.24$ the derivatives generally show less effect of d_s/d . Variation of d_s/d at $M_\infty = 3$ produced no effect on the damping derivatives. It should also be noted that at $M_\infty = 1.76$ (Fig. 13) the effects of sting diameter decreased as $\omega d/2V_\infty$ increased.

Figure 14 shows $C_{m_q} + C_{m_{\dot{\alpha}}}$ as a function of d_s/d at $\alpha \approx 0$ for an effective sting length ratio (ℓ_s/d) of 1.50. The effects of sting diameter on the dynamic derivatives for the shorter effective sting length ($\ell_s/d = 1.50$) are generally the same as found for the longer sting ($\ell_s/d = 3.55$, Fig. 13).

The effects of sting diameter on the damping derivatives as a function of angle of attack are shown in Figs. 15 and 16 for $\ell_s/d = 3.55$ and 1.50, respectively. For $\alpha \approx 3$ to 15 deg, variations of sting diameter for both sting lengths tested produced very little effect on the damping derivatives. For the angle-of-attack region near $\alpha = 0$ the effects of sting diameter on the damping derivatives are as discussed previously.

The dynamic stability derivatives for the BLDT configuration are shown in Figs. 17 and 18 for $d_s/d = 0.183$ and 0.530 , respectively, as functions of the ratio of effective sting length to model diameter and $\omega d/2V_\infty$. The damping trends shown in Fig. 17 are dependent upon Mach number, Reynolds number, and $\omega d/2V_\infty$. For $\omega d/2V_\infty \approx 0.009$ to 0.007 (Fig. 17a) the trends with ℓ_s/d at $M_\infty = 1.76$ are opposite those at $M_\infty \approx 2.24$ for $Re_d \approx 0.25 \times 10^6$. Also, in Fig. 17b ($M_\infty = 1.76$, $Re_d \approx 0.25 \times 10^6$) the trends of the dynamic derivatives for $\omega d/2V_\infty \approx 0.022$ are opposite those for $\omega d/2V_\infty \approx 0.009$ (Fig. 17a). The effects of ℓ_s/d at $M_\infty = 1.76$ also seemed to decrease with increasing $\omega d/2V_\infty$ (Fig. 17). At $M_\infty \approx 1.76$, $\alpha \approx 0$ for $d_s/d = 0.530$ (Fig. 18), the pitch derivatives generally increased slightly (greater stability) with increasing effective sting length, but at $M_\infty = 3$ (Figs. 17 and 18) no effect of ℓ_s/d was found for either d_s/d ratio.

Figures 19 and 20 show the effect of sting length on the dynamic derivatives as a function of angle of attack at $M_\infty = 1.76$ for d_s/d of 0.183 and 0.530 , respectively. For the angle-of-attack range from ≈ 3 to 15 deg, the damping derivatives generally showed approximately the same levels and trends for both effective sting lengths tested ($\ell_s/d = 1.50$ and 3.55), but for the near-zero-angle-of-attack region there are strong effects as discussed for Figs. 17 and 18.

In conclusion, the instability "spike" at $\alpha \approx 0$ does not appear to be a sting interference effect, since for $\ell_s/d = 1.50$ and 3.55 the instability decreased as the sting diameter increased. Also, the instabilities noted during the free-flight tests help to substantiate this conclusion. Support interference effects also seem to decrease with increasing $\omega d/2V_\infty$. The dynamic stability derivatives for angles of attack from 3 to 15 deg were not significantly affected by support interference. At the near-zero-angle-of-attack region support interference did affect the dynamic stability derivatives. The amount of support interference produced by the basic sting arrangement ($d_s/d = 0.183$ and $\ell_s/d = 3.55$) at $\alpha \approx 0$ cannot be directly determined, since a free-flight value of the dynamic stability derivative is not available. However, it was shown in Figs. 10, 11, and 12 that the model wake geometry at $\alpha \approx 0$ when supported by the basic sting was close to being the same as the free-flight model wake geometry. Probably the basic sting produced little or no support interference effect on the dynamic stability data at $\alpha \approx 0$. It is also evident that the sting interference-free dynamic stability coefficient (free-flight value) at $\alpha \approx 0$ is equal to or greater (more unstable) than the value obtained with the BLDT model supported by the basic sting.

4.1.3 Comparison of Present Results with Results from PWT 16S

Figure 21 shows a comparison of the previous PWT data (Ref. 16) with the present data for configuration 721M. Mach number, Reynolds number, reduced frequency parameter ($\omega d/2V_\infty$), and amplitude of oscillation are all very closely matched. The comparison is good and shows that the instability at $\alpha \approx 0$ does exist and is an aerodynamic effect instead of a tunnel vibration effect. The noted instabilities in free flight (Section 4.1.1) also support this conclusion.

Since the results from the previous tests indicated substantial Reynolds number effects, the damping derivatives were determined for a range of Reynolds numbers during the present tests. These data are shown in Fig. 22 for several angles of attack and Mach numbers. As angle of attack is increased, the effect of Reynolds number on the derivatives becomes less. At $\alpha \approx 0$ the damping trends with Reynolds number were dependent on Mach number. These effects were similar to those found during the previous Viking test (Ref. 16). One point worth special mention is that for a Reynolds number of 1.5×10^6 at $M_\infty = 2.75$, an instability at $\alpha = 0$ is noted, even though there is no instability at the lower Reynolds numbers.

Figure 23 shows the PWT and VKF damping data as functions of Mach number. The damping derivatives are highly nonlinear with Mach number; and considering that there are slight differences in Reynolds number, the two sets of data agree satisfactorily.

The PWT results obtained with a sting geometry of $d_s/d = 0.0967$ and $\ell_s/d = 1.37$ and at $\omega d/2V_\infty \approx 0.03$ might contain some support interference effects. It is evident from Figs. 13 and 14 that the sting diameter effect on the damping derivatives becomes less as $\omega d/2V_\infty$ increases. Therefore, the PWT results probably contain very little sting diameter effects since those data were obtained at $\omega d/2V_\infty \approx 0.03$. This point is substantiated by the fact that the present results on configuration 721M agree well with the PWT results, even though the sting diameter is twice as large. Figure 17 shows that sting length effects for a sting diameter ratio of 0.183 are large for $\omega d/2V_\infty \approx 0.008$, but for $\omega d/2V_\infty \approx 0.02$ sting length effects are much less and show opposite trends. Even though data are not available for the higher reduced frequency (0.03), it is believed that based on Fig. 17 the PWT results are not affected largely by the relatively short effective sting length.

4.2 PRESENT TEST RESULTS

4.2.1 Free-Flight Drag Coefficient

Data for the Tunnel D entry are given in Tables I and II. The drag coefficients are shown in Figs. 24 and 25 as functions of Mach number and Reynolds number. The drag coefficient was found to be almost independent of Mach number and Reynolds number for the conditions tested. The average $C_D \approx 1.6$ is in general agreement with sting-supported data (Figs. 24 and 25) from Ref. 11 for a slightly different base geometry.

4.2.2 Effects of Amplitude of Oscillation

Representative damping-in-pitch derivatives are sketched in Fig. 26 as functions of angle of attack and amplitude of oscillation for the 721M and BLDT configurations. Figure 26a shows two representative variations of damping with angle of attack for a constant amplitude of oscillation. One curve (Region 1) is for the case for which the model is stable throughout the α range. The second curve is for the case where the model is unstable in the angle-of-attack range from 0 to approximately 2.5 deg (Region 3) and stable for angles of attack above about 3 deg (Region 2). Figure 26b shows representative sketches of the damping derivatives as functions of oscillation amplitude for constant angle of attack for the various regions of Fig. 26a. Whenever the model is stable (Regions 1 and 2), the damping derivatives vary little with amplitude of oscillation. In Region 3 where the model is unstable and the damping coefficient exhibits a steep gradient with angle of attack, the derivatives vary with the amplitude of oscillation. The three curves shown for Region 3 could even be repeat runs for the same test conditions (same α , M_∞ , p_o , and T_o). From the results of the previous Viking test at AEDC (Ref. 16), it was found that large scatter existed in the coefficients at and near zero angle of attack. It was thought that the aerodynamic phenomenon which caused the instability was unsteady in nature, leading to the scatter in the data. The same comment also applies to the present data. In some instances the present data for a given angle of attack in Region 3 are repeatable with θ , but for others it is not.

4.2.3 Effects of Angle of Attack

The damping-in-pitch derivatives for BLDT configurations 1000, 5000, and 4000 are shown in Figs. 27 through 31 as functions of angle of attack for $M_\infty = 1.76$ to 3. These data were obtained with the basic sting configuration ($d_s/d = 0.183$, $l_s/d = 3.55$). The trends of the damping derivatives with angle of attack are similar to those found during the previous tests (Ref. 16) on similar configurations. In general,

for the angle-of-attack range from 0 to ≈ 2.5 deg the damping derivatives at $M_\infty = 1.76$ (Figs. 27a, 28a, 29a, 30a, and 31a) are positive (dynamically unstable) and exhibit a steep gradient with angle of attack. For angles of attack from about 3 to 15 deg at $M_\infty = 1.76$, the damping derivatives are negative (dynamically stable) and are essentially invariant with angle of attack. At $M_\infty = 3$ the derivatives show very little effect of angle of attack, and the configurations are stable. For Mach numbers between 1.76 and 3 the pitch derivatives show intermediate trends between those found for $M_\infty = 1.76$ and $M_\infty = 3$. The damping trends with angle of attack are dependent on Mach number, Reynolds number, and reduced frequency parameter, and these trends are discussed in following sections of the report.

4.2.4 Effects of Reynolds Number

Figures 32, 33, and 34 show the damping derivatives as a function of Reynolds number for $\alpha \approx 0$ and 6 deg for the three reduced frequency ranges investigated. For an angle of attack of 6 deg the damping derivatives were negative (dynamically stable) and were essentially independent of Reynolds number for each Mach number and reduced frequency tested. This was typical for angles of attack from 3 to 15 deg. For the Mach numbers other than $M_\infty = 3$ the derivatives at $\alpha \approx 0$ were either negative or positive, depending on Mach number and Reynolds number, and were generally nonlinear with Reynolds number. At $M_\infty = 3$, $\alpha \approx 0$, all configurations were stable, and the derivatives showed very little variation with Reynolds number. In general, the variation of the damping coefficient with Reynolds number was small, but for a few specific cases (Figs. 22d, 32a, and 33b), one point gave an indication of a large erratic effect.

4.2.5 Effects of Mach Number

The damping derivatives as functions of Mach number for $\alpha \approx 0$ are presented in Fig. 35 for the three reduced frequencies tested. For the three reduced frequencies and the range of Reynolds numbers tested, the BLDT configuration was dynamically unstable at $M_\infty = 1.76$ and dynamically stable at $M_\infty = 3$. The stability or instability of the BLDT configuration for the Mach numbers between 1.76 and 3 depended upon the Reynolds number and the reduced frequency parameter. Although not shown, the damping-in-pitch derivatives for angles of attack between 3 and 15 deg were negative (dynamically stable) and showed very little variation with Mach number for the Reynolds numbers investigated.

4.2.6 Effects of Reduced Frequency Parameter

The dynamic stability derivatives as a function of reduced frequency parameter ($\omega d/2V_\infty$) are presented in Fig. 36 for the BLDT configuration at $\alpha \approx 0$. At $M_\infty = 1.76$ (Fig. 36a) increased reduced frequency reduced the level of dynamic instability for the Reynolds numbers tested. For $M_\infty \approx 2.00$ (Fig. 36b) and 2.24 (Fig. 36c) the reduced frequency effect on the damping derivatives was dependent on Reynolds number. At $M_\infty \approx 2.50$ (Fig. 36d) and 3 (Fig. 36e) the stability derivatives were essentially invariant with $\omega d/2V_\infty$ for the Reynolds numbers tested.

Figure 37 shows the effect of reduced frequency on the damping derivatives for $\alpha \approx 6$ deg. These trends are typical for angles of attack between 3 and 15 deg. The variation of $\omega d/2V_\infty$ had very little effect on the damping derivatives for angles of attack between 3 and 15 deg for the Mach numbers and Reynolds numbers tested.

4.2.7 Effects of Nozzles

Figures 38, 39, and 40 show the comparison of the damping derivatives with and without the nozzles for the BLDT configuration. For angles of attack from 3 to 15 deg at $M_\infty = 1.76$ and 2.23 and 0 to 15 deg at $M_\infty = 3$, the nozzles produced no noticeable effect on the damping derivatives for the reduced frequency parameters and Reynolds numbers tested. At zero angle of attack the comparison of the derivatives with and without the nozzles shows agreement in some cases (Figs. 39a, 40a, and 40b) and disagreement in others (Figs. 38a, 38b, and 39b) depending on Mach number, Reynolds number, and $\omega d/2V_\infty$. However, the effect of the nozzle at $\alpha = 0$, if any, is within the scatter and repeatability of the data, and the differences are not considered to be significant.

4.2.8 Effects of Combined Angle of Attack and Angle of Yaw

The BLDT configuration and balance were rolled -45 and -90 deg to determine the effect of combined angle of attack and angle of yaw on the damping derivatives. The model was oscillated in the -45- and -90-deg planes at various yaw angles. Since the configuration had an offset center of gravity, the static pitching moment deflected the cross flexures so that the model was always pitched to some angle of attack in the -45- and -90-deg planes; therefore, the angle of attack was never zero when the yaw angle was zero. The data then could not be directly compared with the $\phi = 0$ data.

Figure 41 shows the damping derivatives as functions of yaw angle for configuration 1090 ($\phi = -90$ deg). When the model and balance were rolled -90 deg, the model oscillated in a plane-of-symmetry flow field (except for the small angle of attack caused by the static pitching moment which becomes insignificant as yaw angle increases). For configuration 1000 ($\phi = 0$) the model oscillated in an unsymmetrical flow field (except at $\alpha = 0$) because of angle of attack. Although there is a difference in the flow fields about the models, the damping derivatives show generally the same trends with yaw angle (Config. 1090) that were found with angle of attack (Config. 1000, Figs. 27 and 28).

SECTION V CONCLUSIONS

Wind tunnel tests were conducted to substantiate earlier test results (Ref. 16) and to determine the dynamic stability characteristics of the BLDT configuration. The effects of Mach number, Reynolds number, angle of attack, amplitude of oscillation, reduced frequency parameter, sting diameter, effective sting length, combined angle of attack and angle of yaw, and rocket motor nozzles on the damping-in-pitch derivatives of the BLDT configuration were investigated. Free-flight tests of the BLDT configuration were also conducted to determine free-flight wake definition and drag coefficients. Data were obtained over a free-stream Mach number range from 1.76 to 3 at free-stream Reynolds numbers, based on maximum model diameter, ranging from 0.25×10^6 to 1.49×10^6 . Conclusions based on the results presented in this report are given below.

1. Dynamic instabilities at zero angle of attack on similar configurations have been found during forced-oscillation tests at PWT and free-flight and free-oscillation tests at VKF. The present data (Config. 721M) agreed well with the PWT results. Therefore, the model instability at zero angle of attack shown in the PWT results does exist and was not a tunnel vibration effect.
2. The basic sting probably produced little or no support interference effects on the BLDT dynamic stability data; therefore, the dynamic instabilities at angles of attack near zero do not appear to be caused by sting interference.

3. For angles of attack between 3 and 15 deg the BLDT configuration was dynamically stable, and the derivatives were generally not a function of Mach number, amplitude of oscillation, Reynolds number, or reduced frequency parameter. At angles of attack near zero the BLDT model was dynamically unstable at the lower Mach numbers, and the data showed very erratic effects with variation of the test parameters.
4. In general, the presence of the BLDT rocket motor nozzles did not affect the damping-in-pitch derivatives.
5. The damping-in-pitch derivatives of the BLDT configuration generally showed the same trends with yaw angle as with angle of attack.
6. Drag coefficients showed little variation with Mach number and Reynolds number.

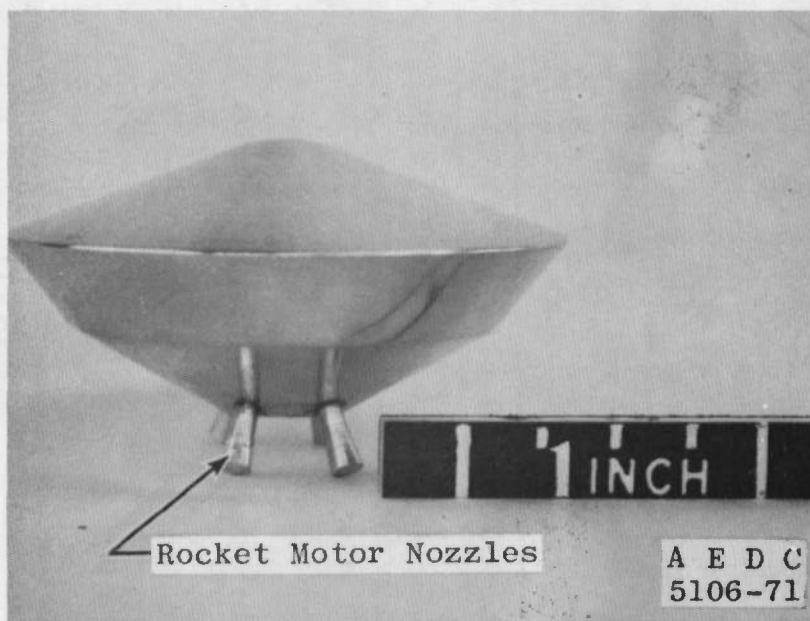
REFERENCES

1. Krumins, Maigonis V. "A Ballistic Range Study of Aerodynamic Characteristics of Mars Probe/Lander Shapes." AIAA Preprint No. 67-167, Fifth Aerospace Sciences Meeting, January 1967.
2. Bendura, Richard J. "Low Subsonic Static and Dynamic Stability Characteristics of Two Blunt 120° Cone Configurations." NASA-TN-D-3853, February 1967.
3. Campbell, James F. "Longitudinal Aerodynamic Characteristics of Several High-Drag Bodies at Mach Numbers from 1.5 to 4.63." NASA-TN-D-3915, April 1967.
4. Darnell, Wayne L., Henning, Allen B., and Lundstrom, Reginald R. "Flight Test of a 15-Ft-Diameter (4.6-Meter) 120° Conical Spacecraft Simulating Parachute Deployment in a Mars Atmosphere." NASA-TN-D-4266, December 1967.
5. Whitlock, Charles H. and Bendura, Richard J. "Dynamic Stability of a 4.6-Meter-Diameter 120° Conical Spacecraft at Mach Numbers from 0.78 to 0.48 in a Simulated Martian Environment." NASA TN D-4558, May 1968.
6. Campbell, James F. and Howell, Dorothy T. "Supersonic Aerodynamics of Large-Angle Cones." NASA-TN-D-4719, August 1968.

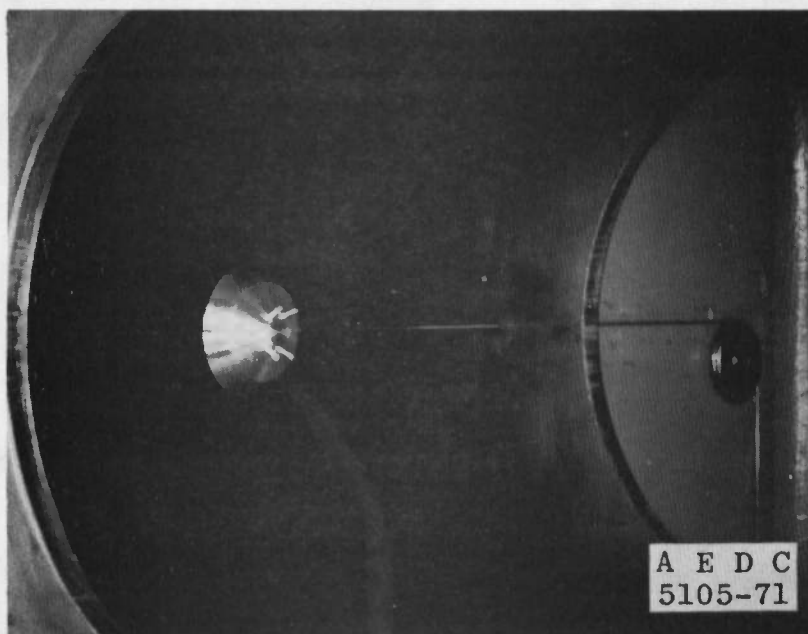
7. Whitlock, Charles H., Bendura, Richard J., and Henning, Allen B. "Dynamic Stability Characteristics of Large-Size 120° Blunted Conical Spacecraft in a Simulated Martian Environment." AIAA Preprint No. 69-104, Seventh Aerospace Sciences Meeting, January 1969.
8. Marko, W. "Dynamic Stability of High-Drag Planetary Entry Vehicles at Transonic Speeds." AIAA Preprint No. 69-105, Seventh Aerospace Sciences Meeting, January 1969.
9. Deveikis, William D. and Sawyer, James Wayne. "Effects of Cone Angle, Base Flare Angle, and Corner Radius on Mach 3.0 Aerodynamic Characteristics of Large Angle Cones." NASA-TN-D-5048, March 1969.
10. Campbell, James F. and Grow, Josephine W. "Experimental Flow Properties in the Wake of a 120° Cone at Mach Number 2.20." NASA-TN-D-5365, July 1969.
11. Campbell, James F. "Supersonic Aerodynamic Characteristics and Shock Standoff Distances for Large-Angle Cones with and without Cylindrical Afterbodies." NASA TN-D-5334, August 1969.
12. Sammonds, Robert I. "Aerodynamics of Mars Entry Probe-Lander Configurations at a Mach Number of 10." NASA-TN-D-5608, January 1970.
13. Gibson, Frederick W. and Carter, James E. "Free-Flight Measurements of Dynamic Stability Derivatives of a Blunted 120° Cone in Helium at Mach Number 15.4." NASA-TM-X-2071, October 1970.
14. Brown, Clarence A., Jr., Campbell, James F. and Tudor, Dorothy H. "Experimental Wake Survey behind a 120°-Included Angle Cone at Angles of Attack of 0° and 5°, Mach Numbers from 1.60 to 3.95, and Longitudinal Stations Varying from 1.0 to 8.39 Body Diameters." NASA TM X-2139, January 1971.
15. McAlister, Kenneth W., Stewart, David A. and Peterson, Victor L. "Aerodynamic Characteristics of a Large-Angle Blunt Cone with and without Force Type Afterbodies." NASA TN D-6269, April 1971.
16. Usselton, B. L., Shadow, T. O., and Mansfield, A. C. "Damping-in-Pitch Derivatives of 120- and 140-deg Blunted Cones at Mach Numbers from 0.6 through 3." AEDC-TR-70-49, (AD868237L), April 1970.

17. Billingsley, J. P. and Norman, W. S. "Relationship between Local and Effective Aerodynamic Pitch-Damping Derivatives as Measured by a Forced-Oscillation Balance for Preliminary Viking Configurations." AEDC-TR-72-25, May 1972.
18. Schueler, C. J., Ward, L. K., and Hodapp, A. E., Jr. "Techniques for Measurements of Dynamic Stability Derivatives in Ground Test Facilities." AGARDograph 121 (AD669227), October 1967.
19. Beers, Yardley. Introduction to the Theory of Error. Addison Wesley Publishing Company, Inc., Reading, Massachusetts, 1957, pp. 26-36.

APPENDIXES
I. ILLUSTRATIONS
II. TABLES



a. BLDT Config. ($d = 2$ in.)



b. Tunnel D Installation Photograph
Fig. 1 Free-Flight Model Photographs

Configuration 721M

PWT Model and Sting Simulation

$$d = 6 \text{ in.}$$

$$\frac{x_{cg}}{d} = 0.232$$

$$\frac{z_{cg}}{d} = 0$$

$$\frac{l_s}{d} = 1.37$$

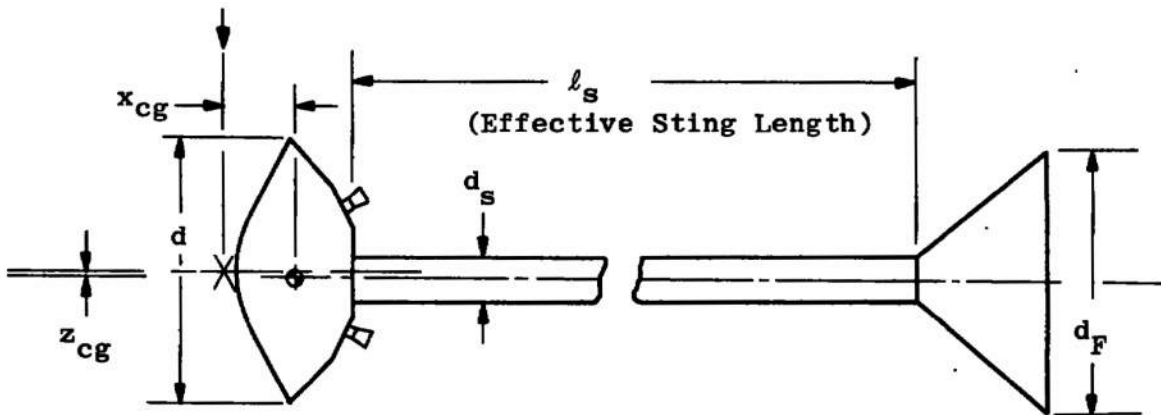
BLDT Configurations

Nozzles and
 $\frac{\omega d}{2V_\infty}$ Combinations

$\left. \begin{array}{c} A \\ B \\ C \\ D \end{array} \right\} \frac{l_s}{d}, \frac{d_s}{d} \text{ Combinations}$

Model Roll Angle

Theoretical Apex of Sharp Nose



$$\frac{x_{cg}}{d} = 0.231, \quad \frac{z_{cg}}{d} = 0.010, \quad d = 6 \text{ in.}$$

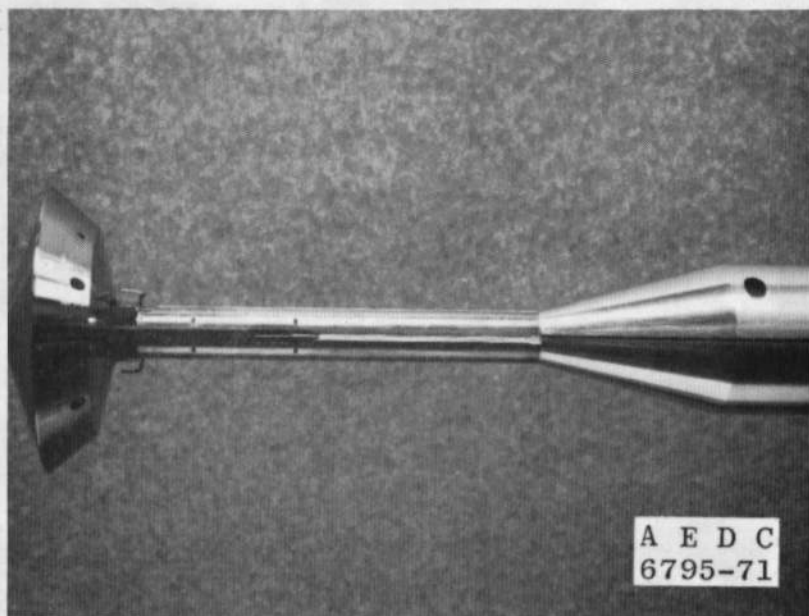
Fig. 2 Nomenclature, Dynamic Stability Models

<u>A</u>		<u>Nozzles</u>		$\omega d/2V_\infty$
1		On		0.008
2		Off		0.008
3		Off		0.020
4		On		0.030
5		On		0.020
6		Off		0.030

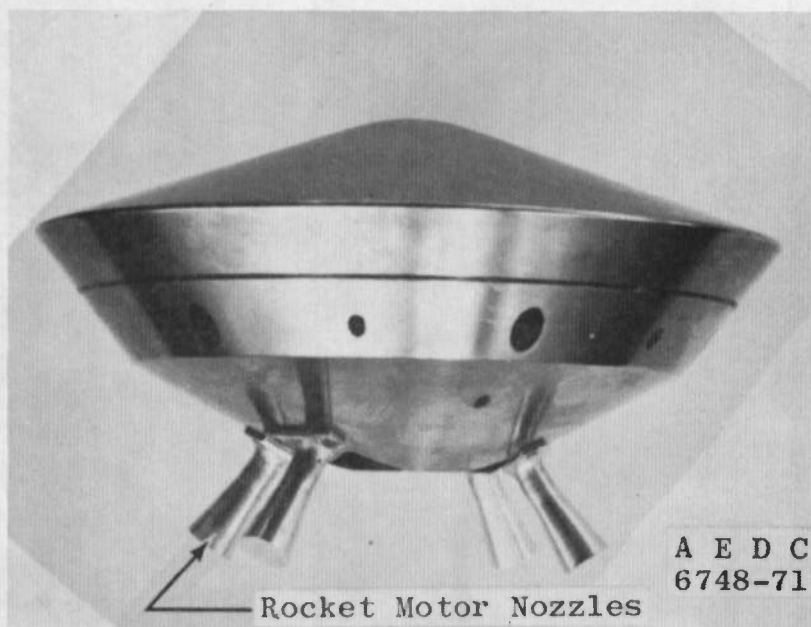
<u>B</u>	$d_s, \text{ in.}$	d_s/d	$\ell_s, \text{ in.}$	ℓ_s/d
0	1.10	0.183	21.37 (Basic) ($d_F = 3.3 \text{ in.}$)	3.55
1	1.10	0.183	21.37 ($d_F = 6 \text{ in.}$)	3.55
3	1.10	0.183	9.00	1.50
4	2.10	0.350	21.37	3.55
6	2.10	0.350	9.00	1.50
7	3.18	0.530	21.37	3.55
9	3.18	0.530	9.00	1.50

<u>CD</u>	<u>$\phi, \text{ deg}$</u>
00	0
45	-45
90	-90

Fig. 2 Concluded

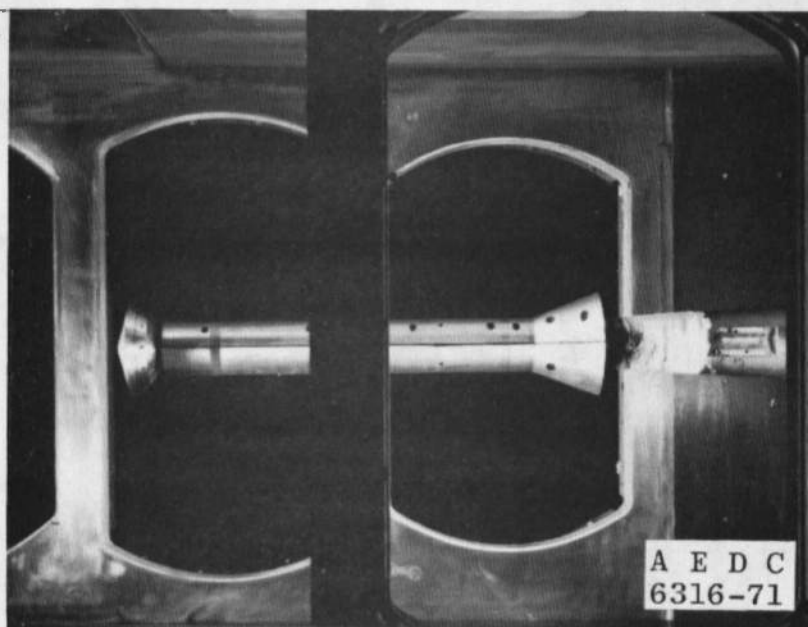


a. Config. 721M, PWT Model-Sting Simulation

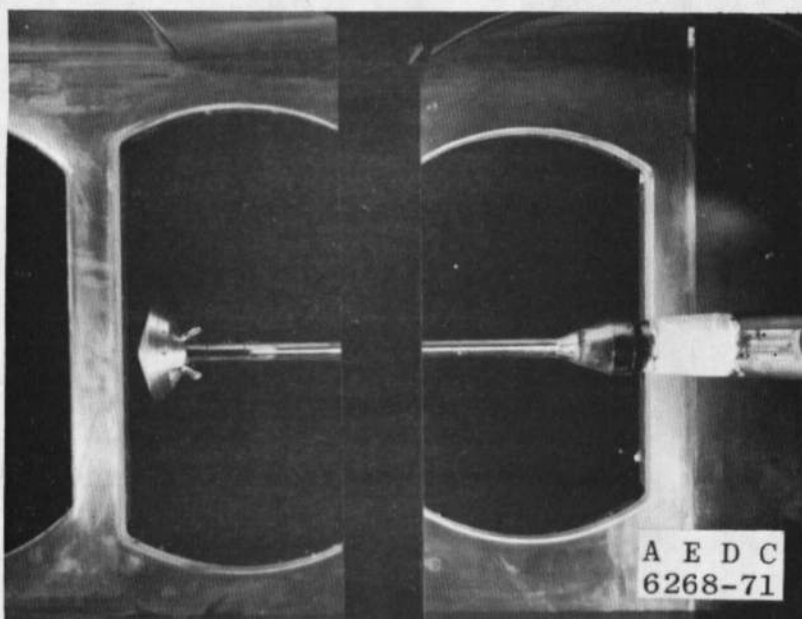


b. BLDT Config. ($d = 6$ in.)

Fig. 3 Photographs of Dynamic Stability Models

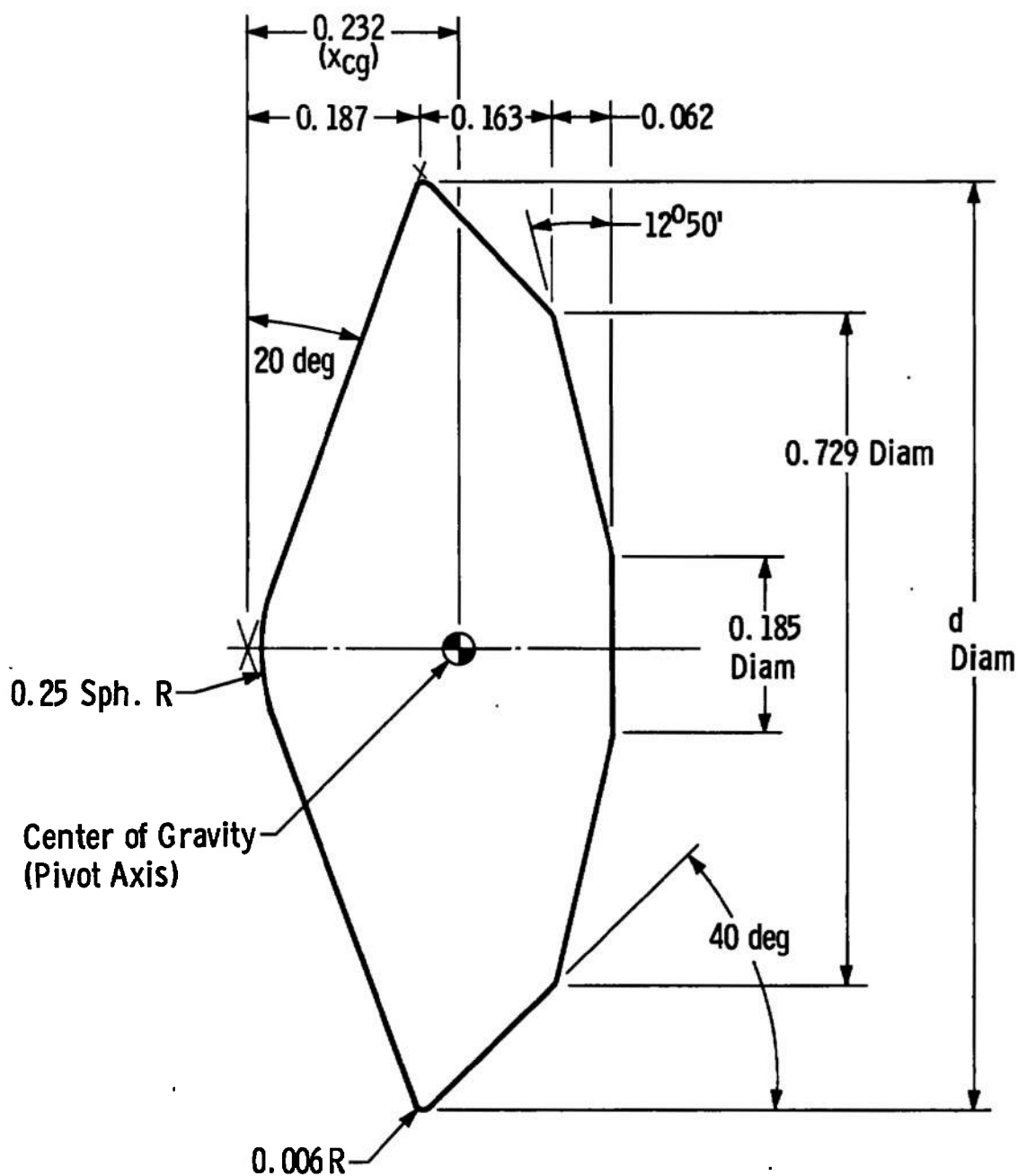


a. Config. A700, $d_s/d = 0.530$, $\ell_s/d = 3.55$



b. Config. A000, Basic Sting Geometry,
 $d_s/d = 0.183$, $\ell_s/d = 3.55$

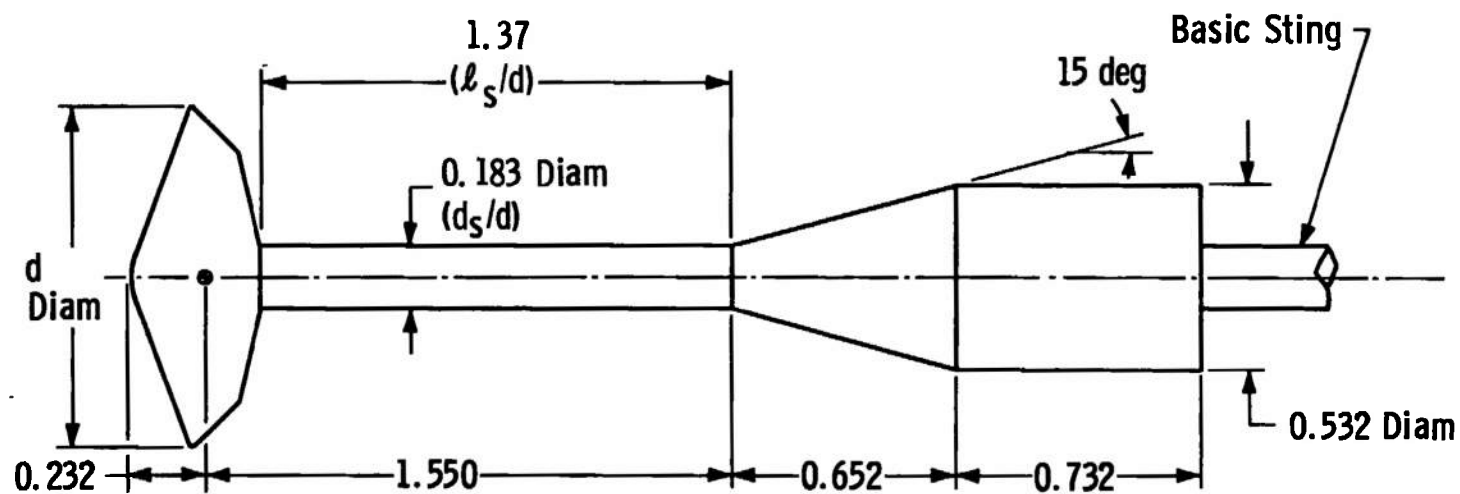
Fig. 4 BLDT Installation Photographs (Tunnel A)



All Linear Dimensions Normalized by d ($d = 6 \text{ in.}$)

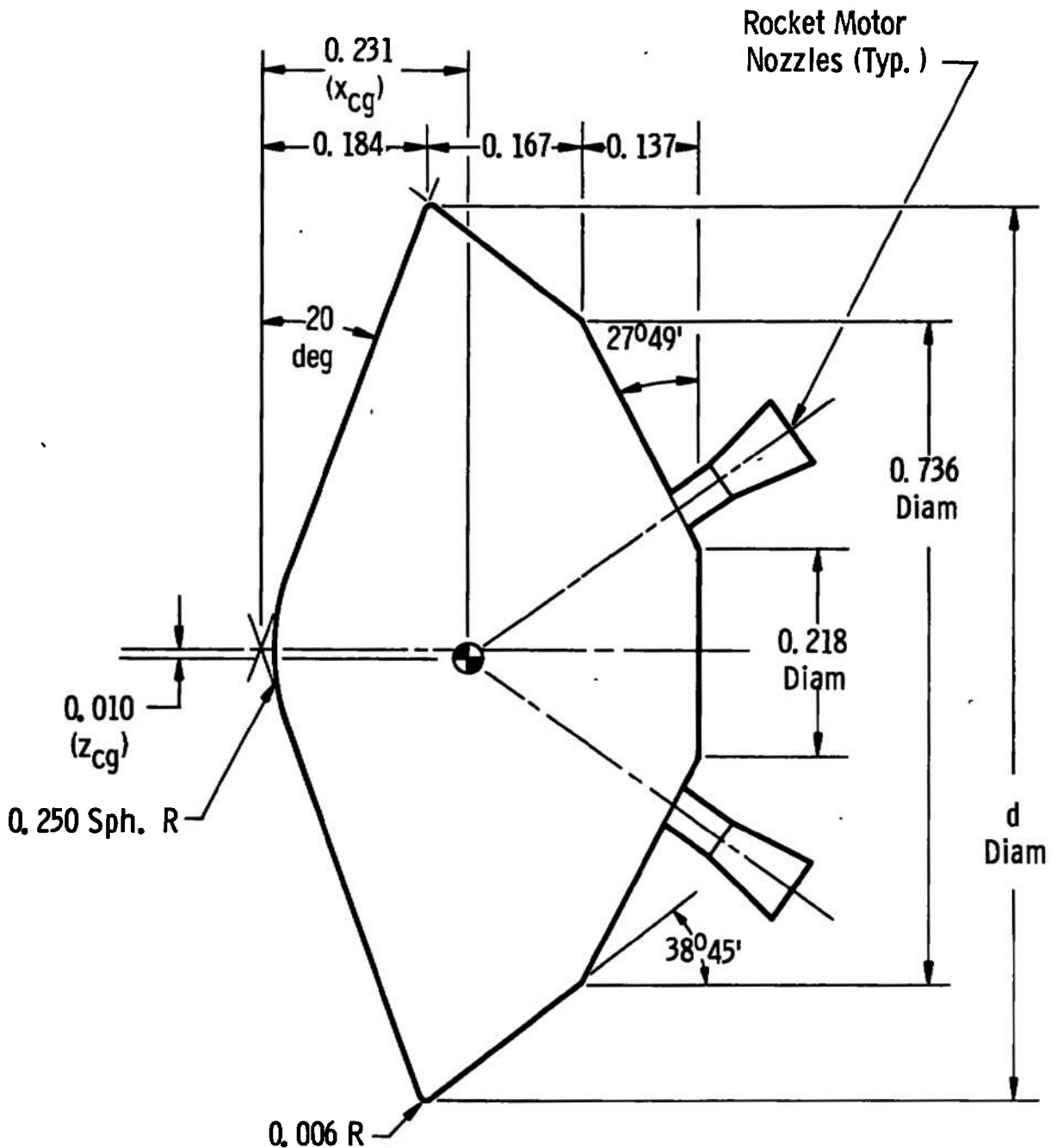
a. Model Geometry

Fig. 5 Config. 721M Model and Sting Geometry



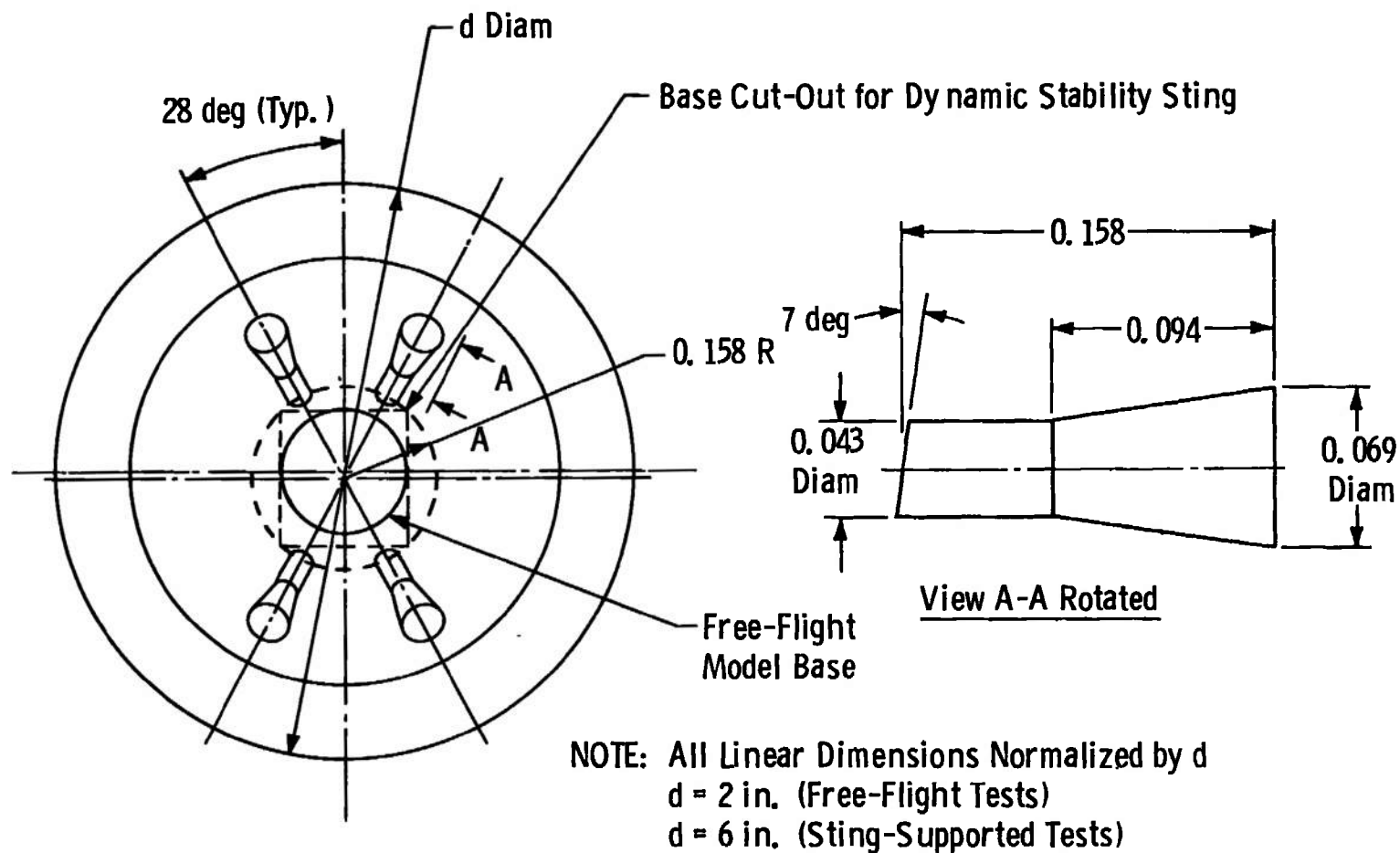
All Linear Dimensions Normalized by d ($d = 6$ in.)

b. Sting Geometry
Fig. 5 Concluded

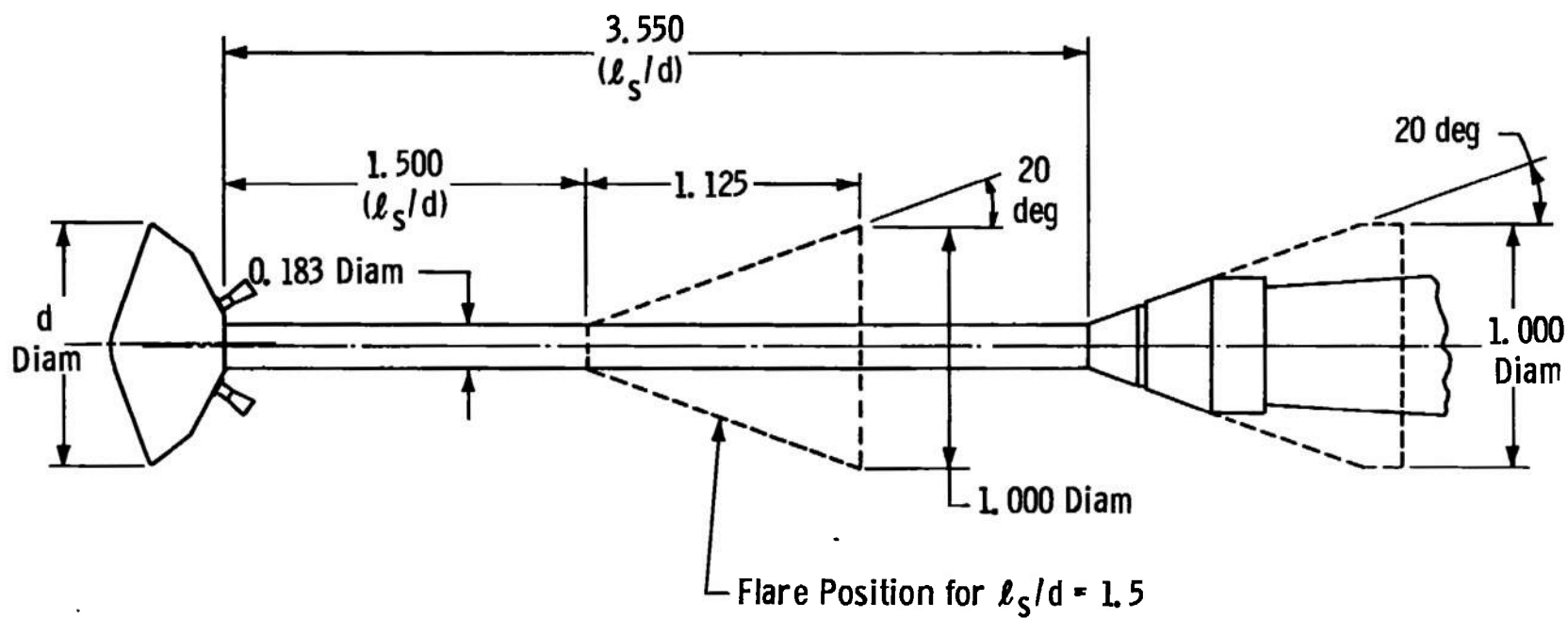


NOTE: All Linear Dimensions Normalized by d
 $d = 2$ in. (Free-Flight Tests)
 $d = 6$ in. (Sting-Supported Tests)

a. Model Geometry
 Fig. 6 BLDT Model and Sting Geometry

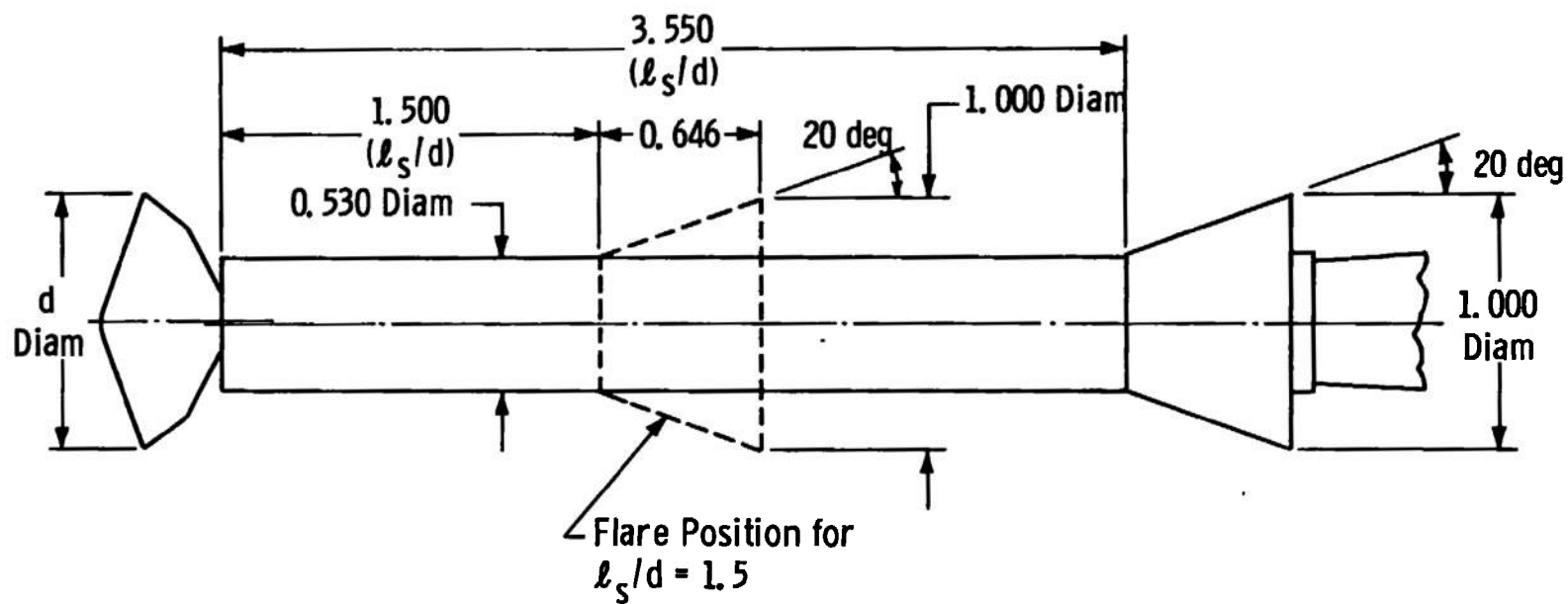


b. Rocket Motor Nozzle Geometry
 Fig. 6 Continued



NOTE: All Linear Dimensions Normalized by d
 $d = 6$ in.

c. BLDT Sting Geometry ($d_s/d = 0.183$)
 Fig. 6 Continued



NOTE: All Linear Dimensions Normalized by d
 $d = 6$ in.

d. BLDT Sting Geometry ($d_s/d = 0.530$)
 Fig. 6 Concluded

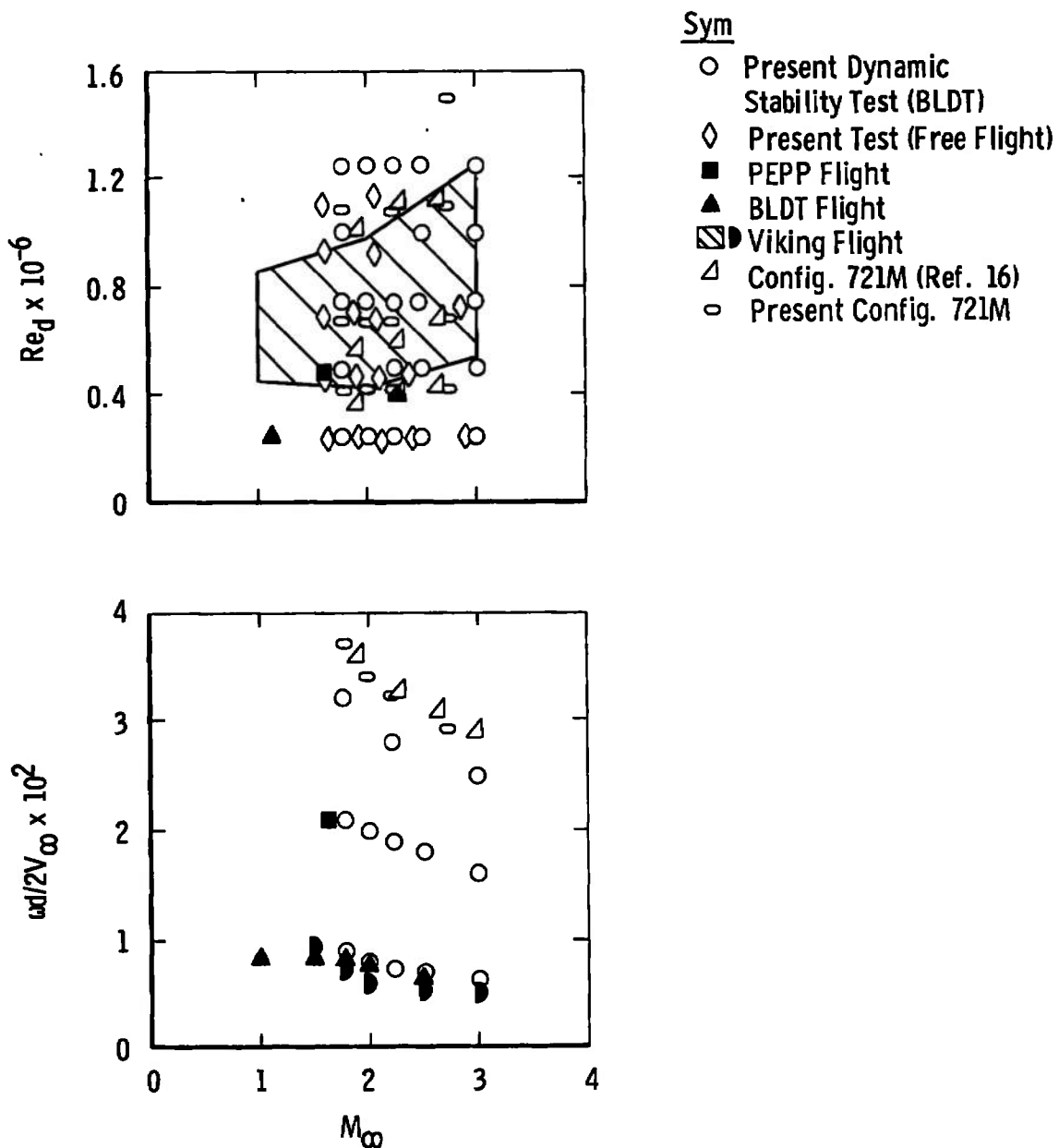


Fig. 7 Comparison of Wind Tunnel and Approximate Flight Test Conditions

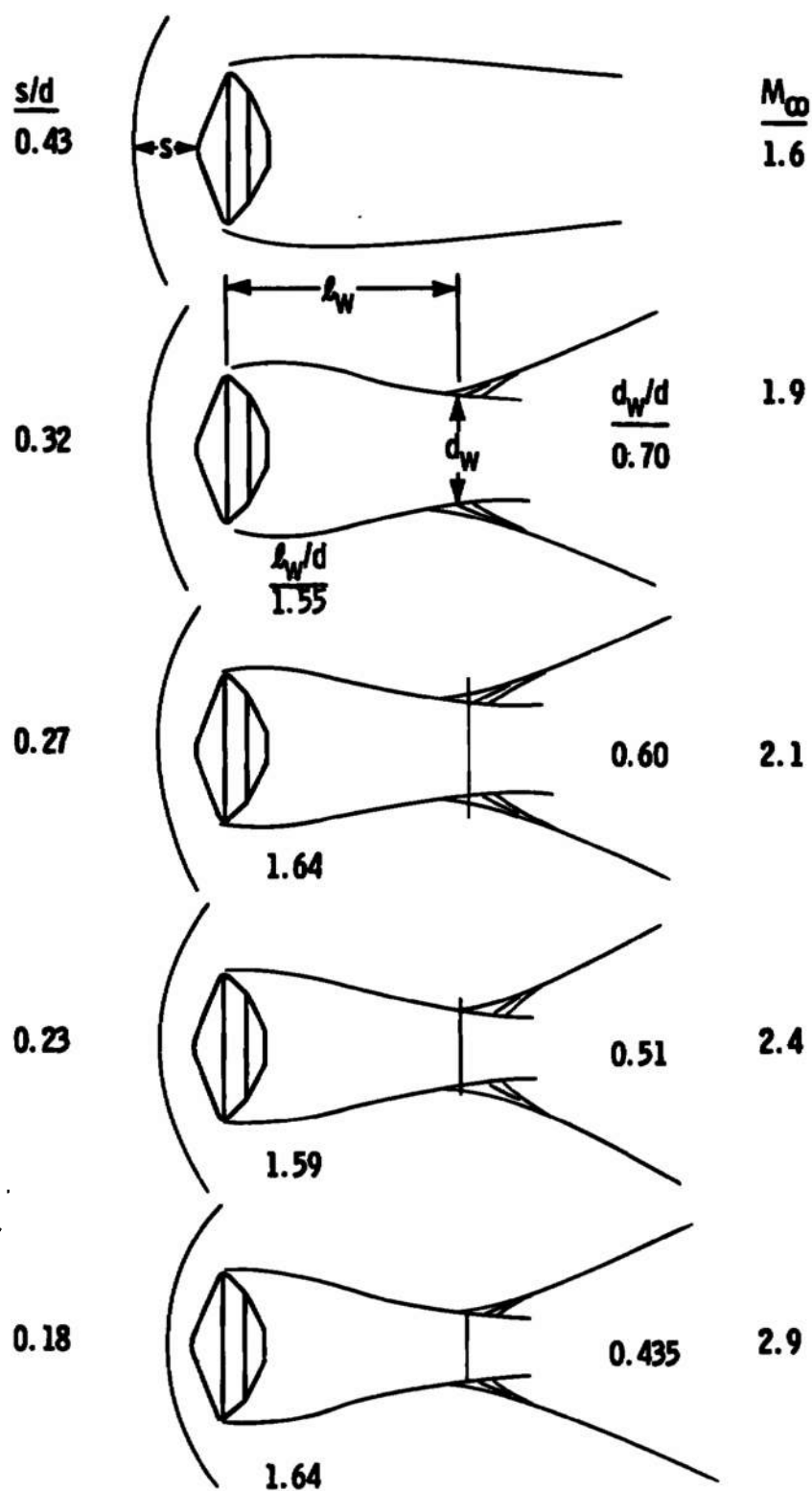
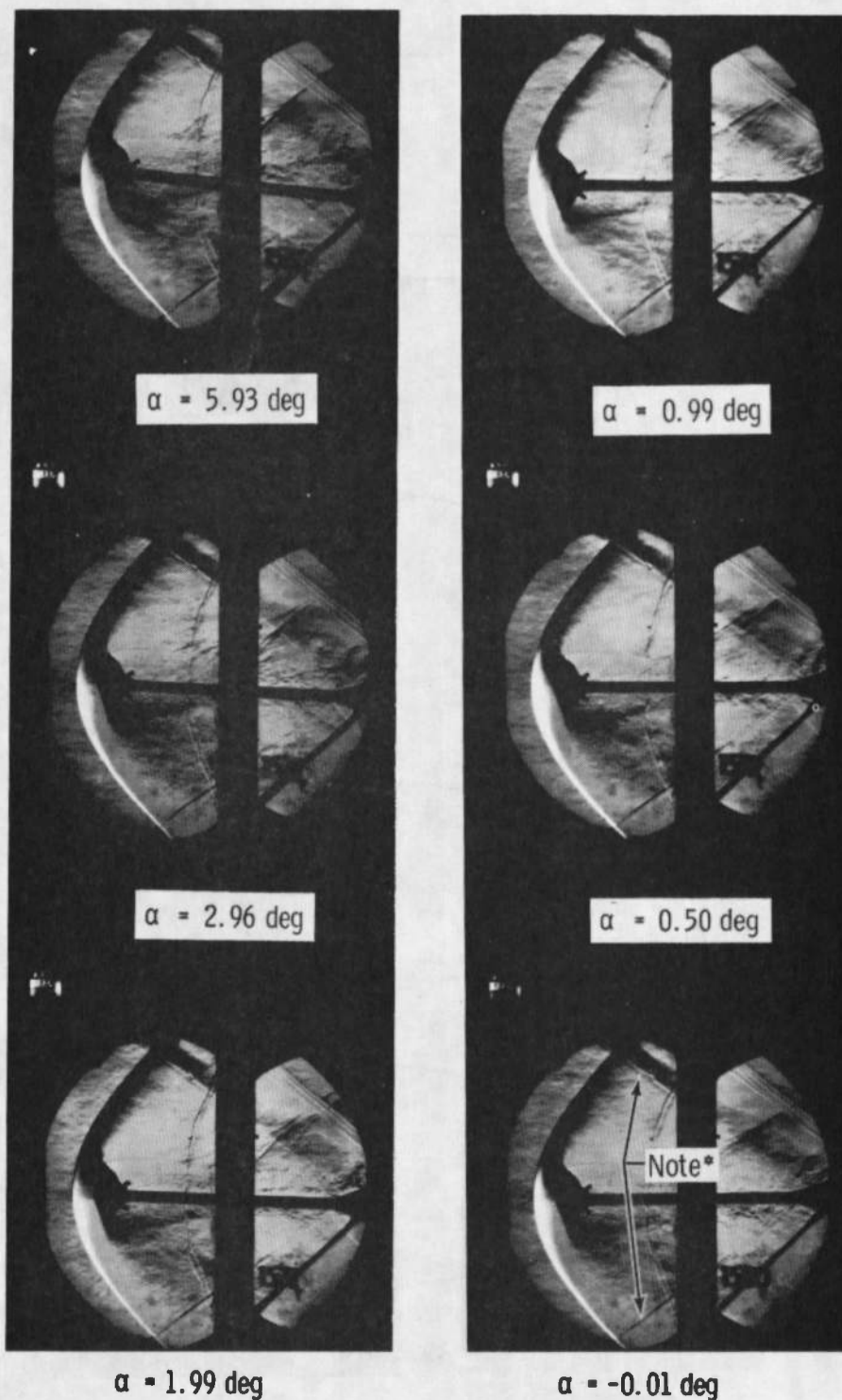


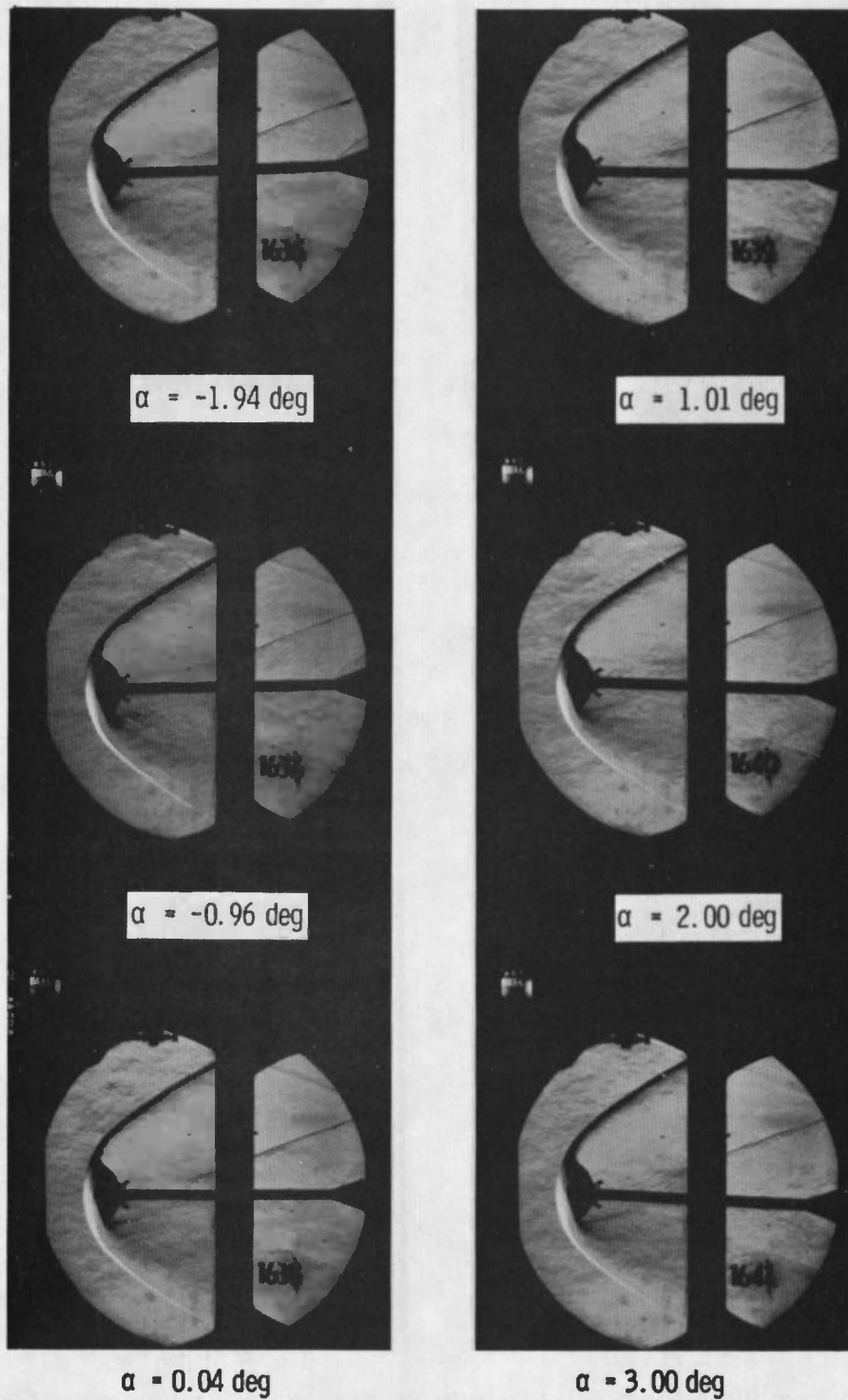
Fig. 8 Shock and Wake Patterns in Free Flight, $\alpha \approx 0$



*Shock from Pin A, Hinge Point for Diffuser Plate (Typical All Photographs)

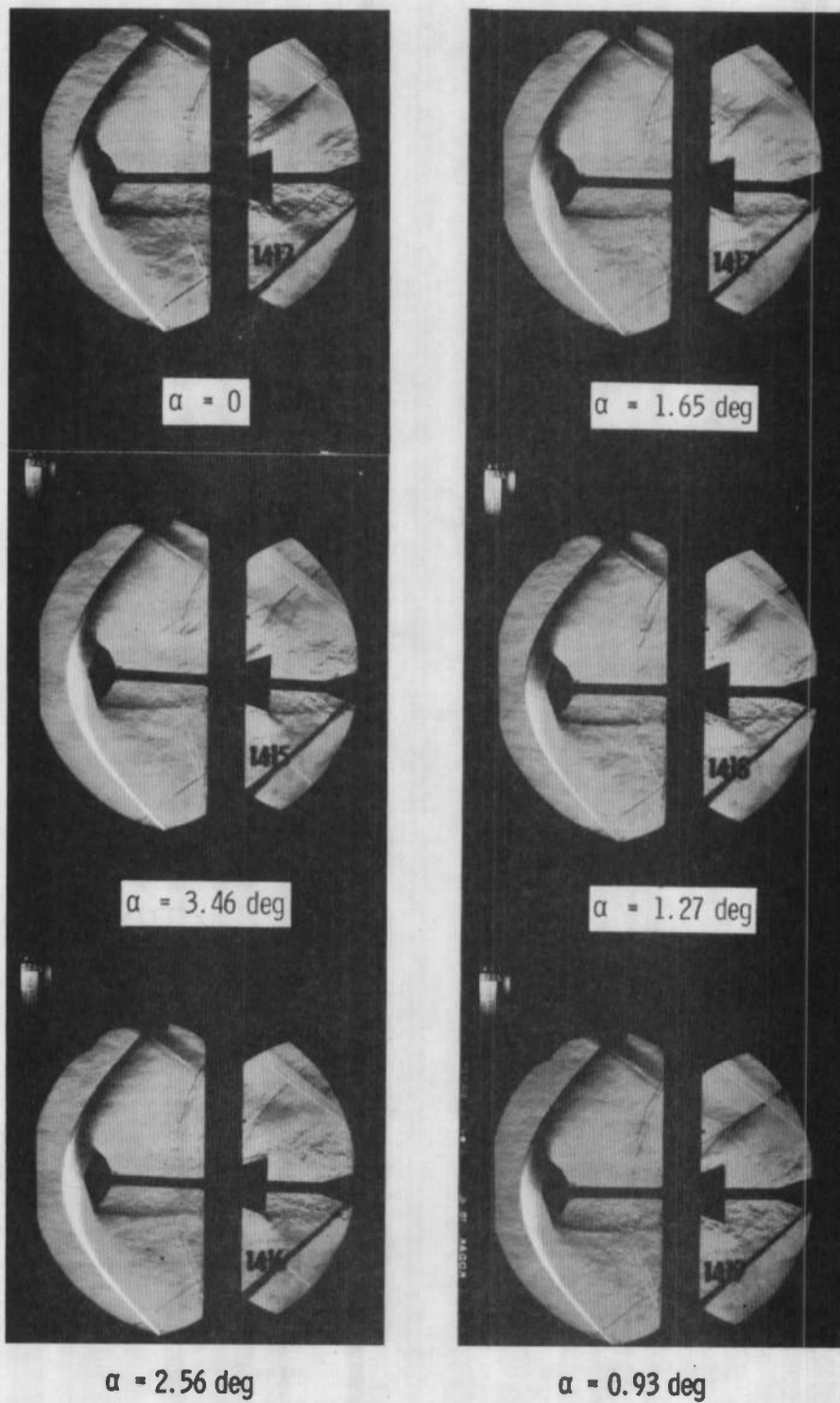
a. Config. 4000, $M_\infty = 1.76$, $Re_d \times 10^{-6} = 0.75$

Fig. 9 Typical Schlieren Photographs from Tunnel A, BLDT Config.



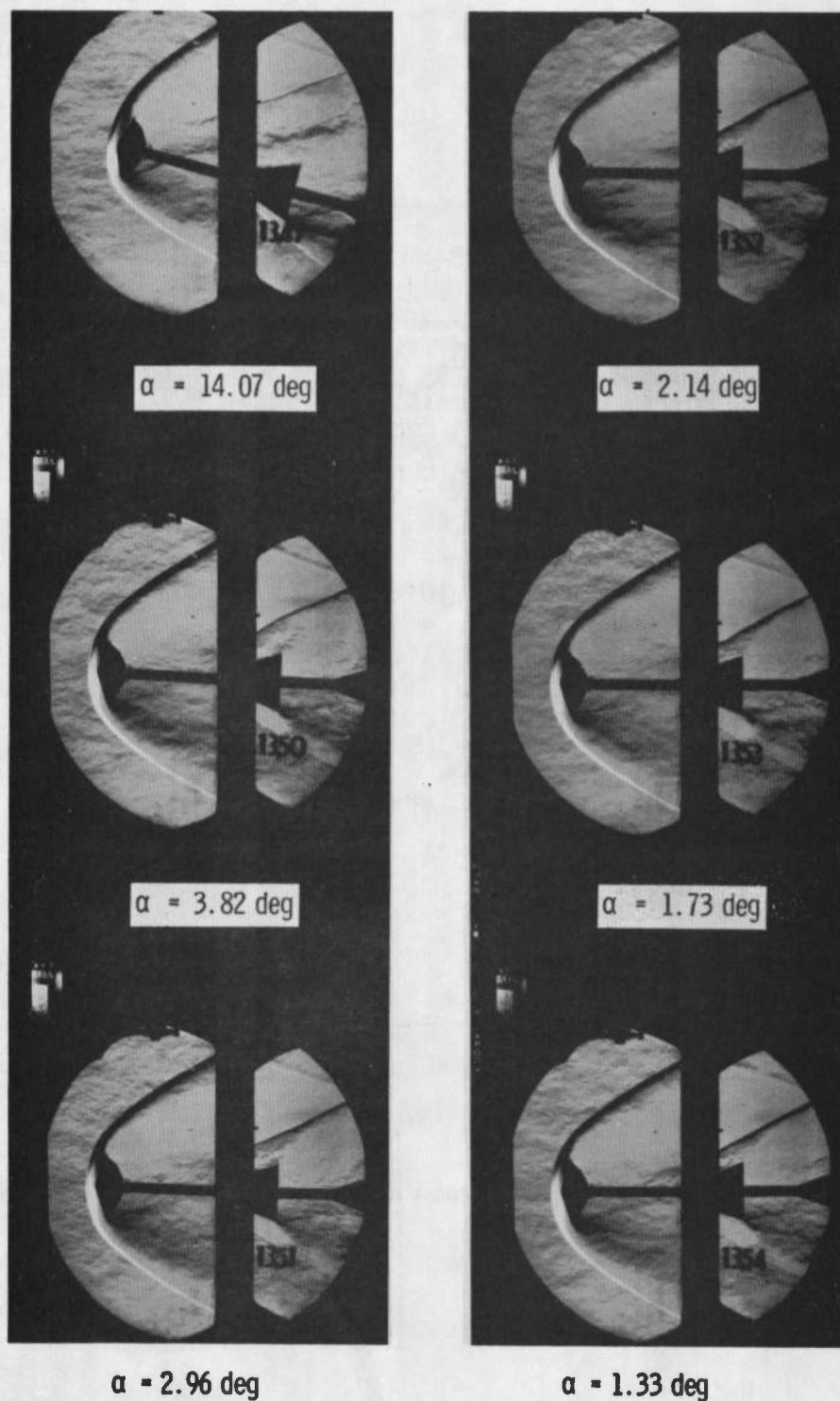
b. Config. 4000, $M_\infty = 2.99$, $Re_d \times 10^{-6} = 0.75$

Fig. 9 Continued



c. Config. 2300, $M_\infty = 1.76$, $Re_d \times 10^{-6} = 0.75$

Fig. 9 Continued



d. Config. 2300, $M_\infty = 3.00$, $Re_d \times 10^{-6} = 1.25$

Fig. 9 Concluded

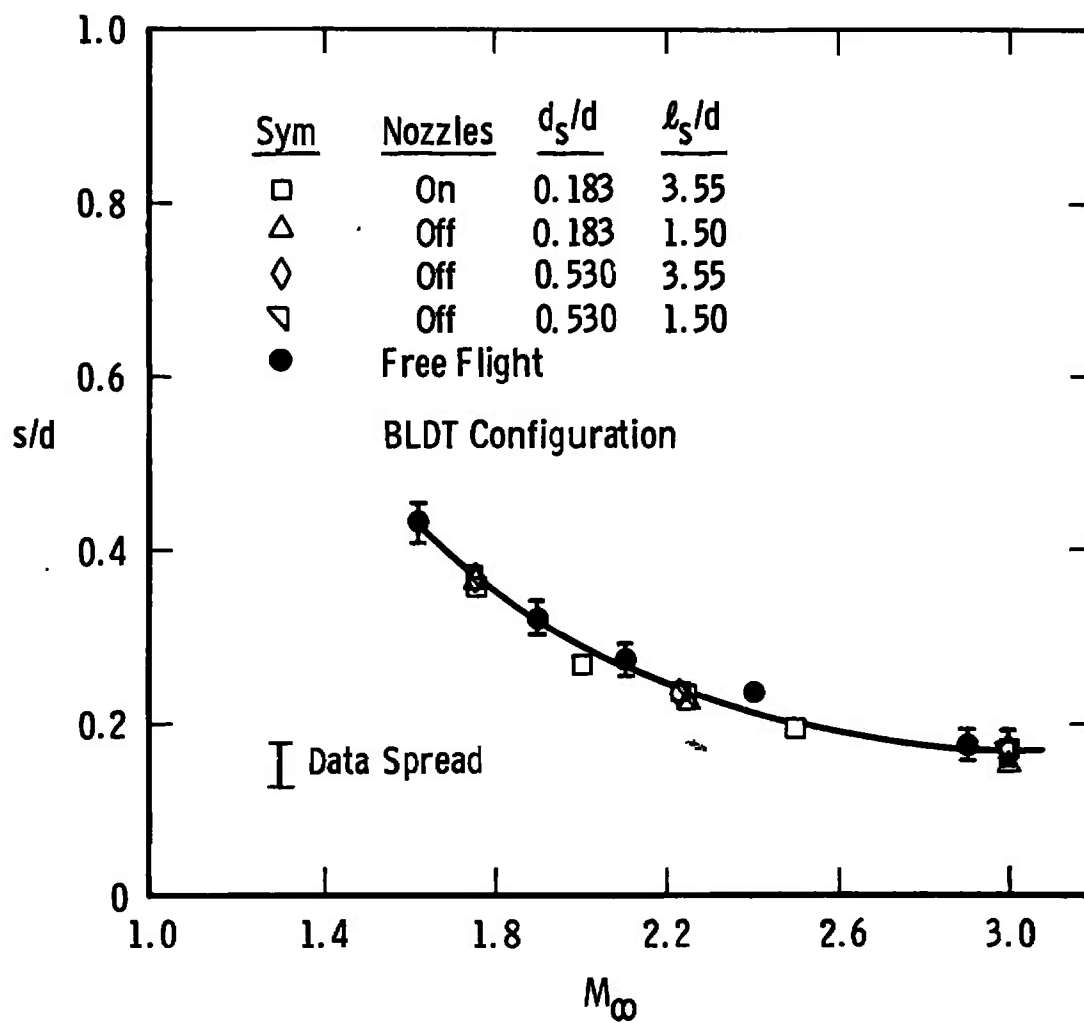


Fig. 10 Bow Shock Stand-Off Distance as a Function of Mach Number

	Sym	Nozzles	d_s/d	l_s/d
-----	□	On	0.183	3.55
- - - - -	△	Off	0.183	1.50
-----	◇	Off	0.530	3.55
.....	▽	Off	0.530	1.50
————	●	Free Flight		

BLDT Configuration.

Symbols Indicate Range of Re_d from 0.25×10^6 to 1.25×10^6 Except as Noted for \triangle and ∇ at $M_\infty = 2.25$

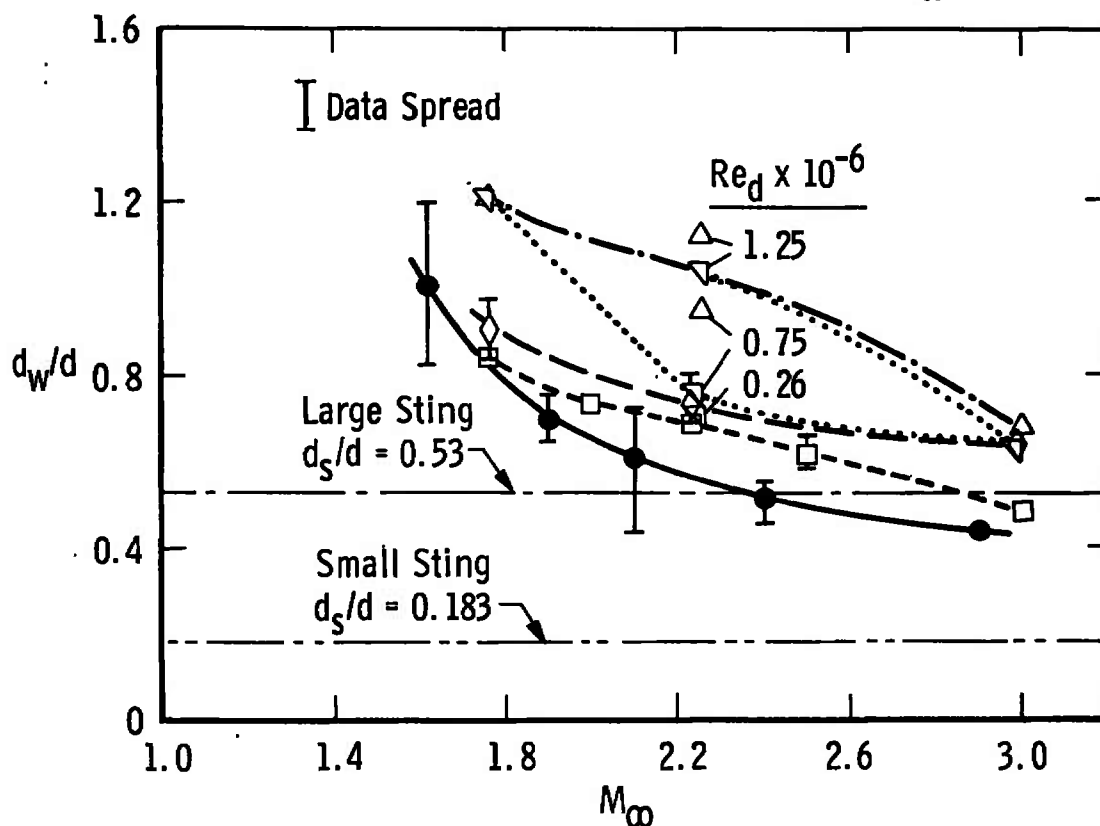


Fig. 11 Wake Diameter as a Function of Mach Number

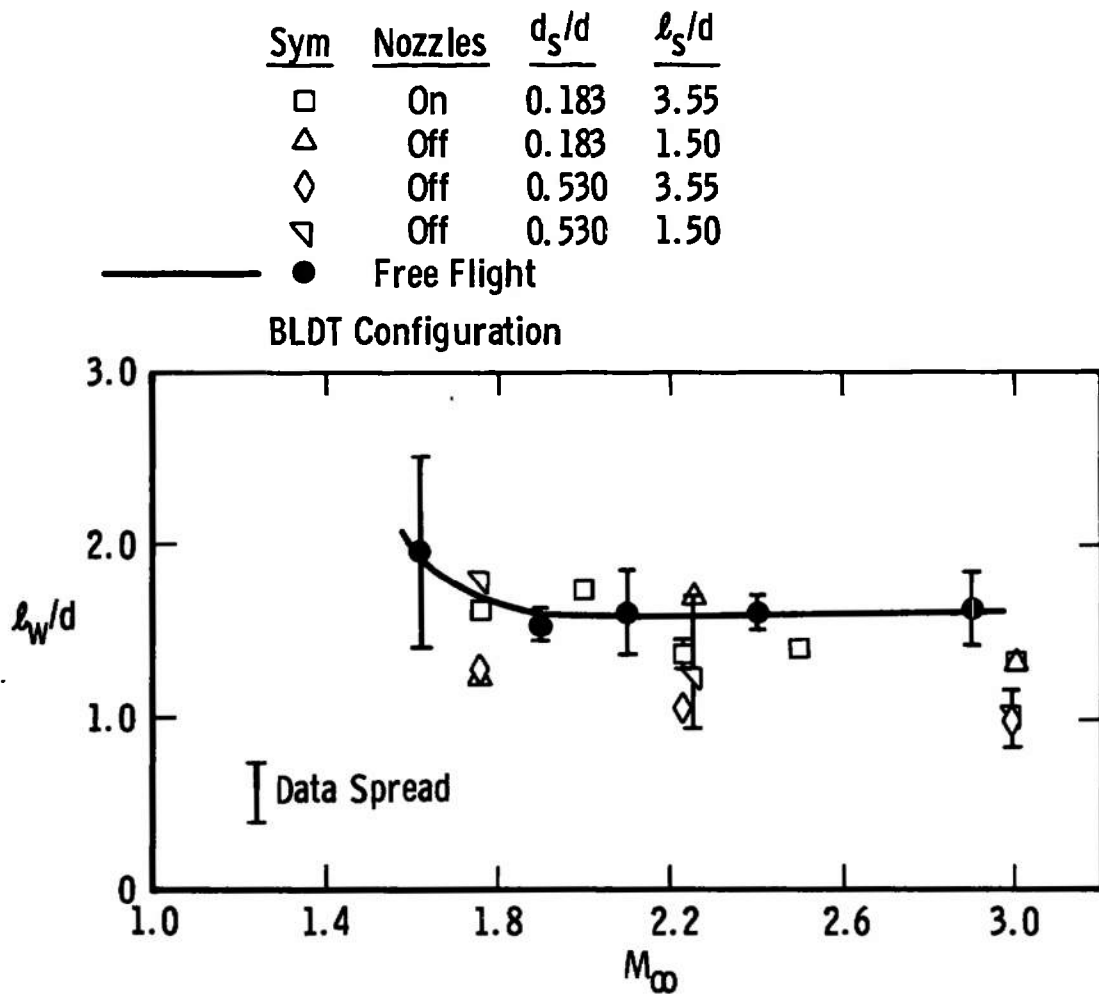
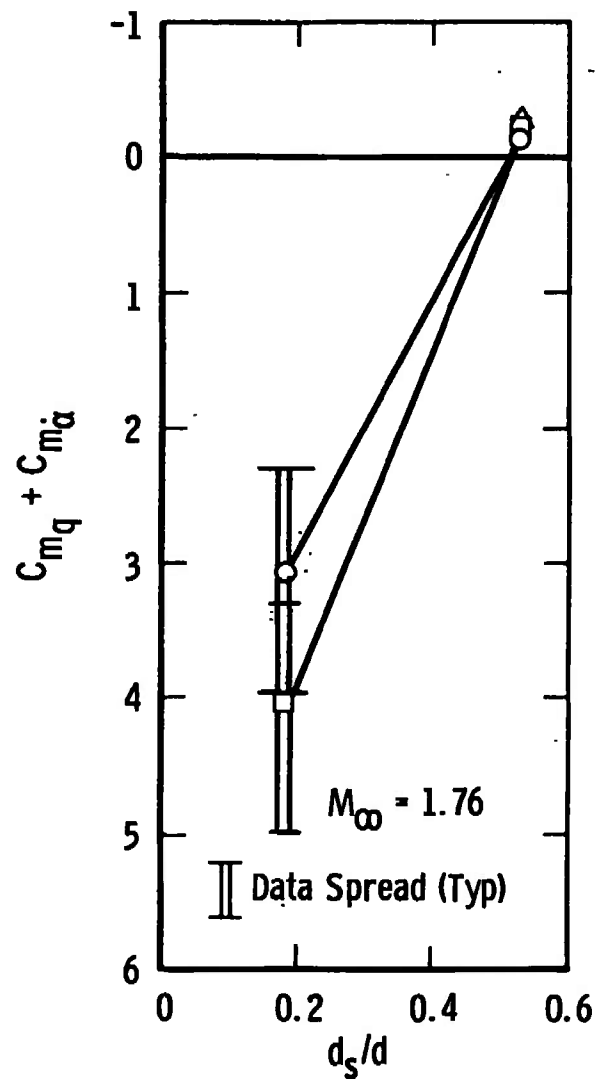


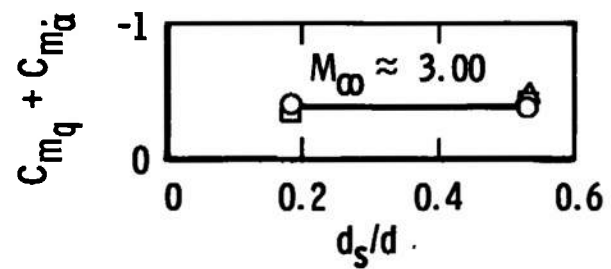
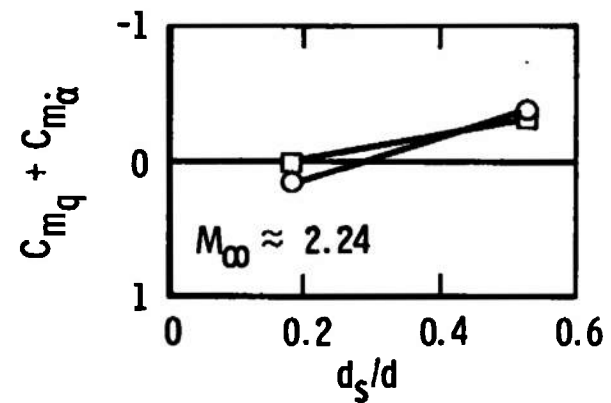
Fig. 12 Distance from Maximum Model Diameter to Minimum Wake Diameter as a Function of Mach Number



Sym $\approx Re_d \times 10^{-6}$

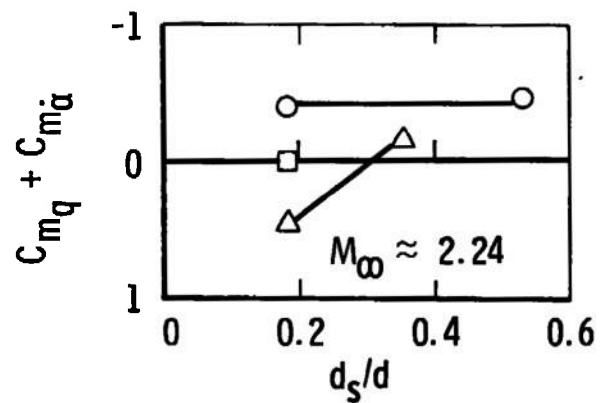
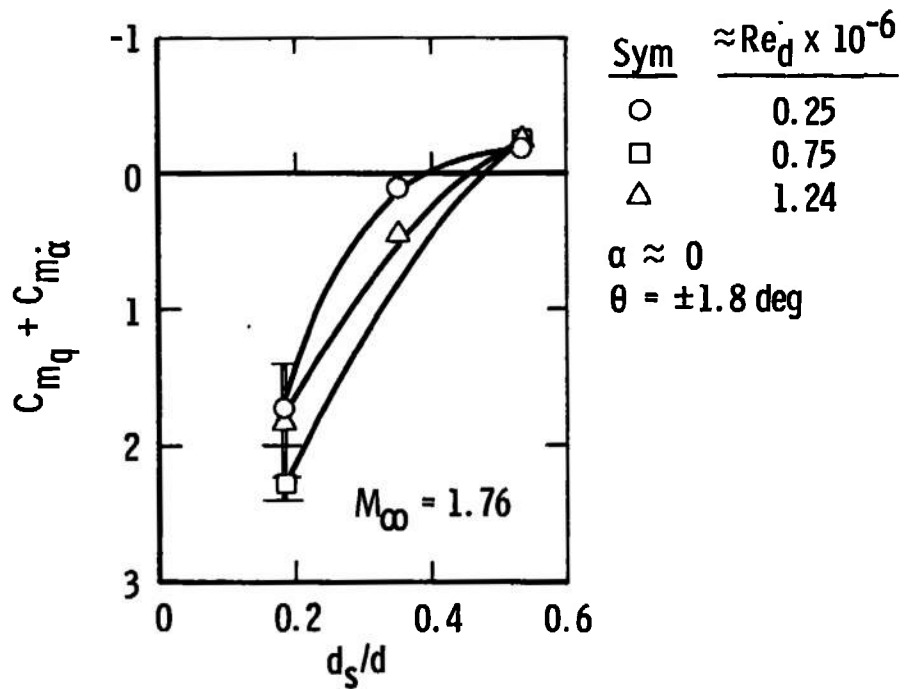
○ 0.25
 □ 0.75
 △ 1.24

$\alpha \approx 0$
 $\theta = \pm 1.8 \text{ deg}$

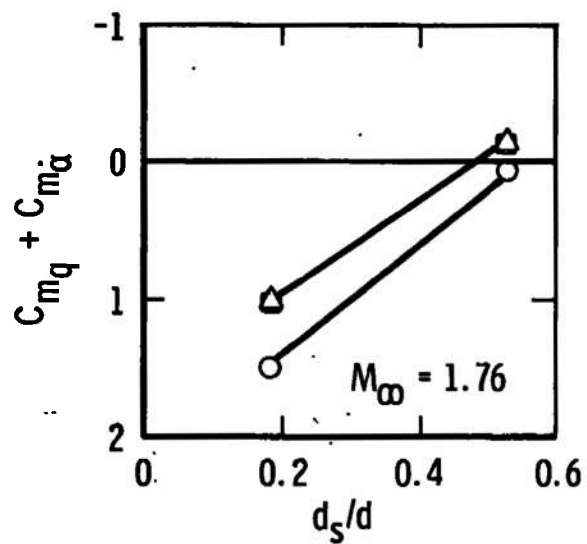


a. $\omega d/2V_\infty \approx 0.009 \text{ to } 0.007$

Fig. 13 Damping-in-Pitch Derivatives as a Function of Sting Diameter, BLDT Config., $l_s/d = 3.55$



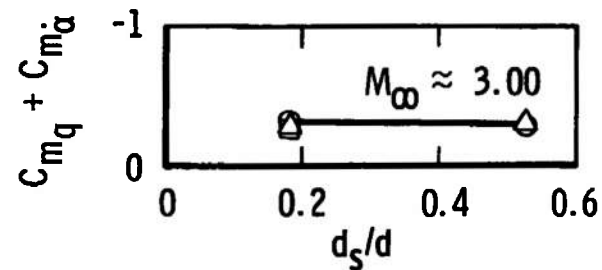
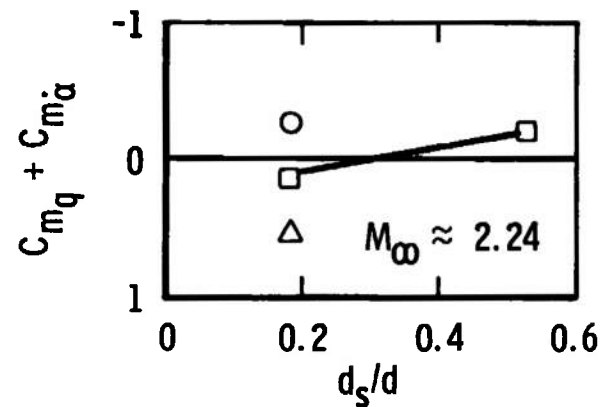
b. $\omega d/2V_\infty \approx 0.021 \text{ to } 0.019$
 Fig. 13 Continued



Sym $\approx Re_d \times 10^{-6}$

○ 0.25
 □ 0.75
 △ 1.24

$\alpha \approx 0$
 $\theta = \pm 1.8 \text{ deg}$

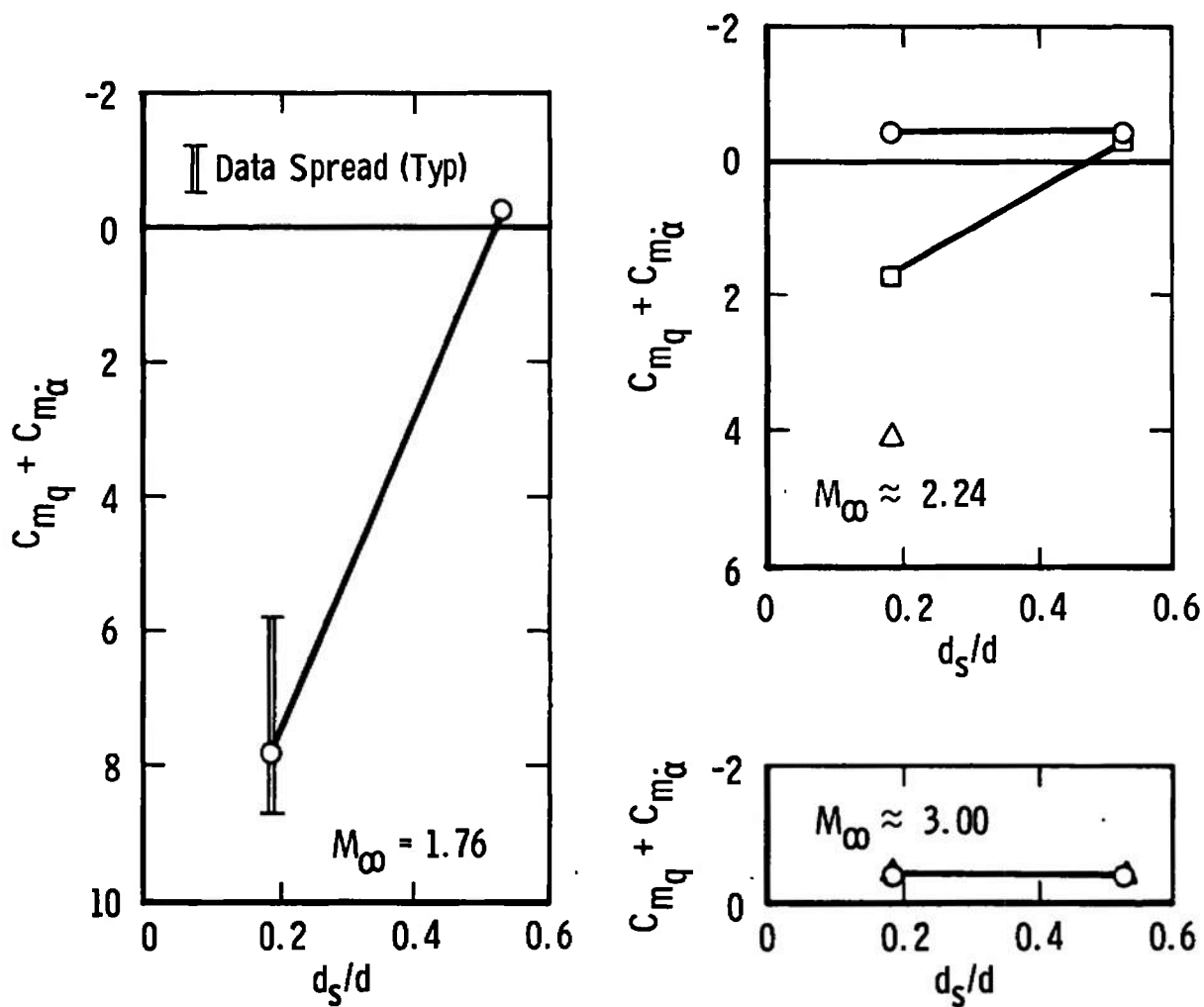


c. $\omega d/2V_\infty \approx 0.033 \text{ to } 0.025$
 Fig. 13 Concluded

Sym	$\approx Re_d \times 10^{-6}$
○	0.25
□	0.75
△	1.24

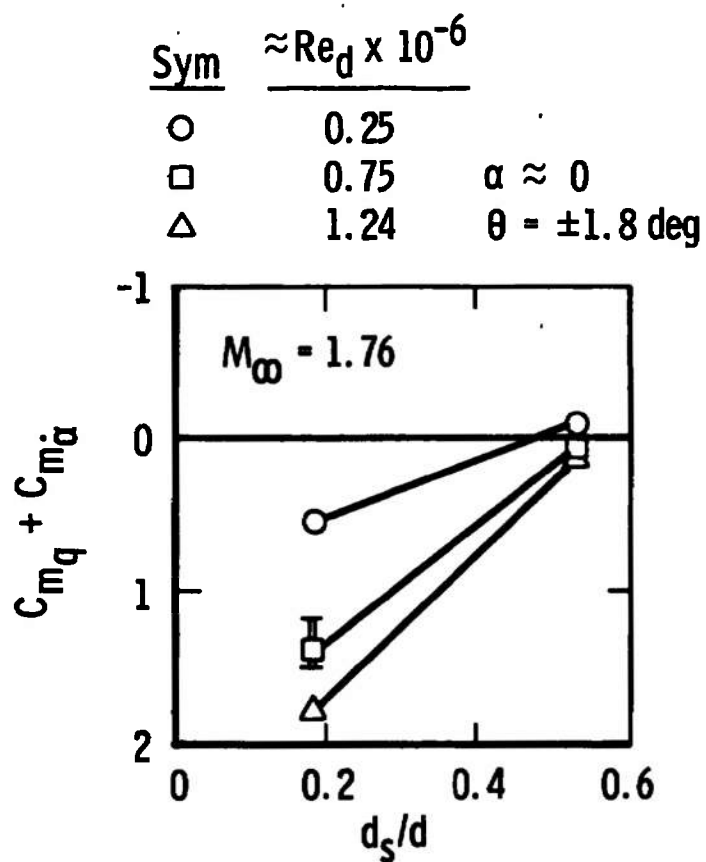
$$\alpha \approx 0$$

$$\theta = \pm 1.8 \text{ deg}$$



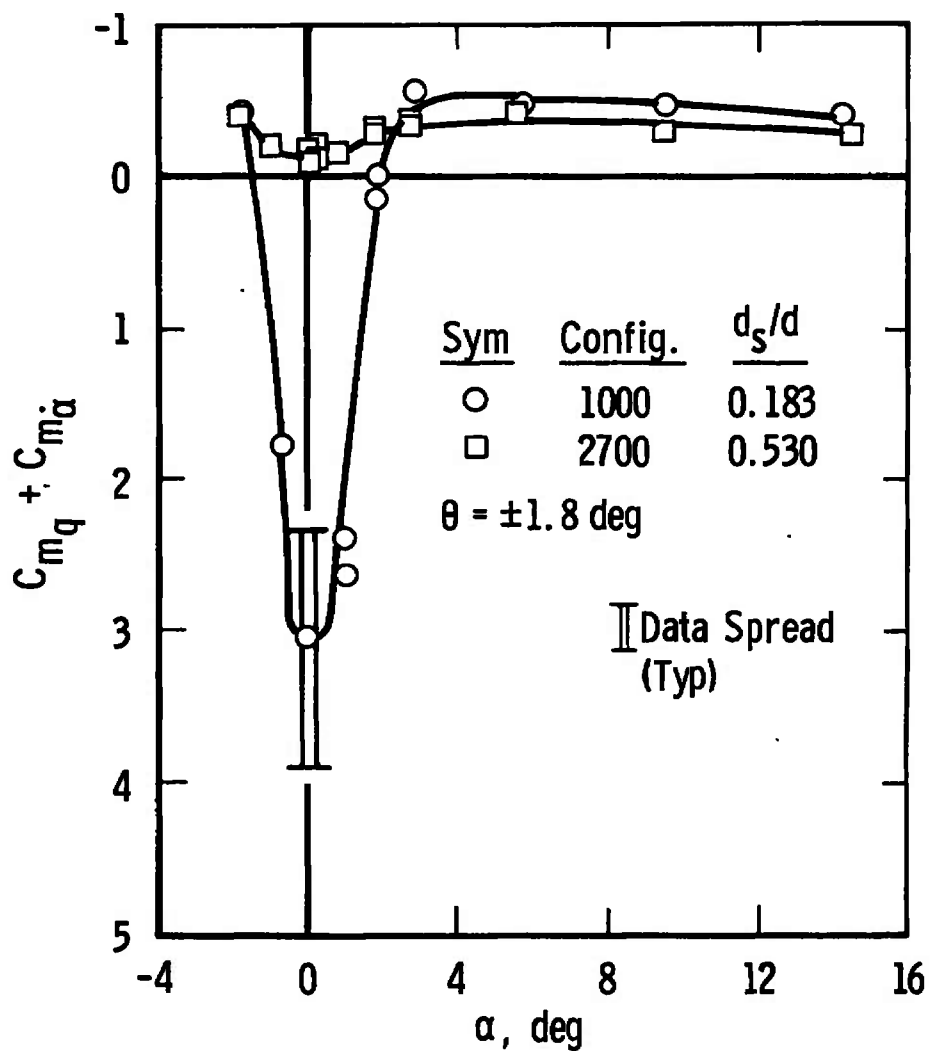
$$a. \omega d/2V_\infty \approx 0.009 \text{ to } 0.007$$

Fig. 14 Damping-in-Pitch Derivatives as a Function of Sting Diameter, BLDT Config., $\ell_s/d = 1.50$



b. $\omega d/2V_\infty \approx 0.022$

Fig. 14 Concluded



a. $\omega d/2V_\infty \approx 0.0087$

Fig. 15 Effect of Sting Diameter on the Damping-in-Pitch Derivatives as a Function of Angle of Attack, $M_\infty = 1.76$, $Re_d \approx 0.26 \times 10^6$, $l_s/d = 3.55$

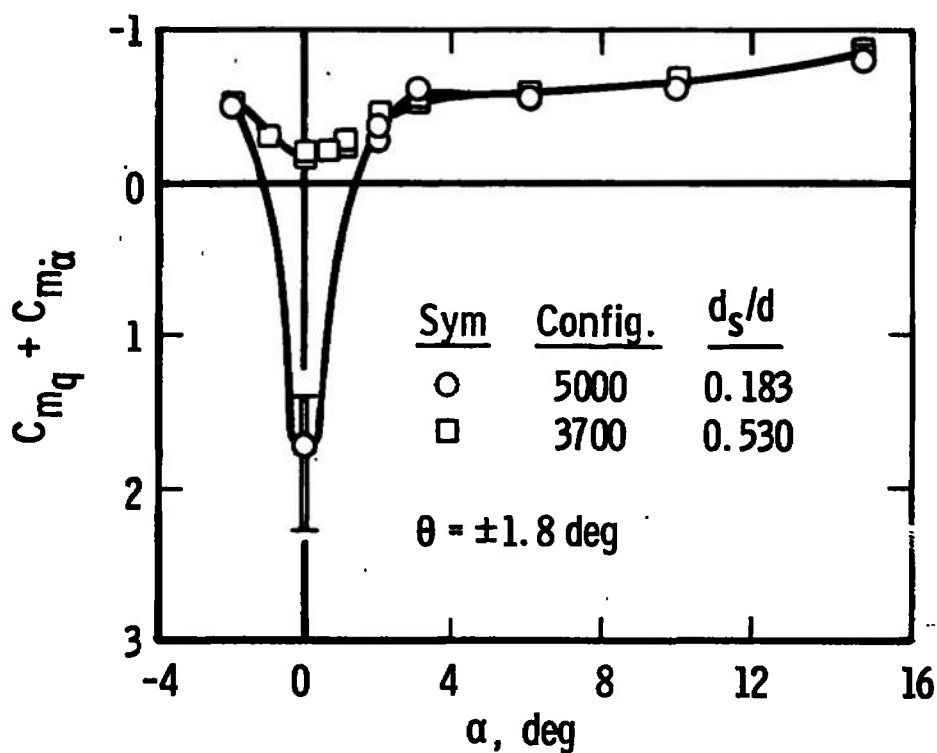
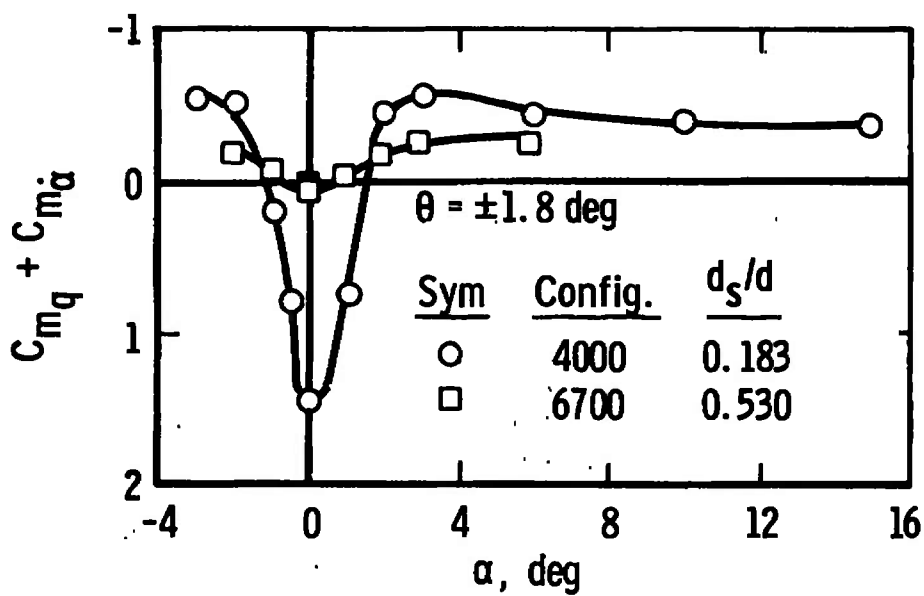
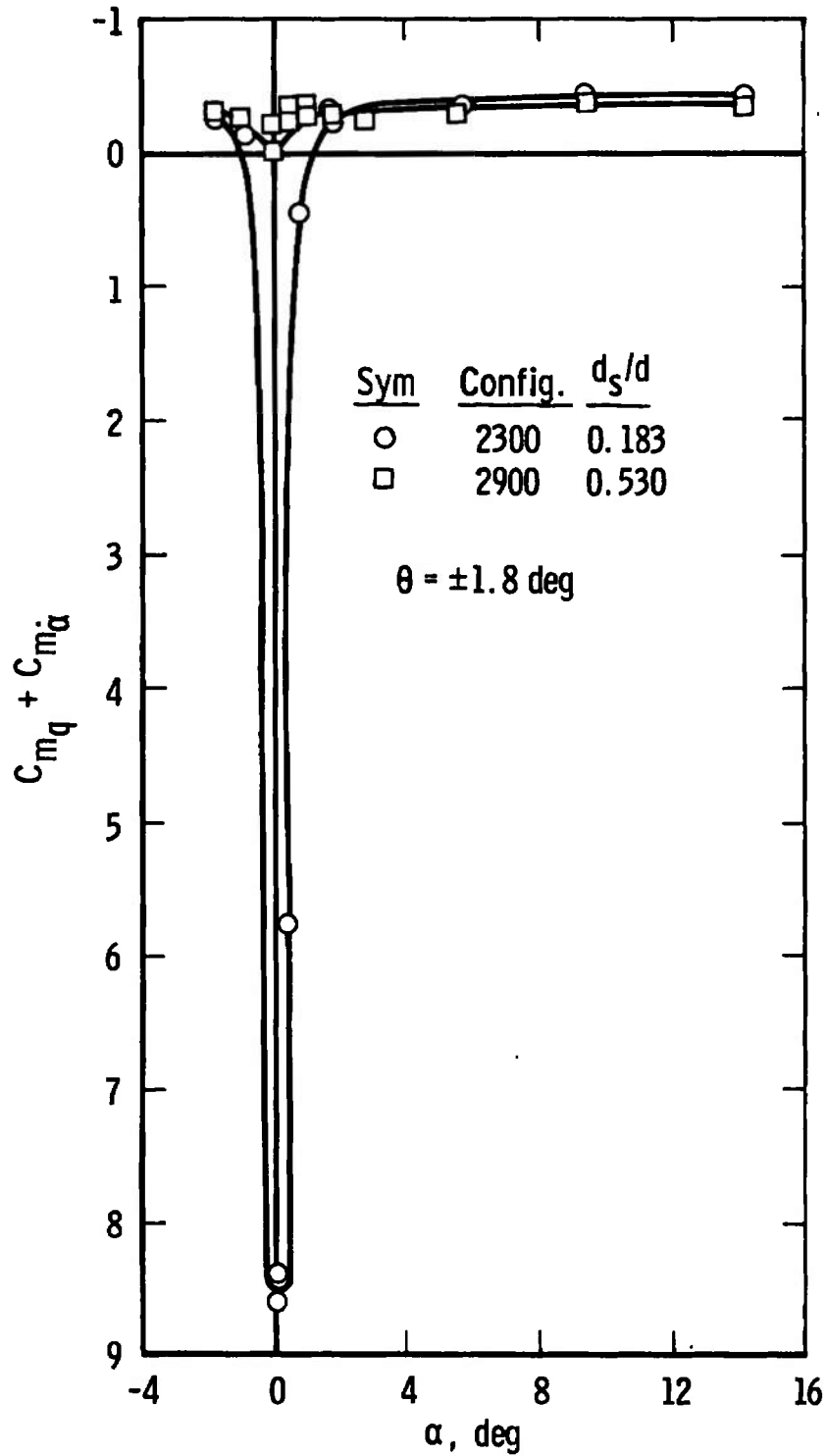
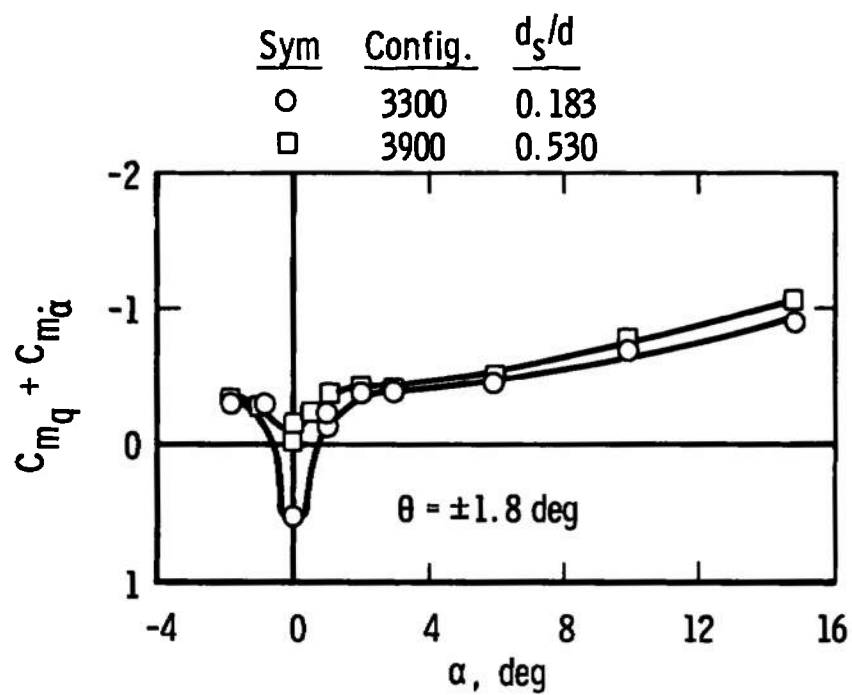
b. $\omega d/2V_\infty \approx 0.021$ c. $\omega d/2V_\infty \approx 0.032$

Fig. 15 Concluded



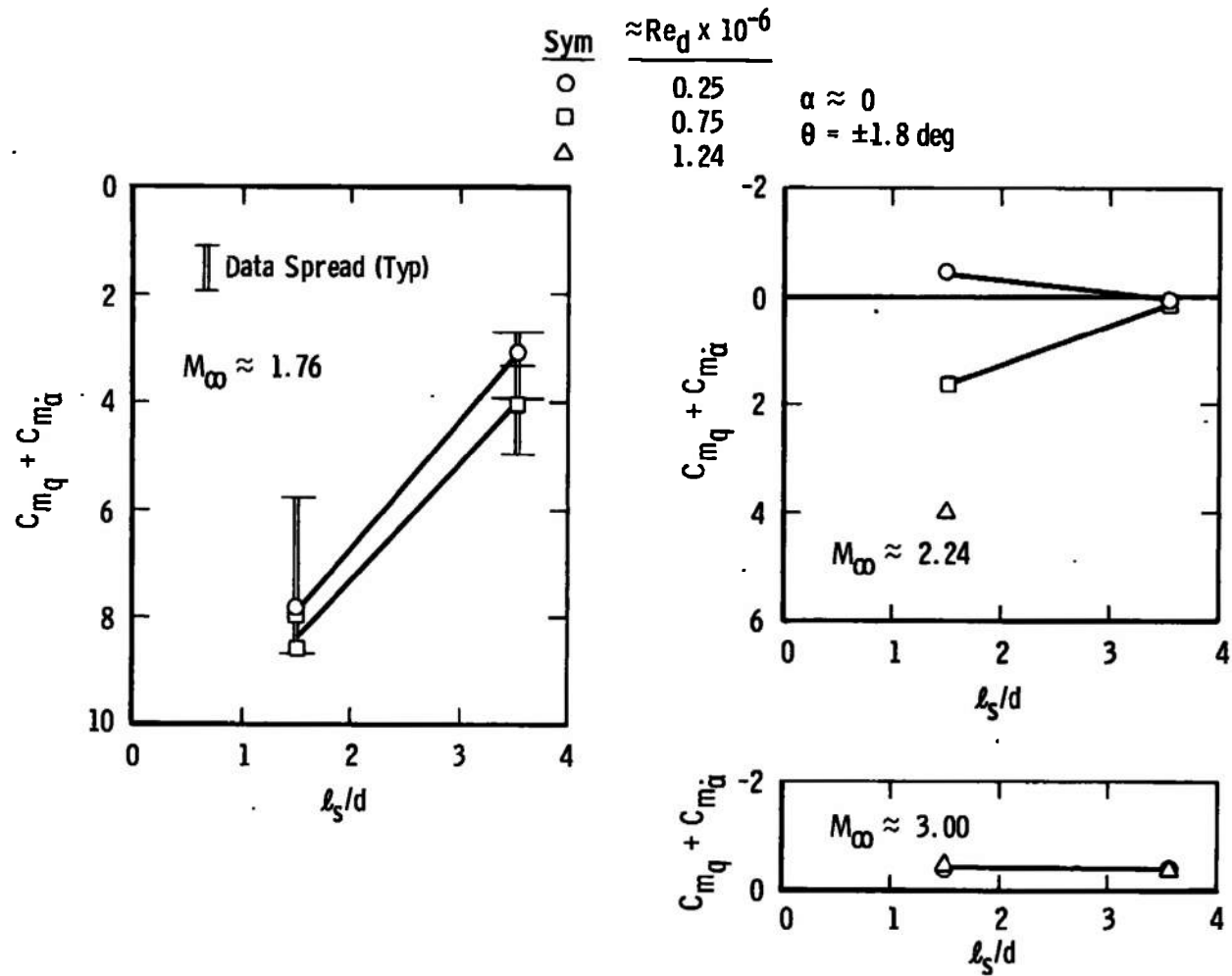
a. $\omega d/2V_\infty \approx 0.0087$

Fig. 16 Effect of Sting Diameter on the Damping-in-Pitch Derivatives as a Function of Angle of Attack,
 $M_\infty = 1.76$, $Re_d \approx 0.26 \times 10^6$, $l_s/d = 1.50$

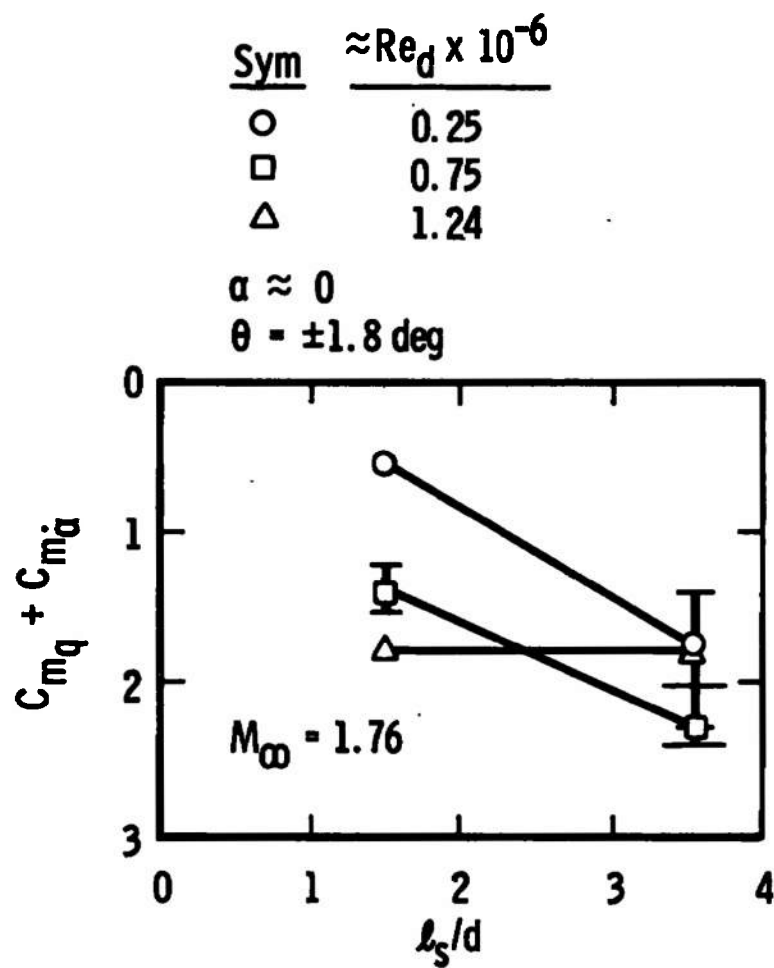


b. $\omega d/2V_\infty \approx 0.021$

Fig. 16 Concluded

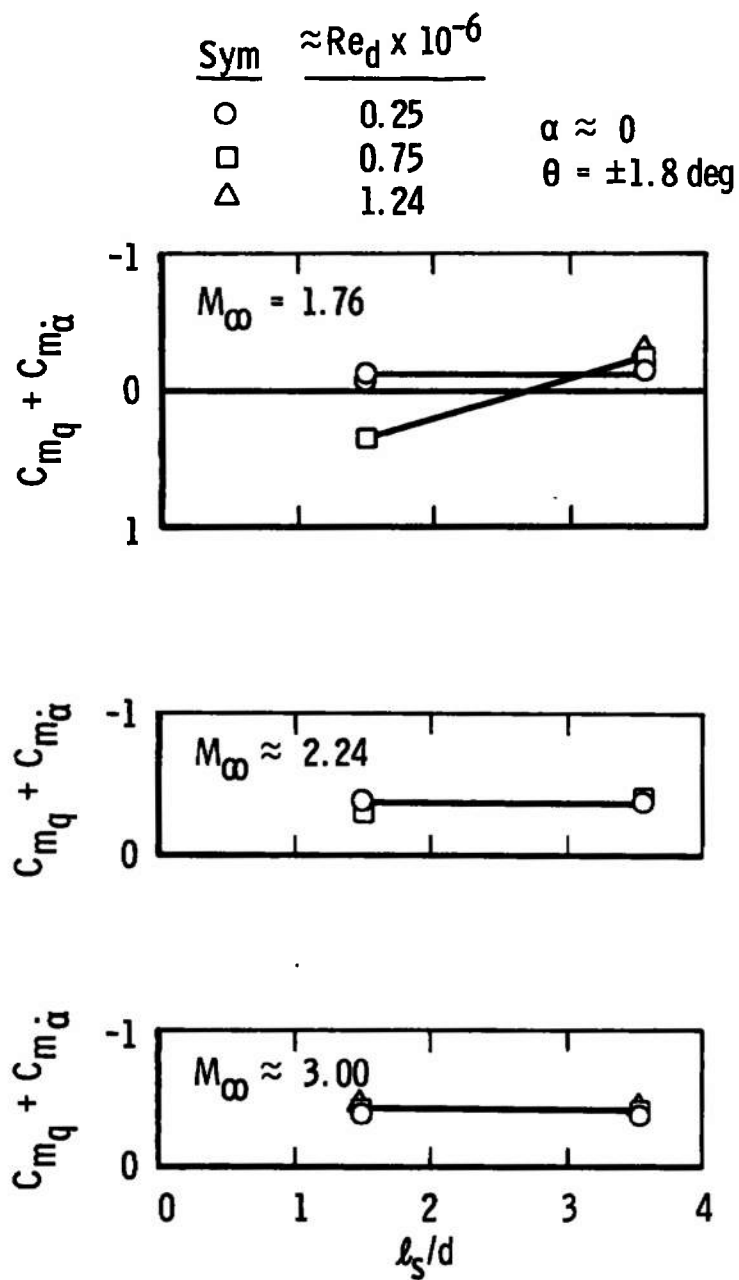


a. $\omega d/2V_\infty \approx 0.009$ to 0.007
**Fig. 17 Damping-in-Pitch Derivatives as a Function of Sting Length,
 BLDT Config., $d_s/d = 0.183$**



b. $\omega d/2V_\infty \approx 0.022$

Fig. 17 Concluded



a. $\omega d/2V_\infty \approx 0.009 \text{ to } 0.007$

Fig. 18 Damping-in-Pitch Derivatives as a Function of Sting Length,
BLDT Config., $d_s/d = 0.530$

Sym	$\approx Re_d \times 10^{-6}$
-----	-------------------------------

○	0.25
---	------

□	0.75
---	------

△	1.24
---	------

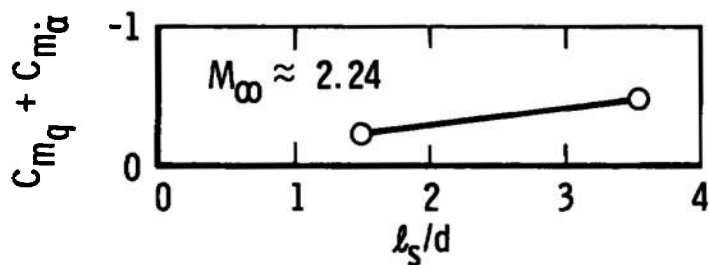
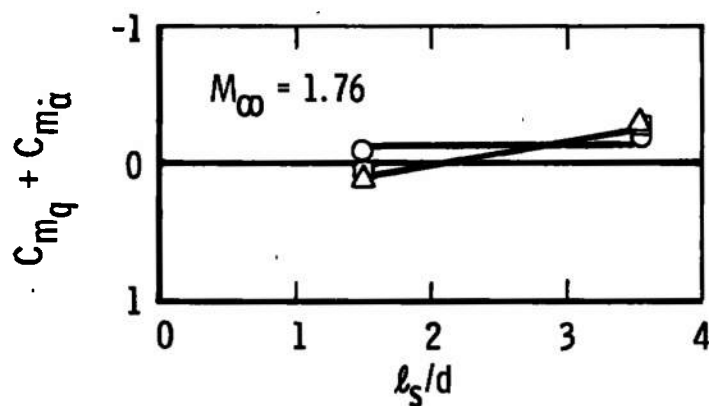
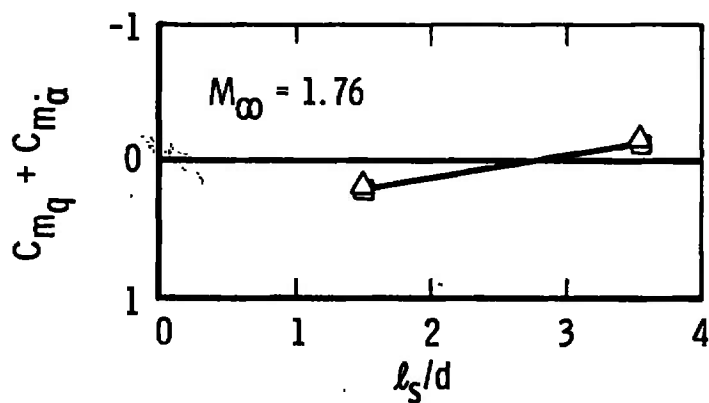
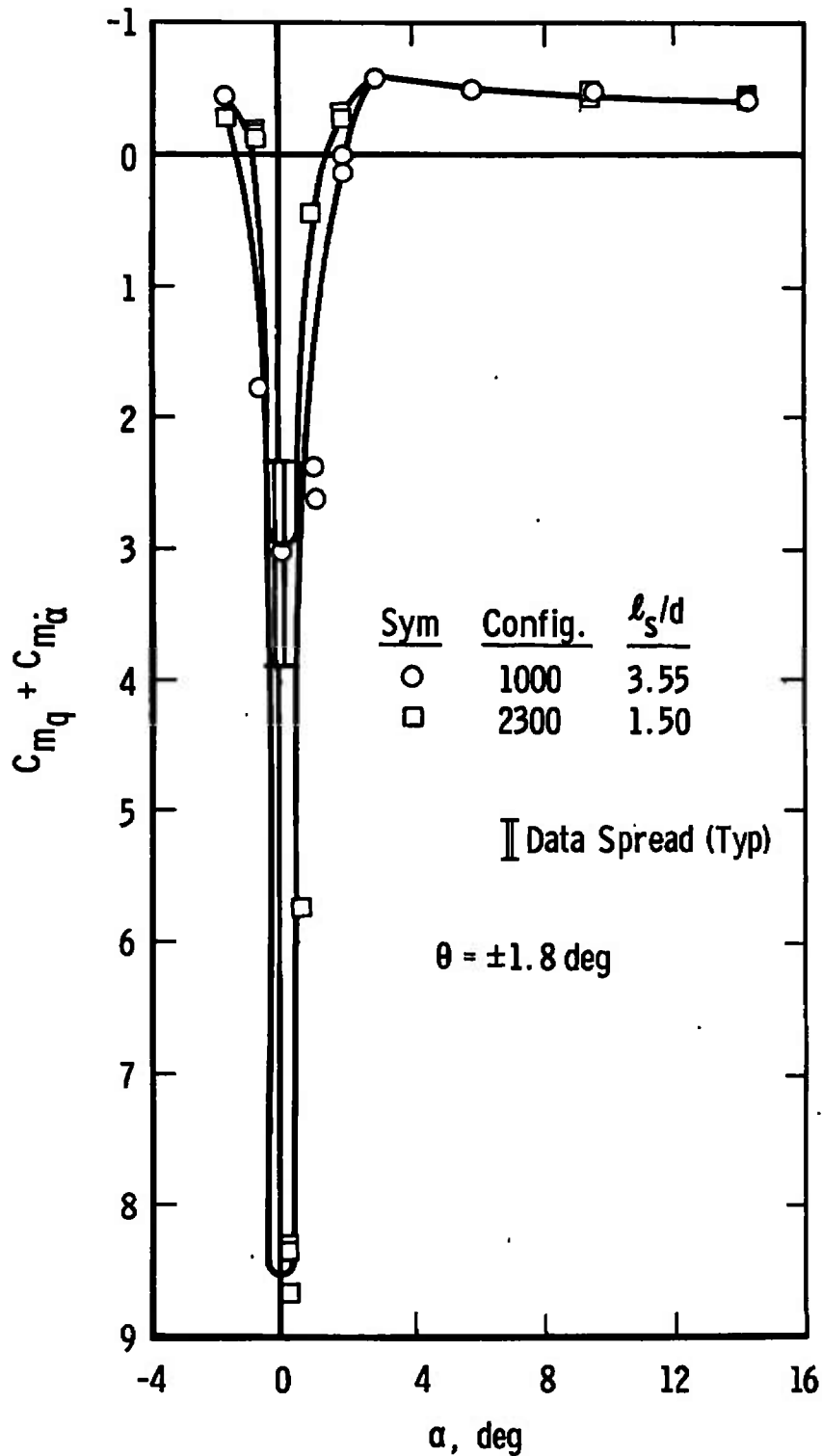
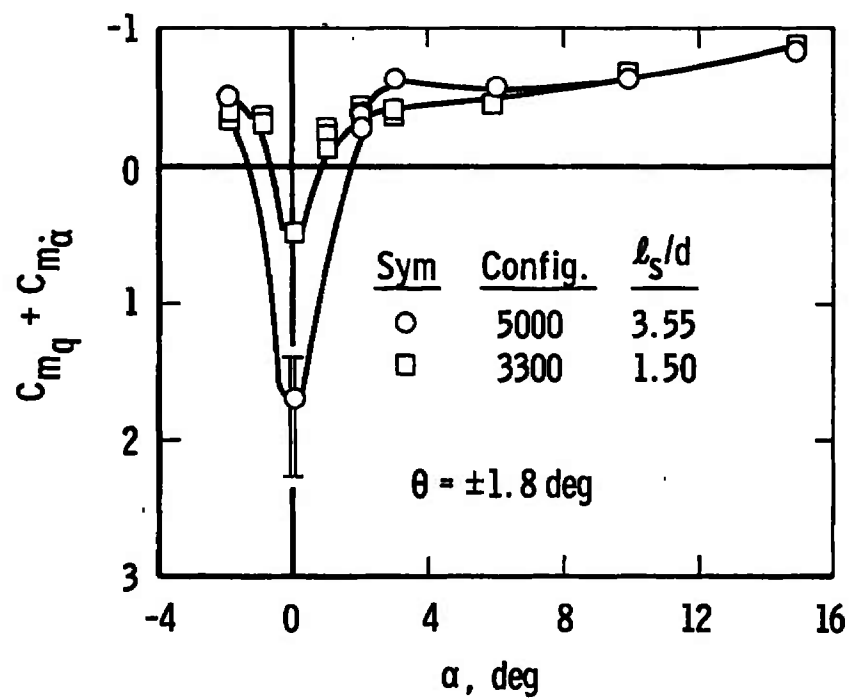
 $\alpha \approx 0$ $\theta = \pm 1.8 \text{ deg}$ b. $\omega d/2V_\infty \approx 0.022 \text{ to } 0.019$ c. $\omega d/2V_\infty \approx 0.033$

Fig. 18 Concluded



a. $\omega d/2V_\infty \approx 0.0087$

Fig. 19 Effect of Sting Length on the Damping-in-Pitch Derivatives as a Function of Angle of Attack, BLDT Config., $M_\infty = 1.76$, $Re_d \approx 0.26 \times 10^6$, $d_s/d = 0.183$



b. $\omega d/2V_\infty \approx 0.021$
 Fig. 19 Concluded

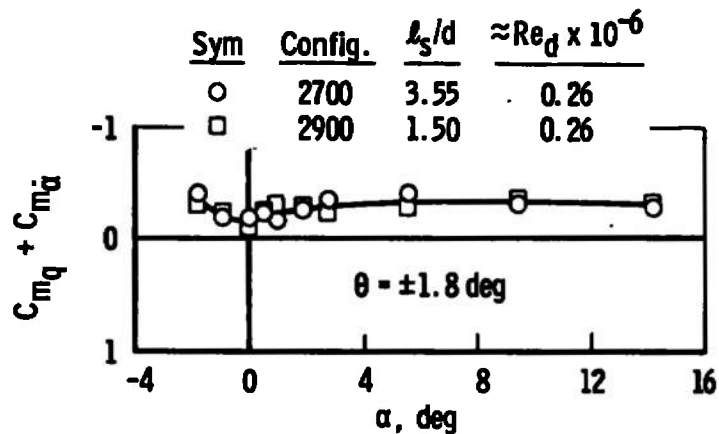
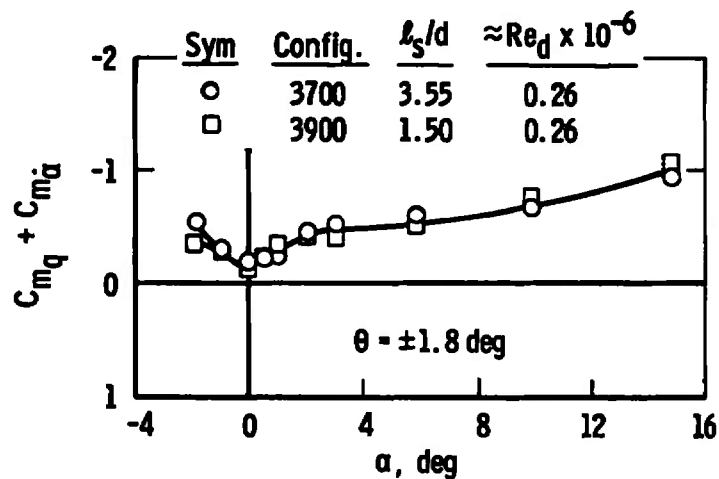
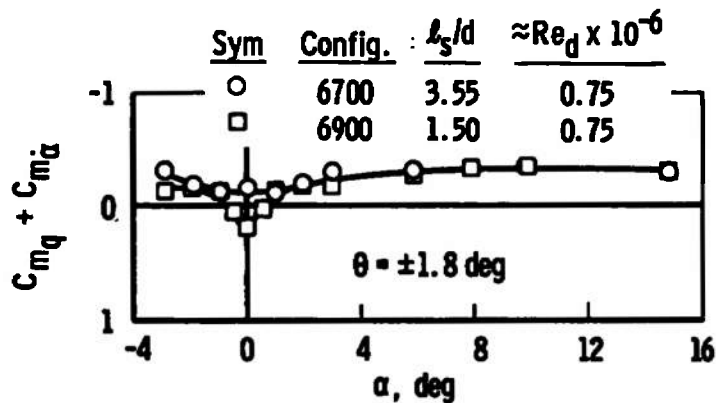
a. $\omega d/2V_\infty \approx 0.0087$ b. $\omega d/2V_\infty \approx 0.021$ c. $\omega d/2V_\infty \approx 0.032$

Fig. 20 Effect of Sting Length on the Damping-in-Pitch Derivatives as a Function of Angle of Attack, BLDT Config., $M_\infty = 1.76$, $d_s/d = 0.530$

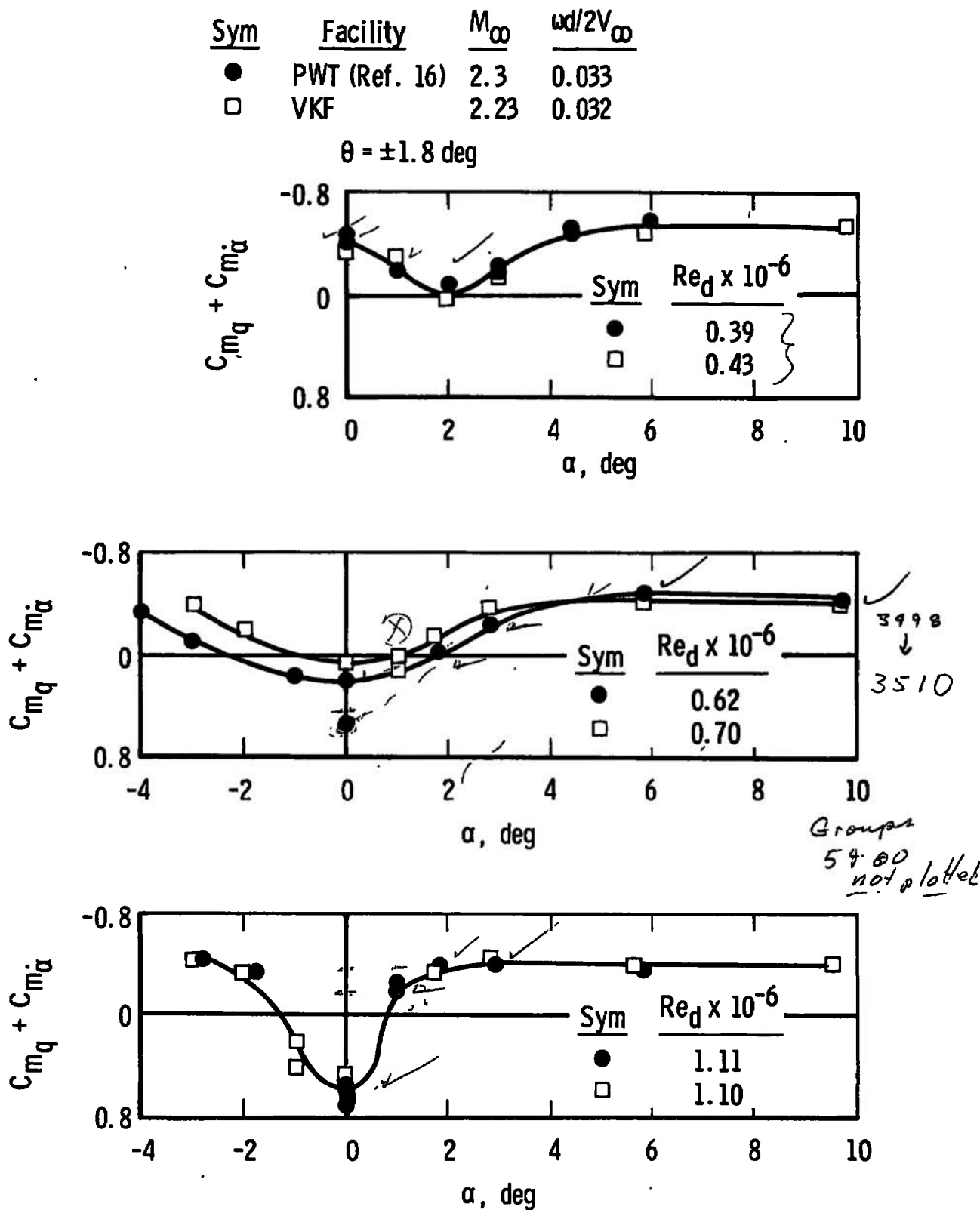


Fig. 21 Comparison of PWT and VKF Data at Various Angles of Attack, Config. 721M

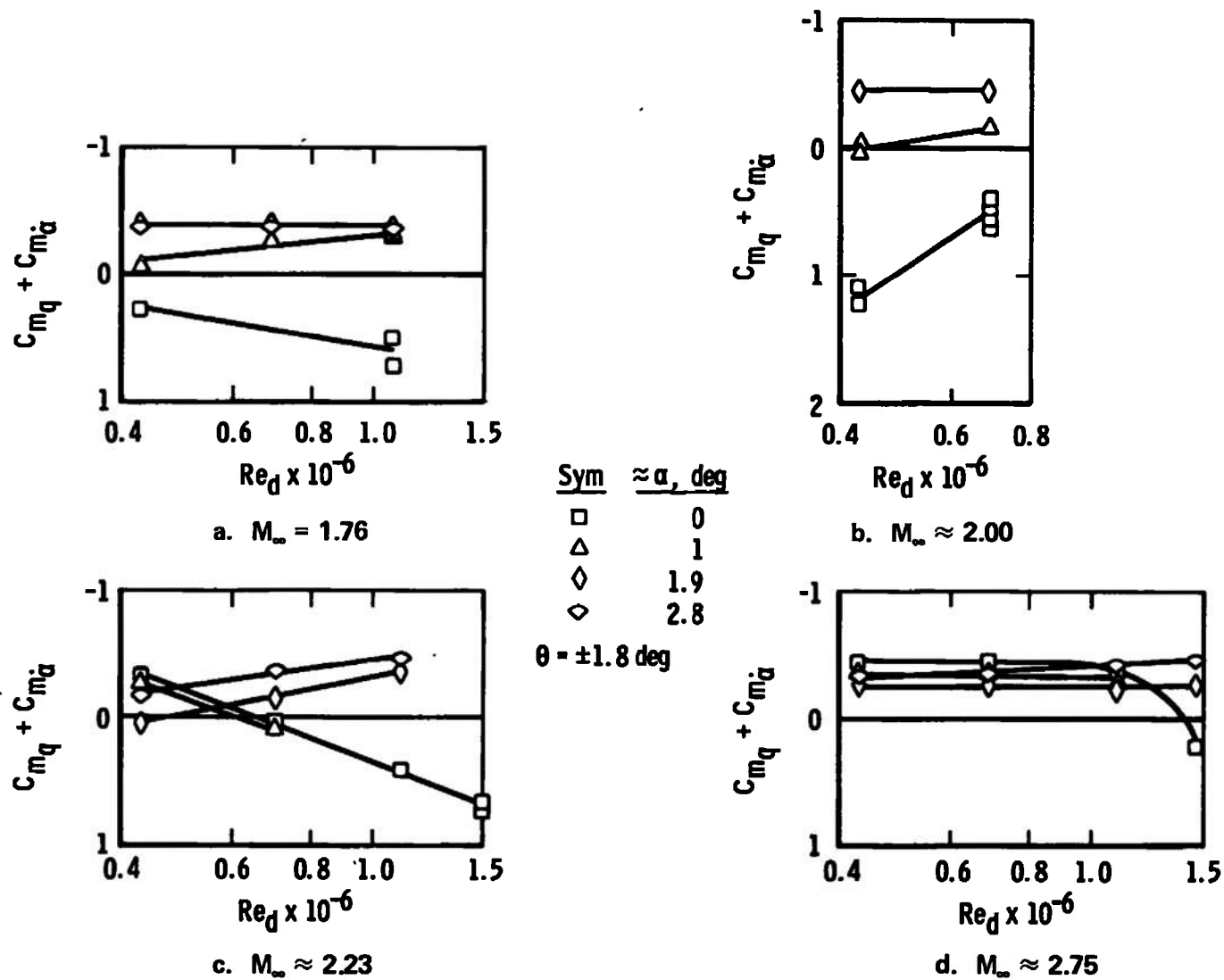


Fig. 22 Damping-in-Pitch Derivatives as a Function of Reynolds Number, Config. 721M

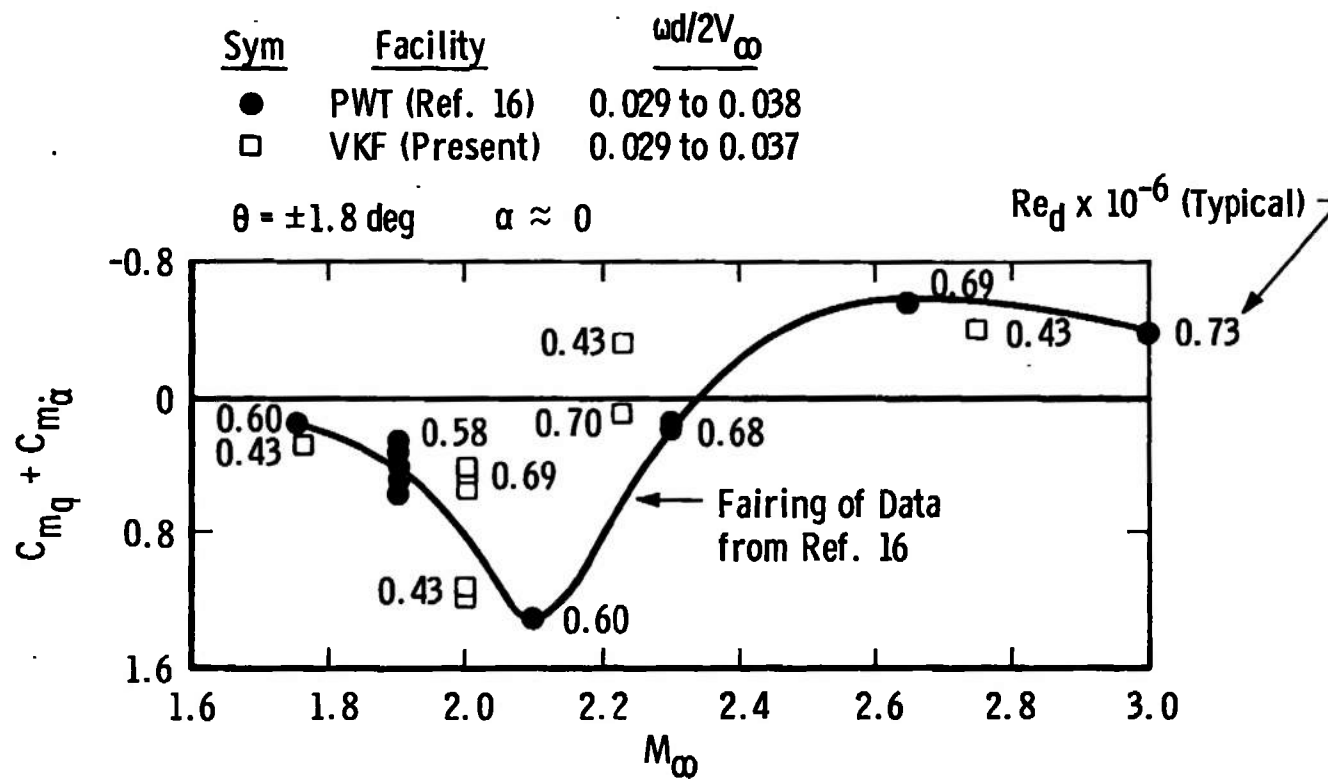


Fig. 23 Comparison of PWT and VKF Data at Various Mach Numbers, Config. 721M

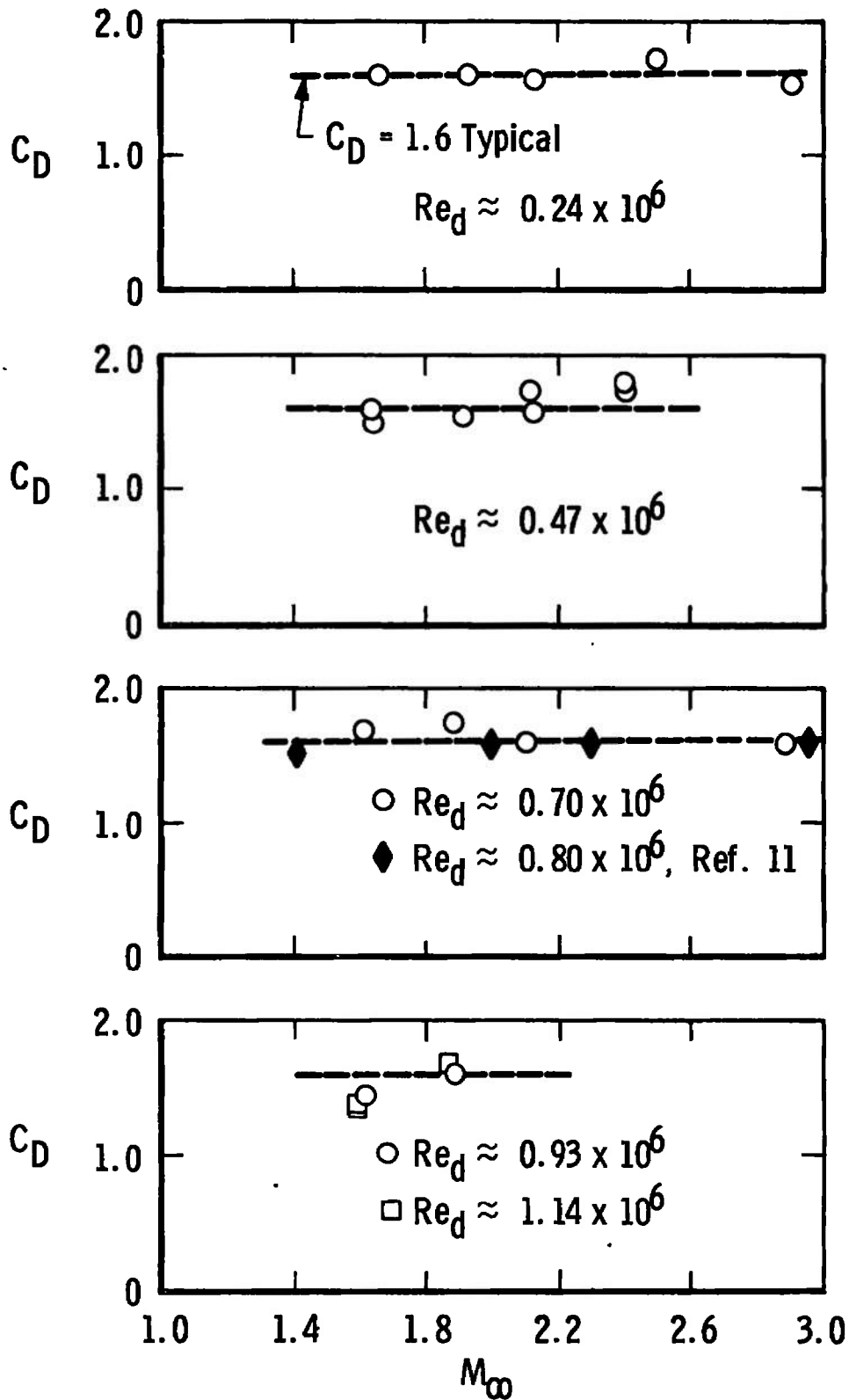


Fig. 24 Drag Coefficient as a Function of Mach Number, BLDT Config.

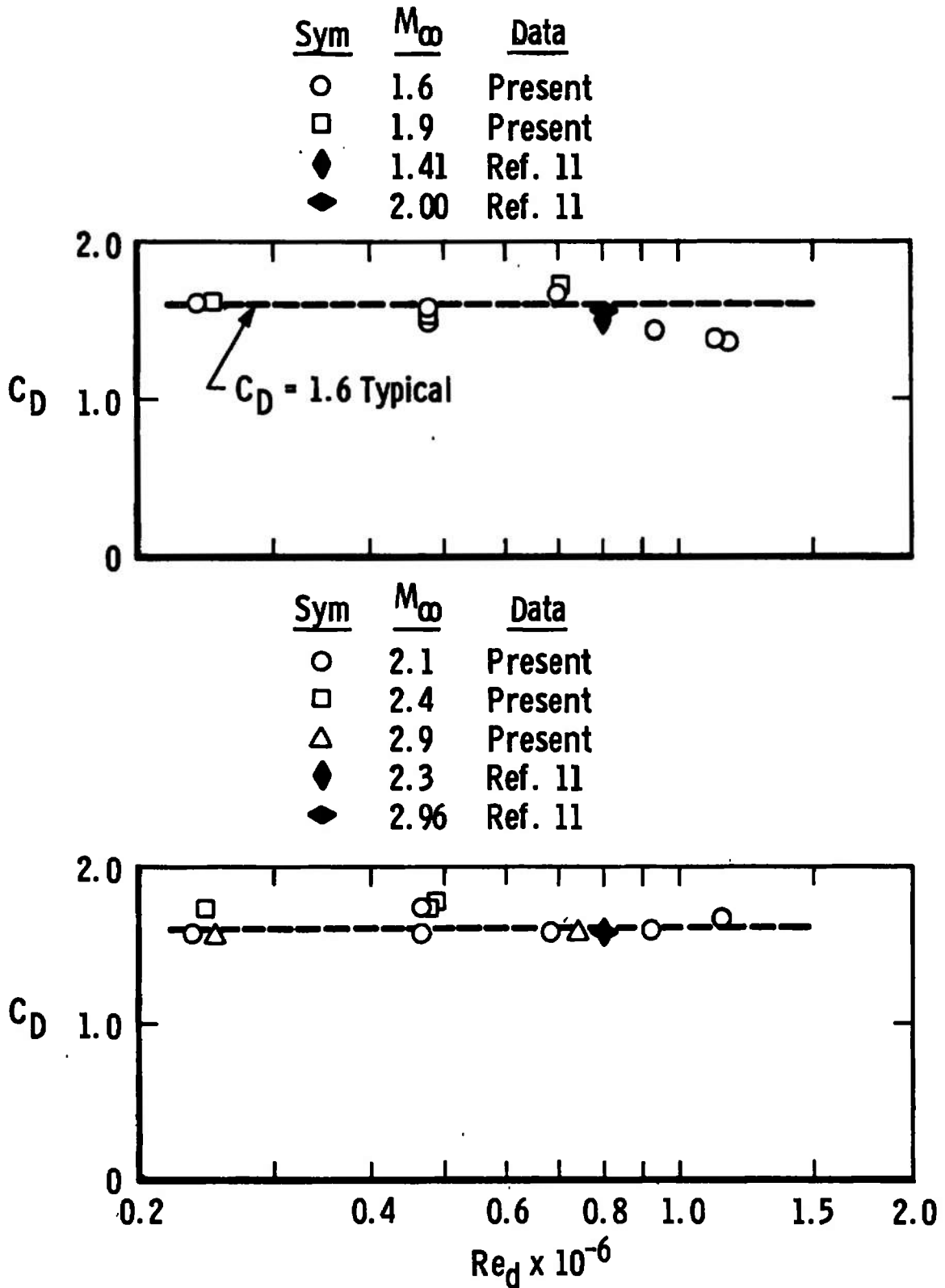
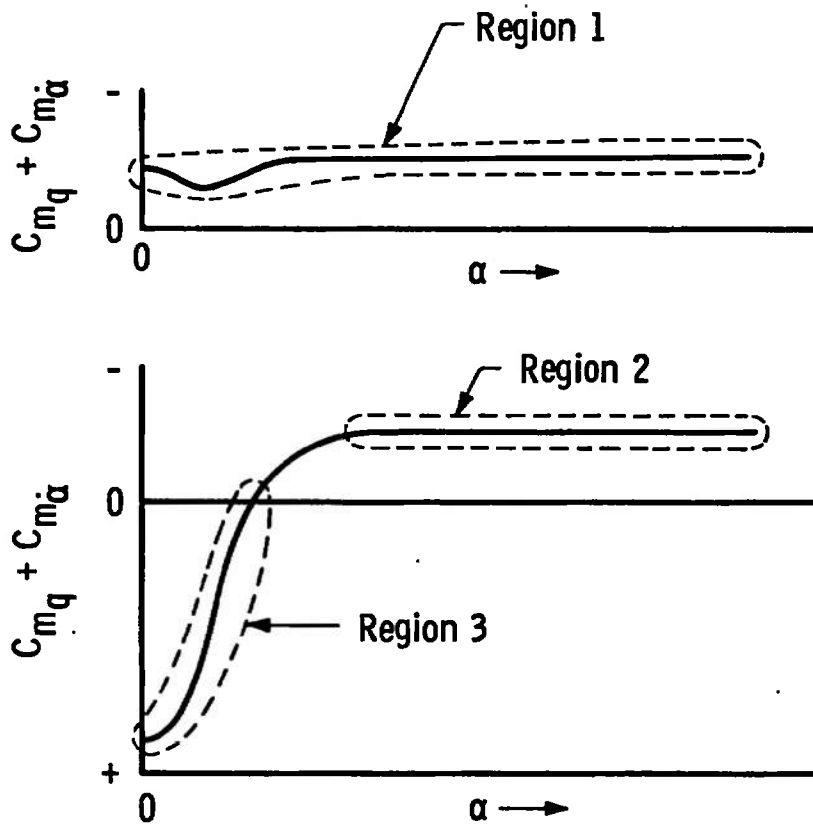
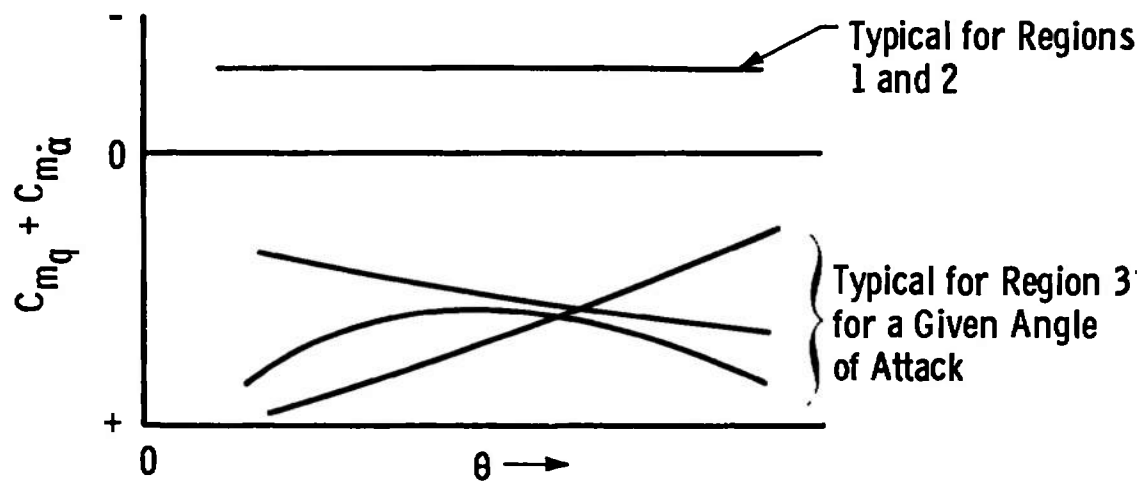


Fig. 25 Drag Coefficient as a Function of Reynolds Number, BLDT Config.

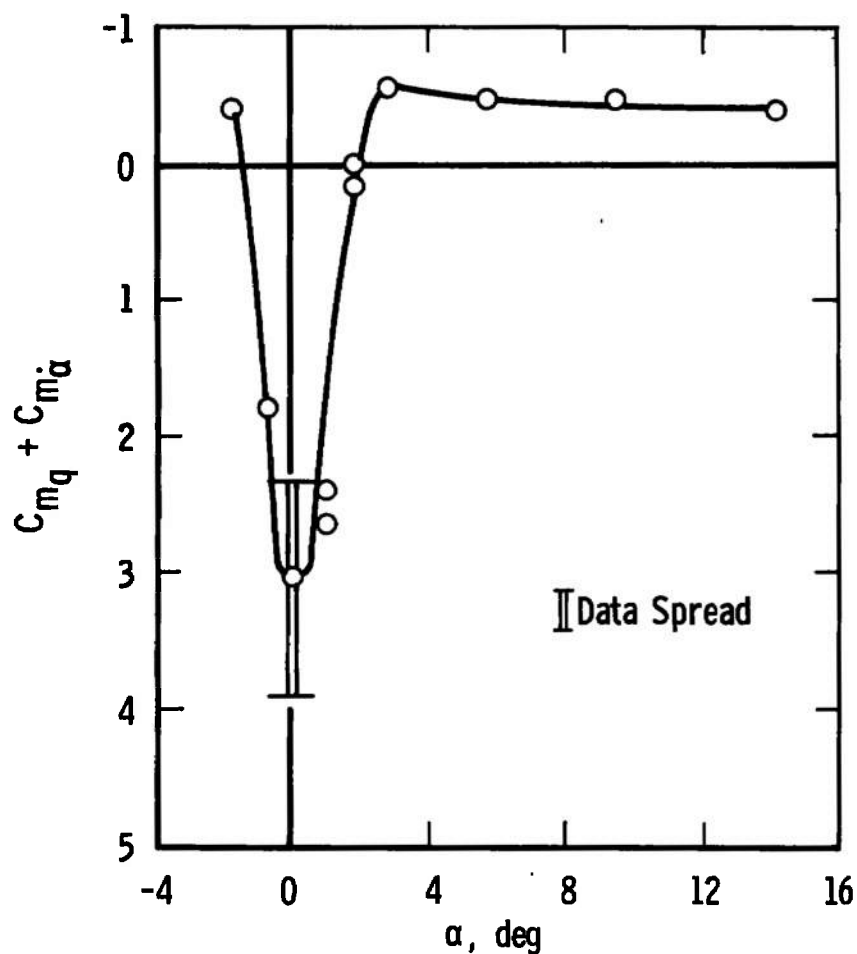


a. Damping Derivatives as a Function of α , $\theta = \text{constant}$

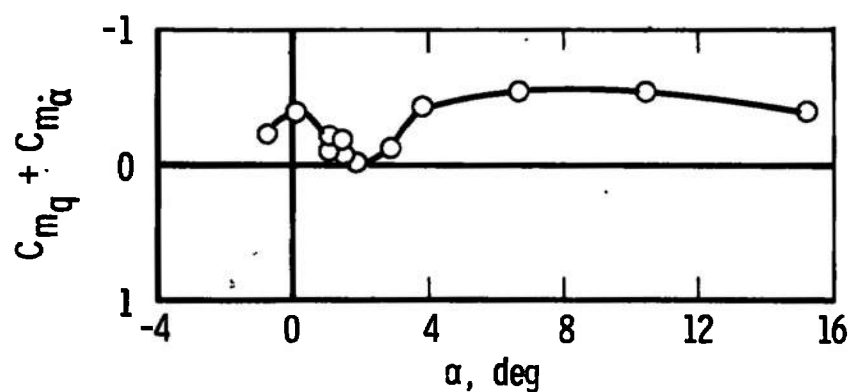


b. Damping Derivatives as a Function of θ , $\alpha = \text{constant}$

Fig. 26 Representative Damping Derivatives as a Function of Amplitude of Oscillation, θ



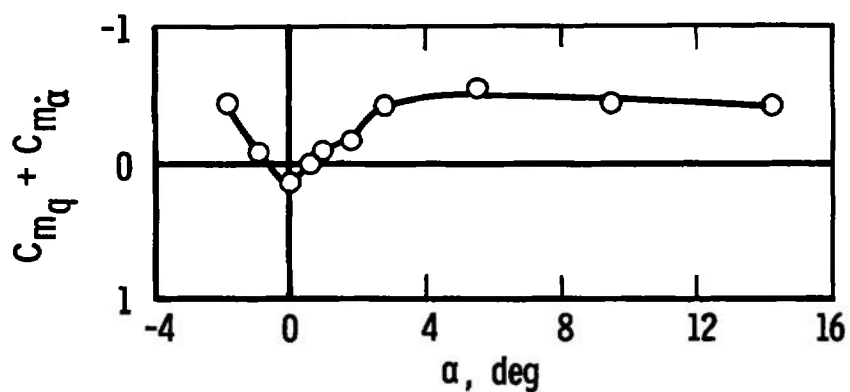
a. $M_\infty = 1.76$, $\omega d/2V_\infty \approx 0.0087$



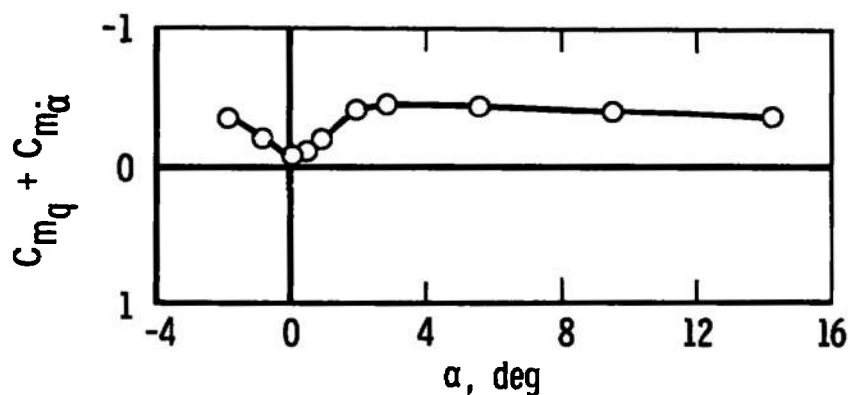
$\theta = \pm 1.8 \text{ deg}$
 $l_s/d = 3.55$
 $d_s/d = 0.183$

b. $M_\infty = 2.00$, $\omega d/2V_\infty \approx 0.0077$

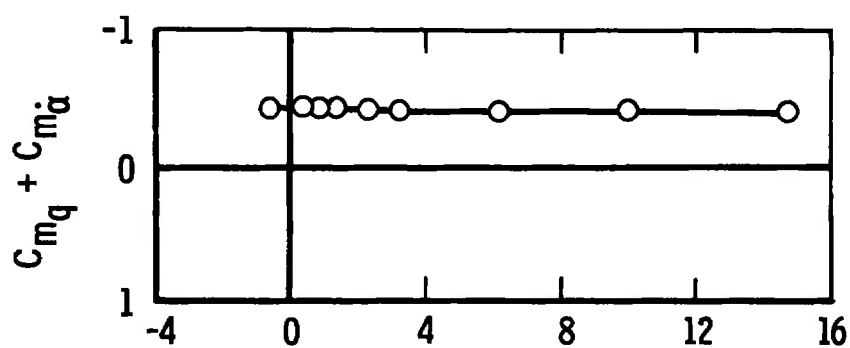
Fig. 27 Damping-in-Pitch Derivatives as a Function of Angle of Attack, Config. 1000, $Re_d \approx 0.26 \times 10^6$



c. $M_\infty = 2.23$, $\omega d/2V_\infty \approx 0.0073$



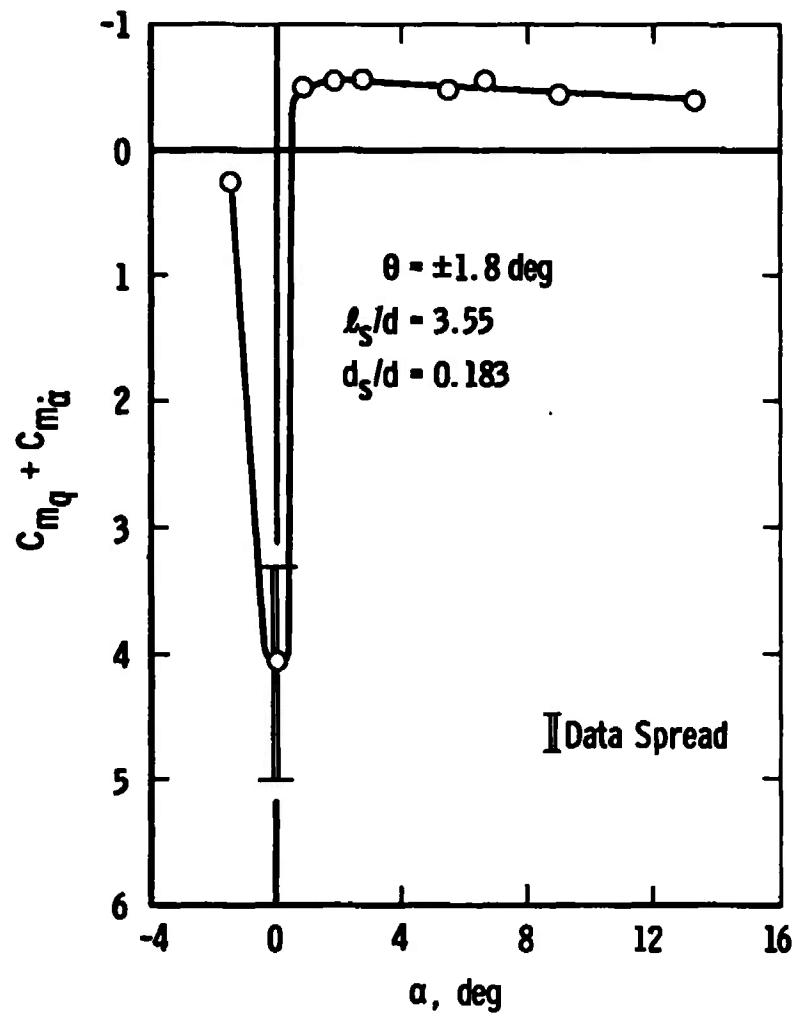
d. $M_\infty = 2.46$, $\omega d/2V_\infty \approx 0.0070$



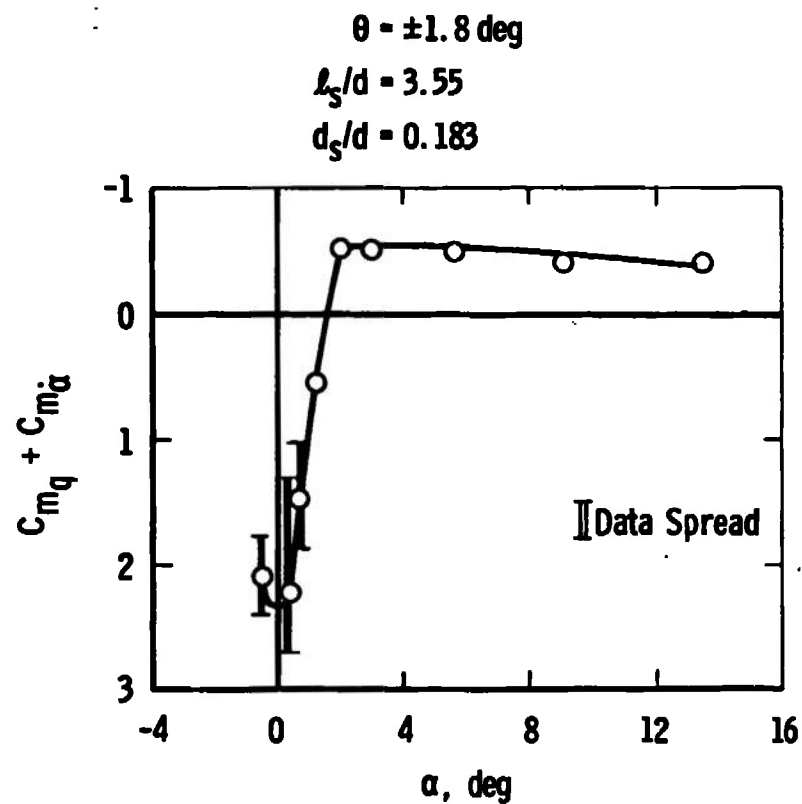
e. $M_\infty = 2.99$, $\omega d/2V_\infty \approx 0.0064$

Fig. 27 Concluded

$\theta = \pm 1.8$ deg
 $l_s/d = 3.55$
 $d_s/d = 0.183$



a. $M_\infty = 1.76, \omega d/2V_\infty \approx 0.0093$



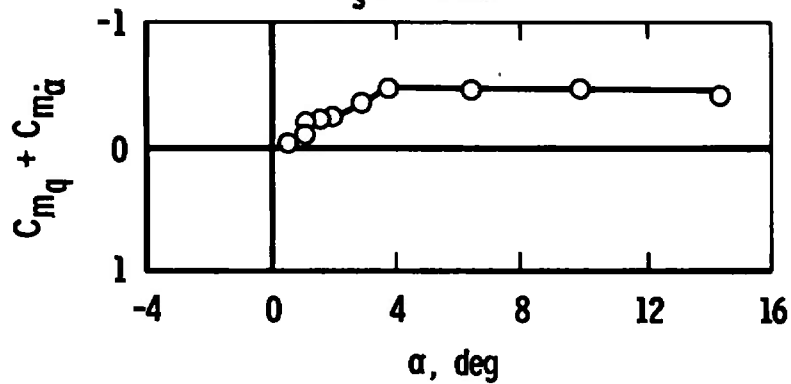
b. $M_\infty = 2.01, \omega d/2V_\infty \approx 0.0084$

Fig. 28 Damping-in-Pitch Derivatives as a Function of Angle of Attack,
 Config. 1000, $Re_d \approx 0.75 \times 10^6$

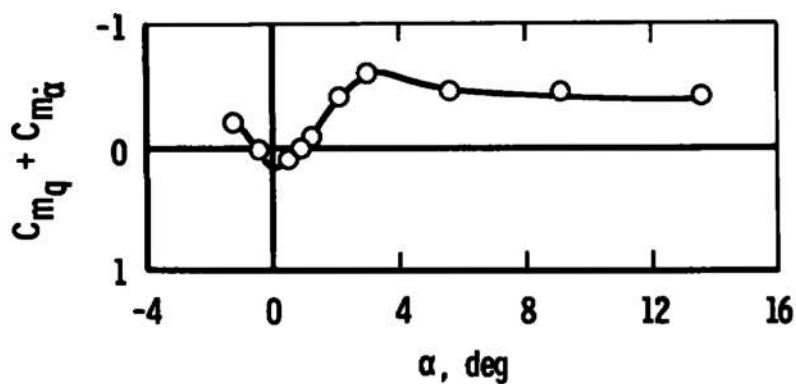
$$\theta = \pm 1.8 \text{ deg}$$

$$l_s/d = 3.55$$

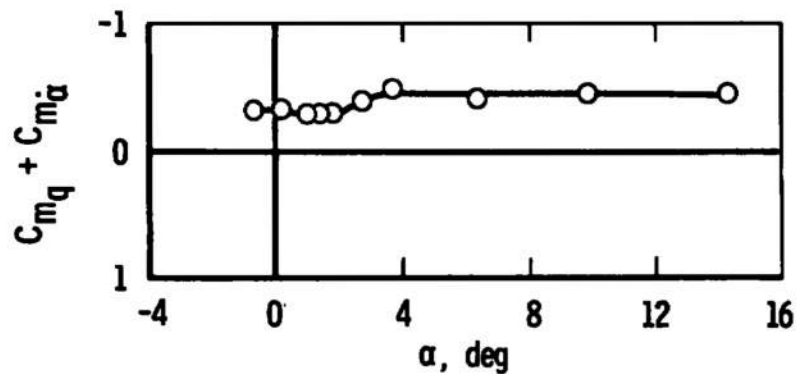
$$d_s/d = 0.183$$



$$c. M_\infty = 2.23, \omega d/2V_\infty \approx 0.0080$$

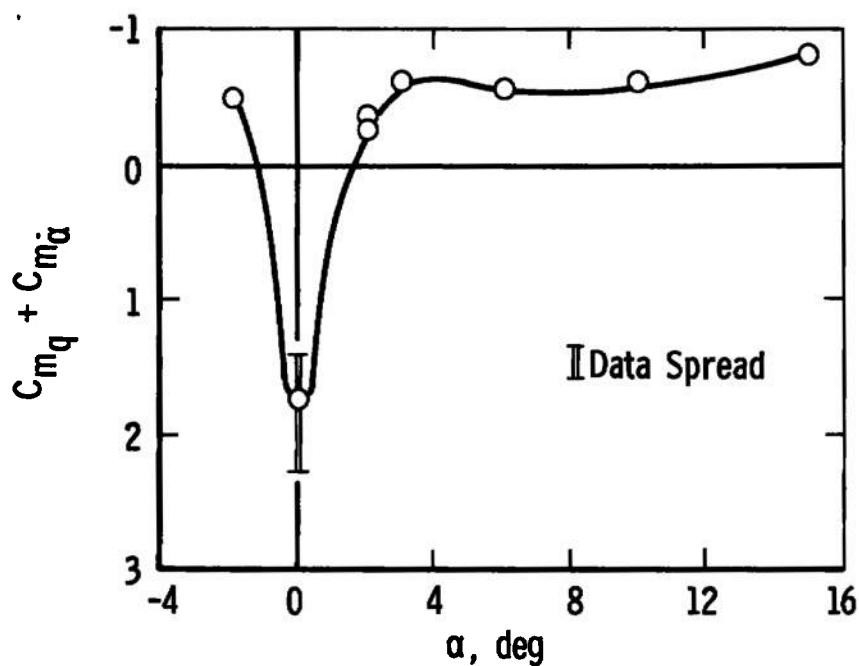


$$d. M_\infty = 2.48, \omega d/2V_\infty \approx 0.0075$$

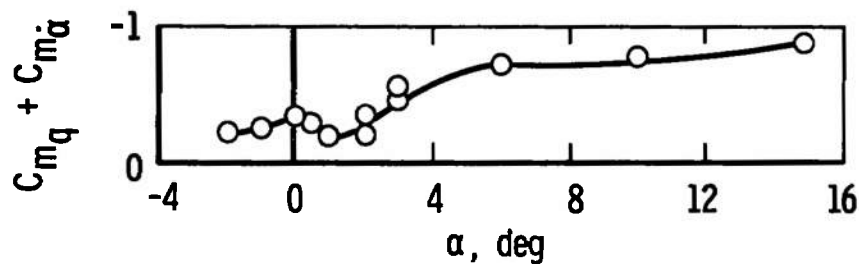


$$e. M_\infty = 3.00, \omega d/2V_\infty \approx 0.0069$$

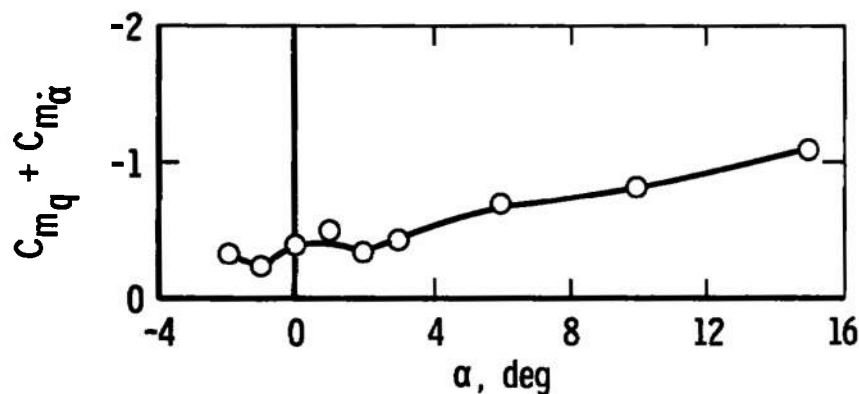
Fig. 28 Concluded



a. $M_\infty = 1.76, \omega d/2V_\infty \approx 0.021$

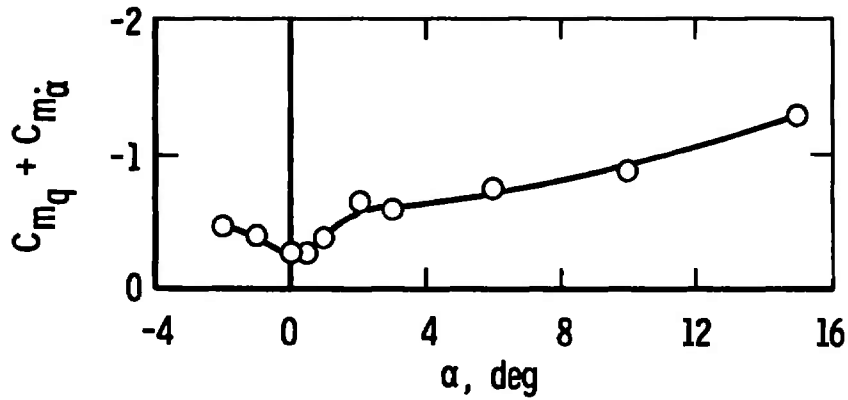


b. $M_\infty = 2.00, \omega d/2V_\infty \approx 0.020$

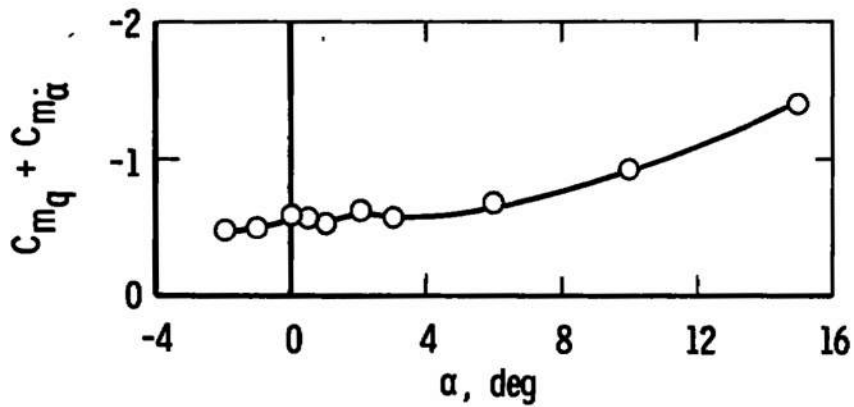


c. $M_\infty = 2.23, \omega d/2V_\infty \approx 0.019$

Fig. 29 Damping-in-Pitch Derivatives as a Function of Angle of Attack,
 Config. 5000, $Re_d \approx 0.26 \times 10^6$

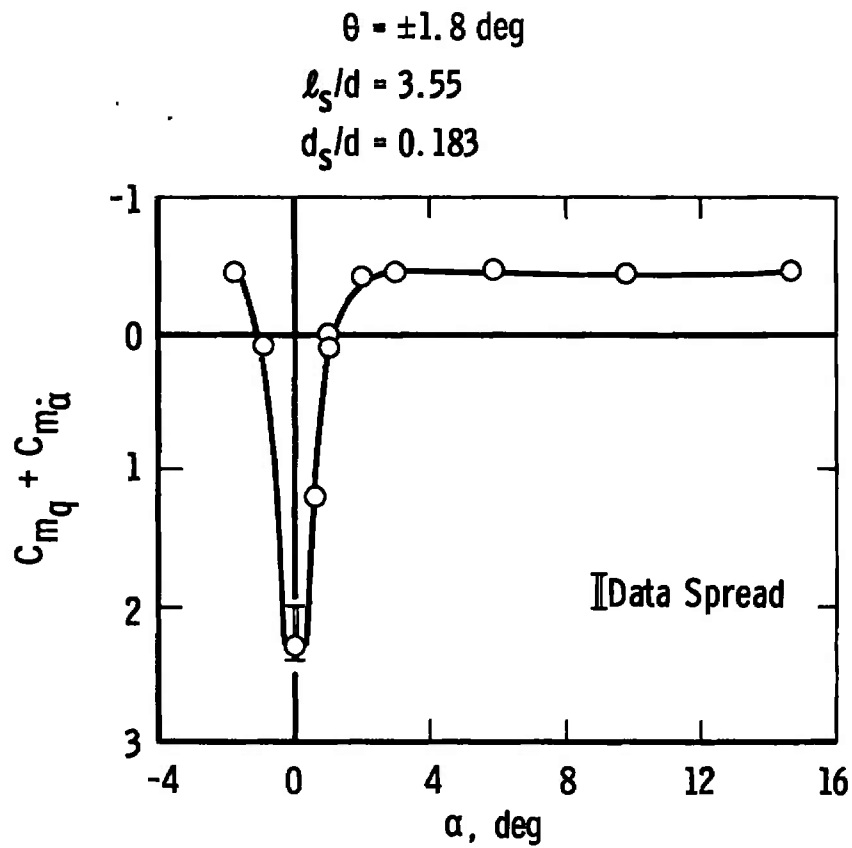
$\theta = \pm 1.8 \text{ deg}$
 $l_s/d = 3.55$
 $d_s/d = 0.183$


d. $M_\infty = 2.48$, $\omega d/2V_\infty \approx 0.018$

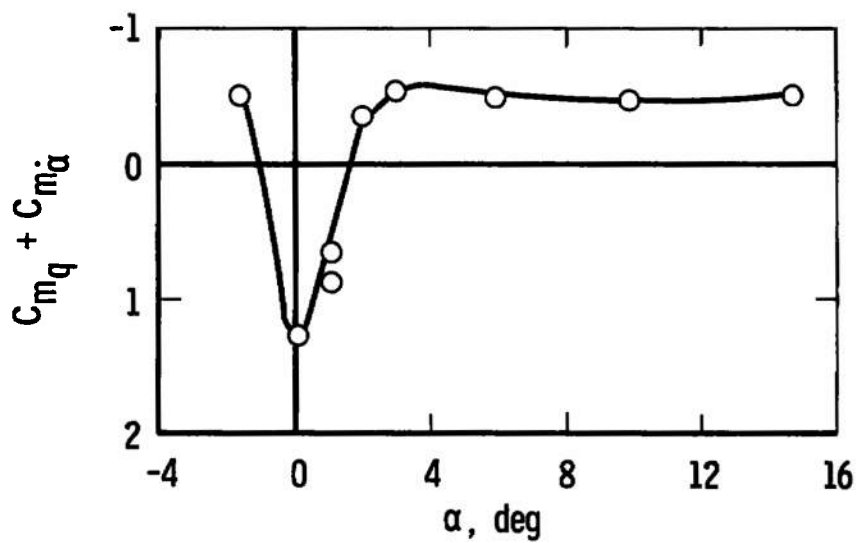


e. $M_\infty = 2.97$, $\omega d/2V_\infty \approx 0.016$

Fig. 29 Concluded

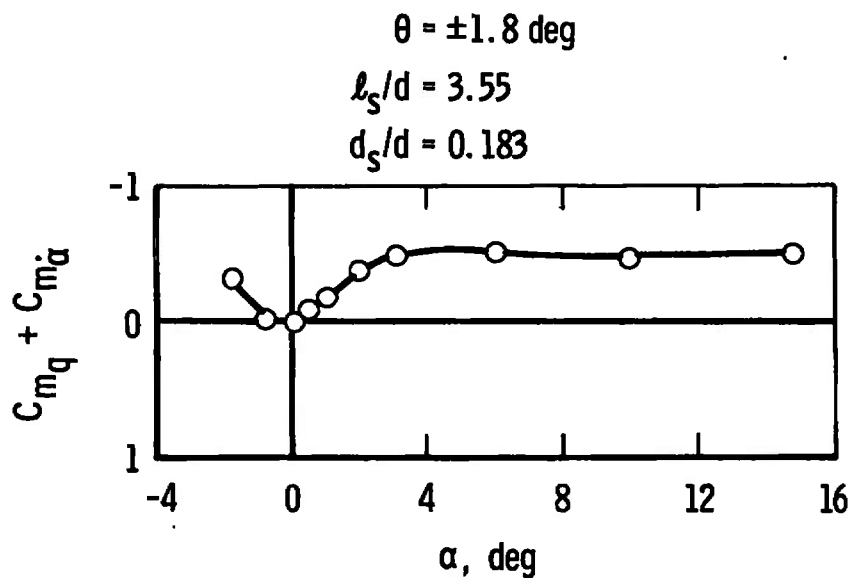


a. $M_\infty = 1.76, \omega d/2V_\infty \approx 0.021$

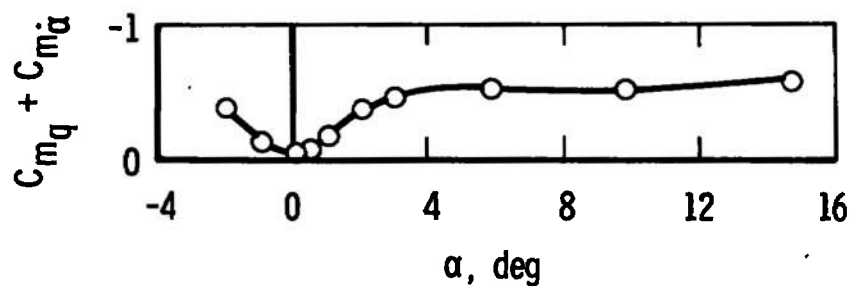


b. $M_\infty = 2.01, \omega d/2V_\infty \approx 0.020$

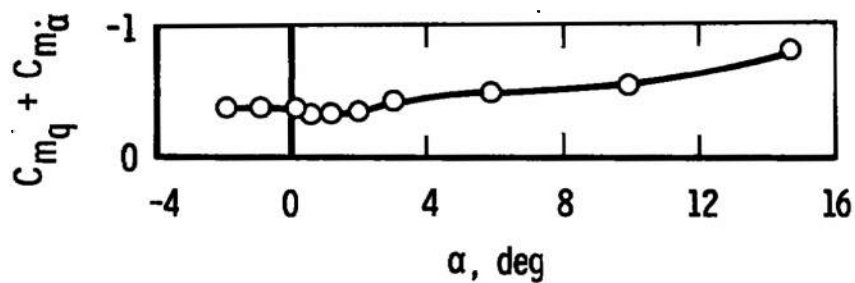
Fig. 30 Damping-in-Pitch Derivatives as a Function of Angle of Attack, Config. 5000, $Re_d \approx 0.75 \times 10^6$



c. $M_\infty = 2.24, \omega d/2V_\infty \approx 0.019$

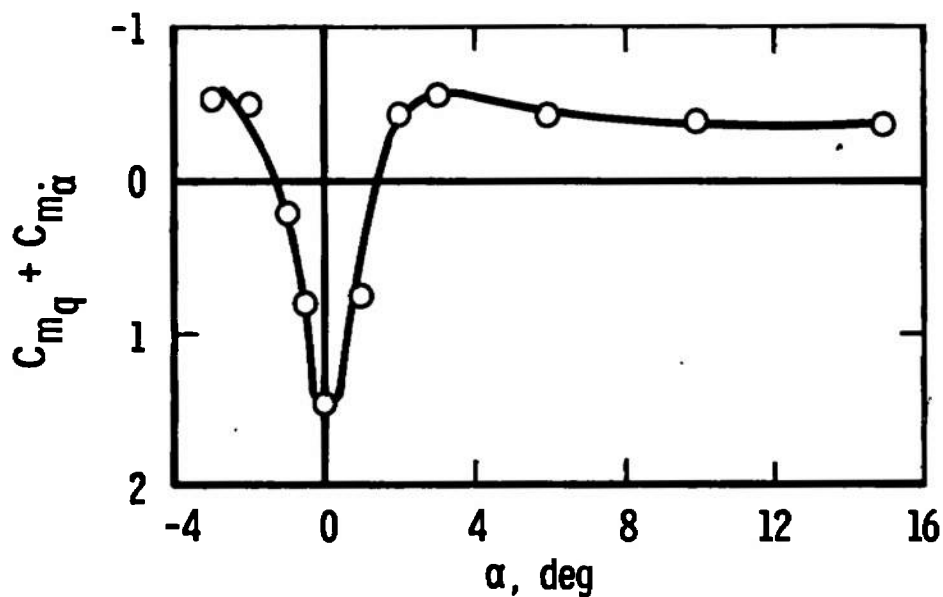


d. $M_\infty = 2.49, \omega d/2V_\infty \approx 0.018$

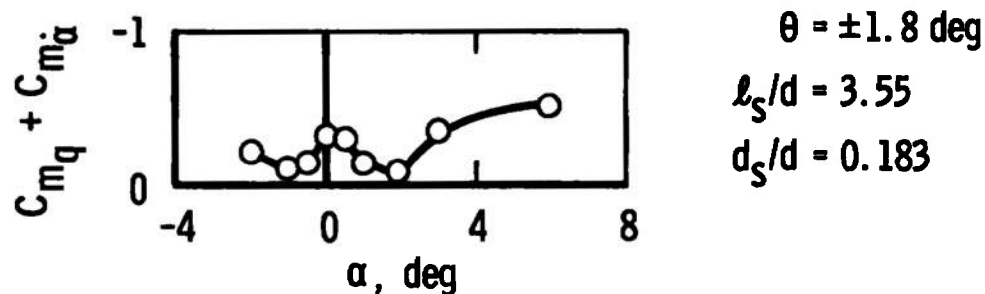


e. $M_\infty = 3.00, \omega d/2V_\infty \approx 0.016$

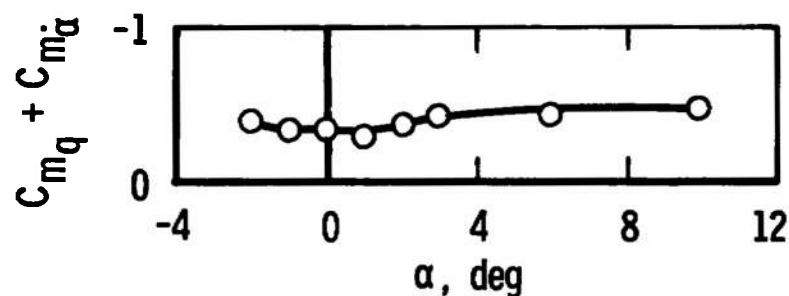
Fig. 30 Concluded



a. $M_\infty = 1.76$, $\omega d/2V_\infty \approx 0.032$

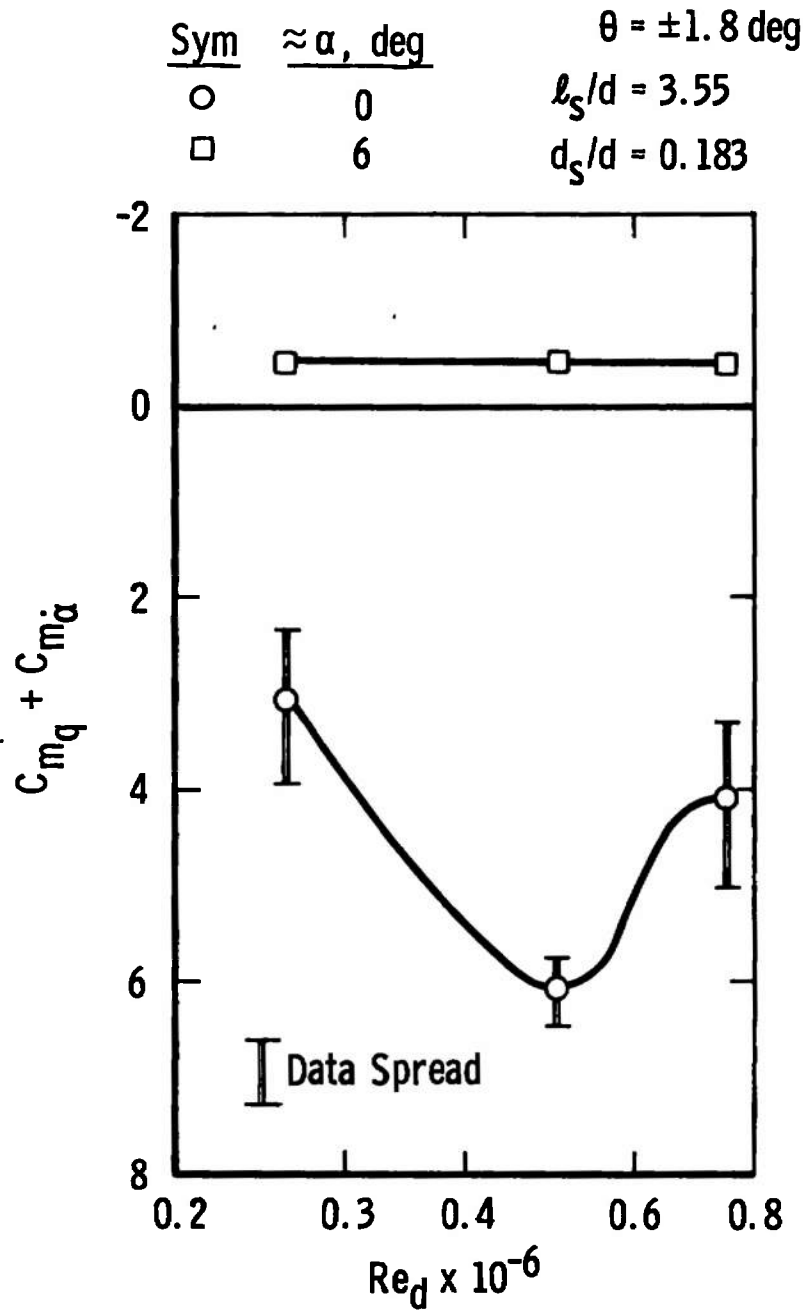


b. $M_\infty = 2.23$, $\omega d/2V_\infty \approx 0.028$



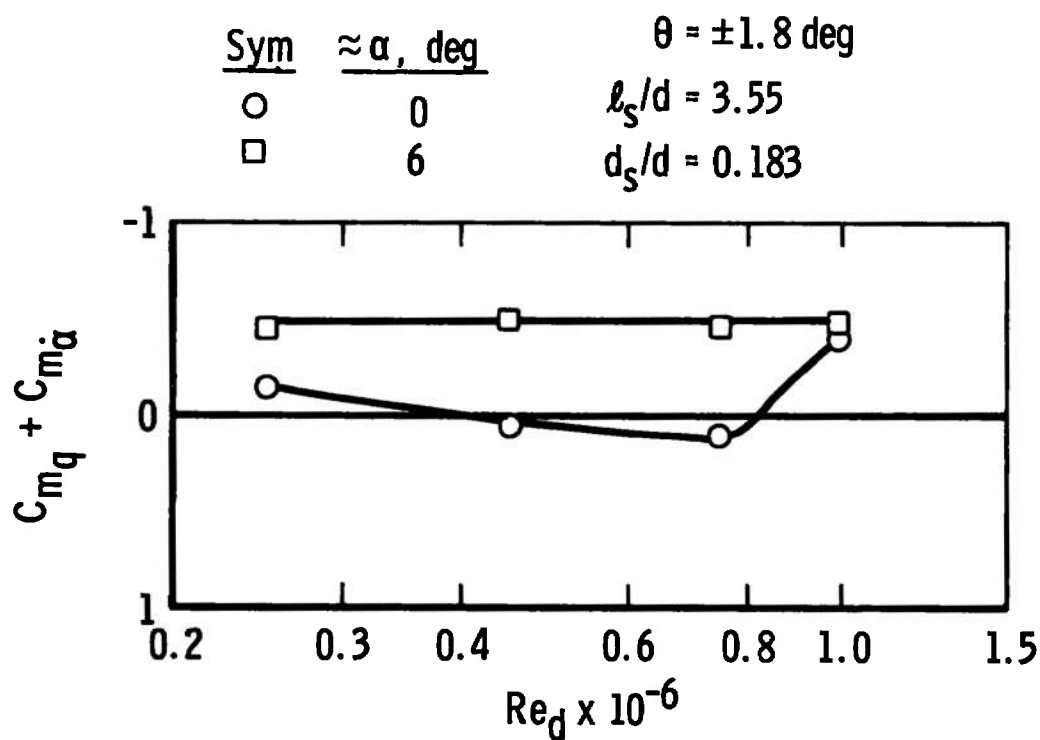
c. $M_\infty = 2.99$, $\omega d/2V_\infty \approx 0.025$

Fig. 31 Damping-in-Pitch Derivatives as a Function of Angle of Attack, Config. 4000, $Re_d \approx 0.26 \times 10^6$

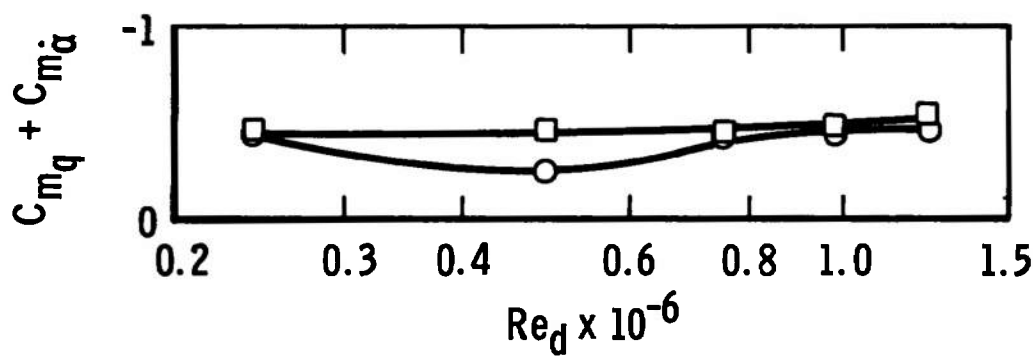


a. $M_\infty = 1.76$, $\omega d/2V_\infty \approx 0.0090$

Fig. 32 Damping-in-Pitch Derivatives as a Function of Reynolds Number, Config. 1000

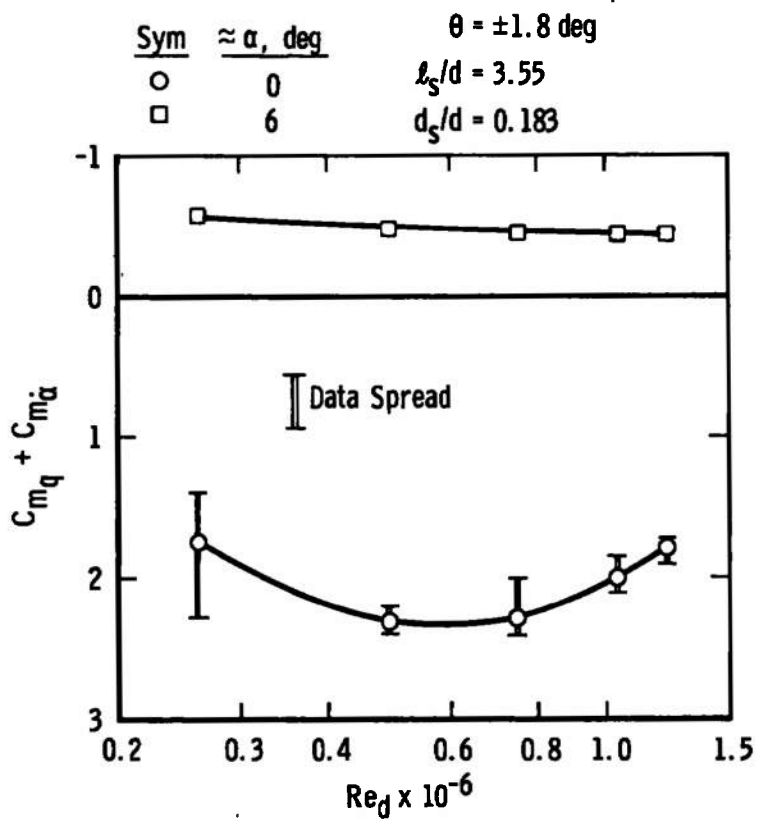


b. $M_\infty \approx 2.50$, $\omega d/2V_\infty \approx 0.0075$

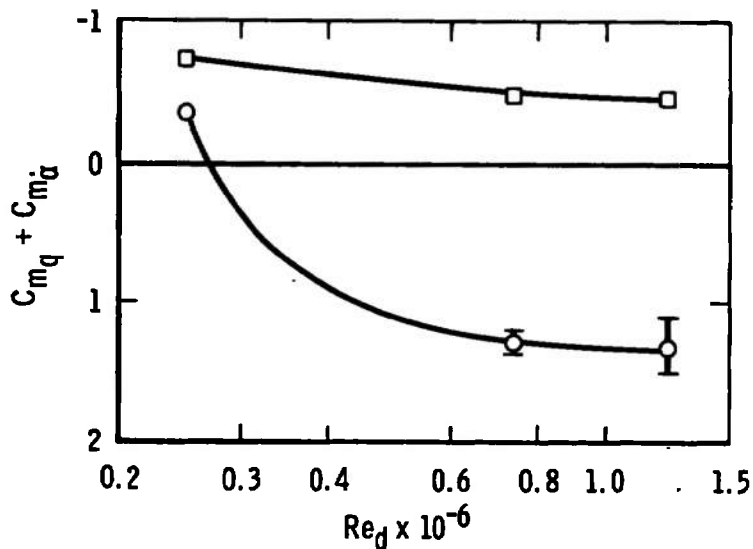


c. $M_\infty \approx 3.00$, $\omega d/2V_\infty \approx 0.0069$

Fig. 32 Concluded

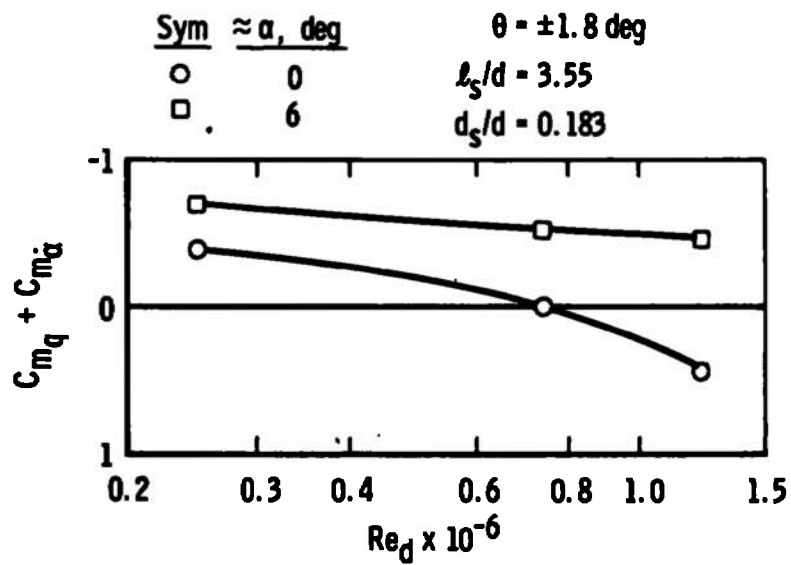


a. $M_\infty = 1.76$, $\omega d/2V_\infty \approx 0.021$

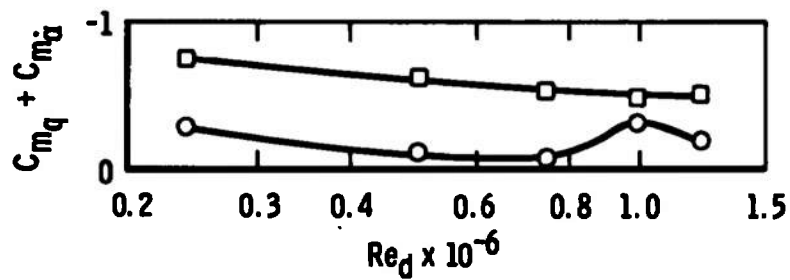


b. $M_\infty \approx 2.00$, $\omega d/2V_\infty \approx 0.020$

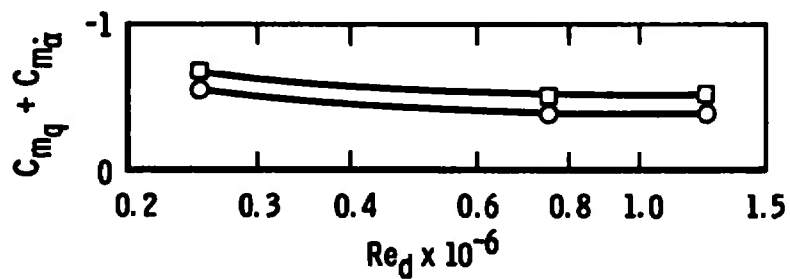
Fig. 33 Damping-in-Pitch Derivatives as a Function of Reynolds Number, Config. 5000



c. $M_\infty \approx 2.24$, $\omega d/2V_\infty \approx 0.019$



d. $M_\infty \approx 2.50$, $\omega d/2V_\infty \approx 0.018$



e. $M_\infty \approx 3.00$, $\omega d/2V_\infty \approx 0.016$

Fig. 33 Concluded

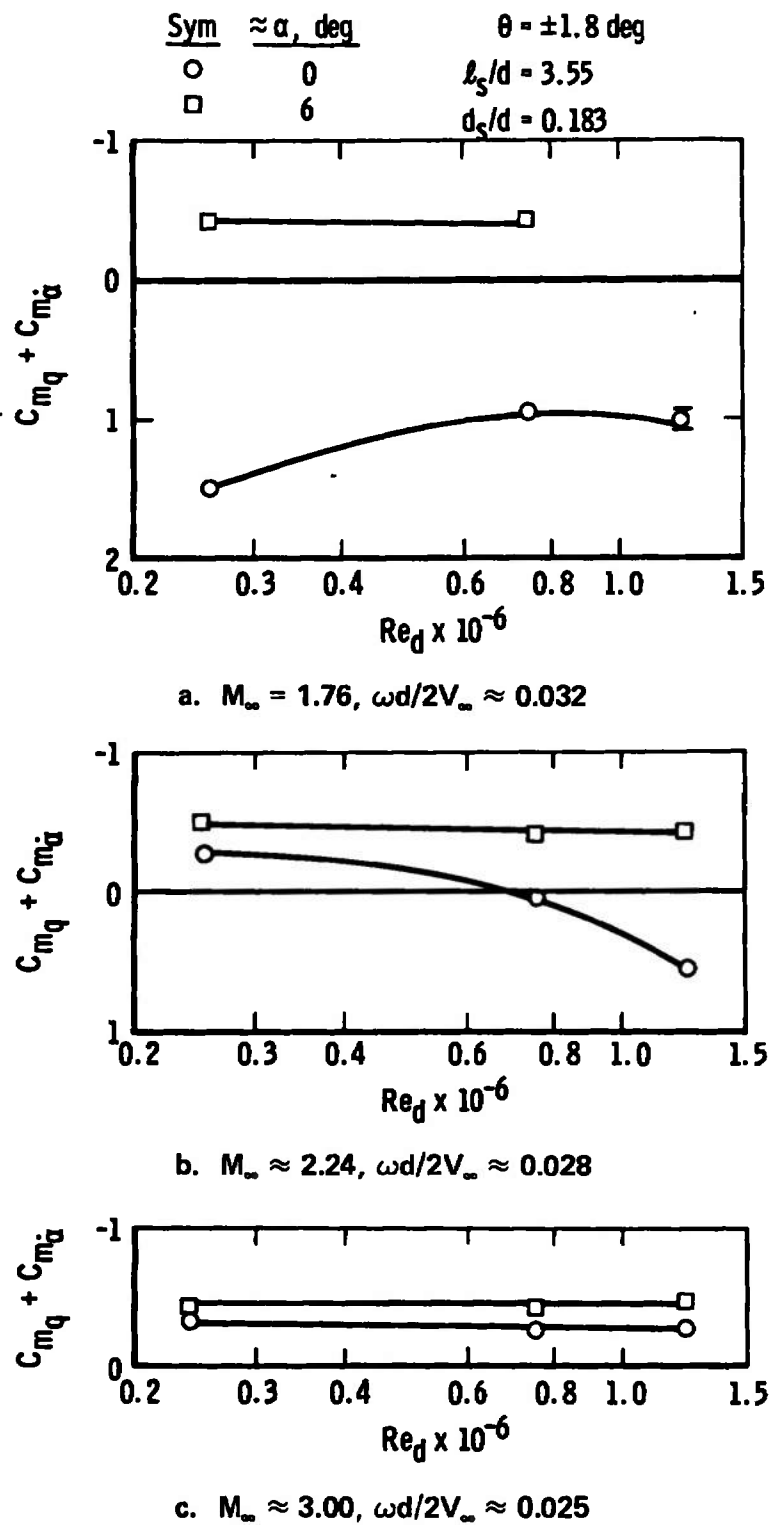
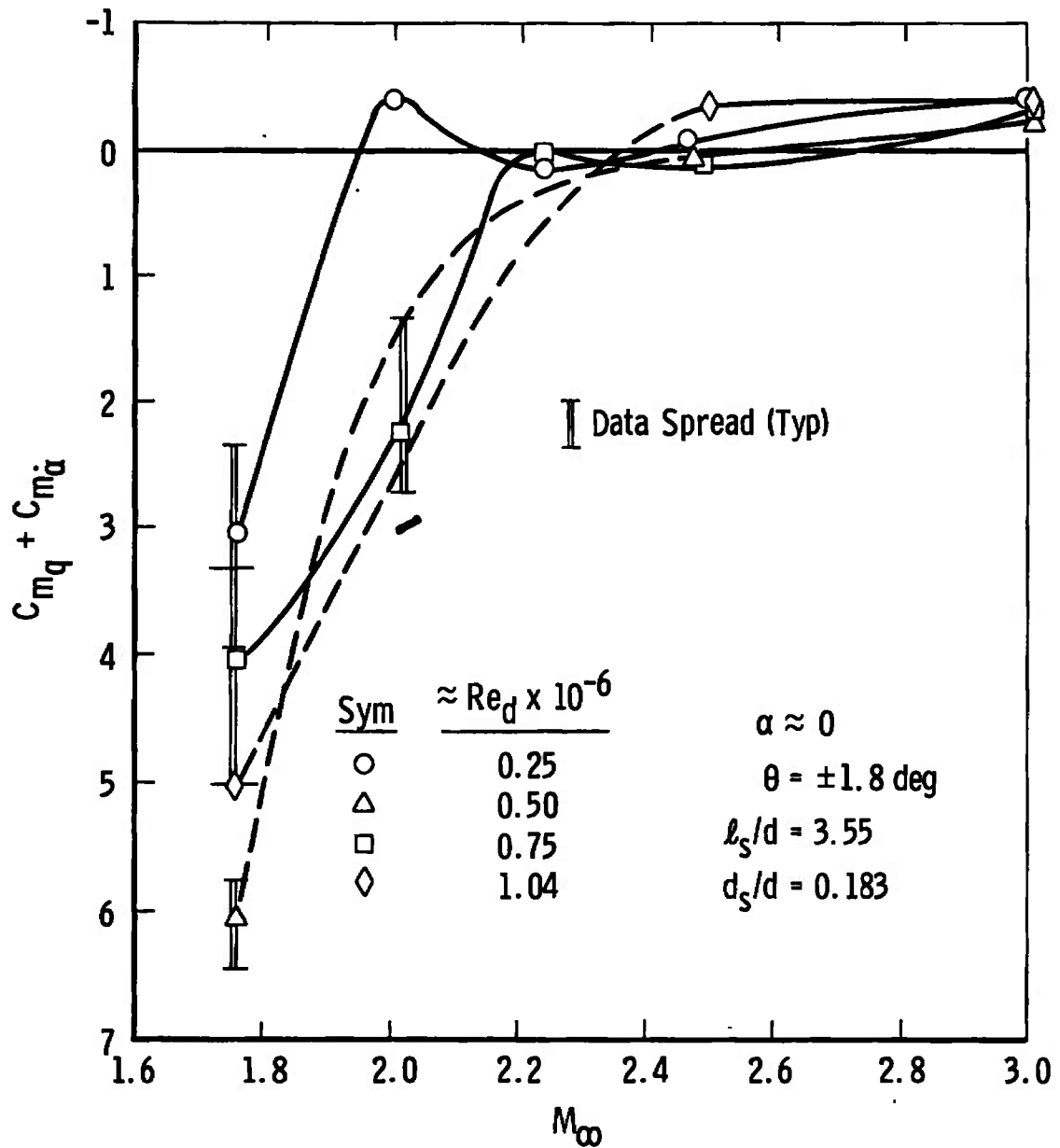


Fig. 34 Damping-in-Pitch Derivatives as a Function of Reynolds Number, Config. 4000



a. Config. 1000, $\omega d/2V_\infty \approx 0.009$ to 0.007

Fig. 35 Damping-in-Pitch Derivatives as a Function of Mach Number

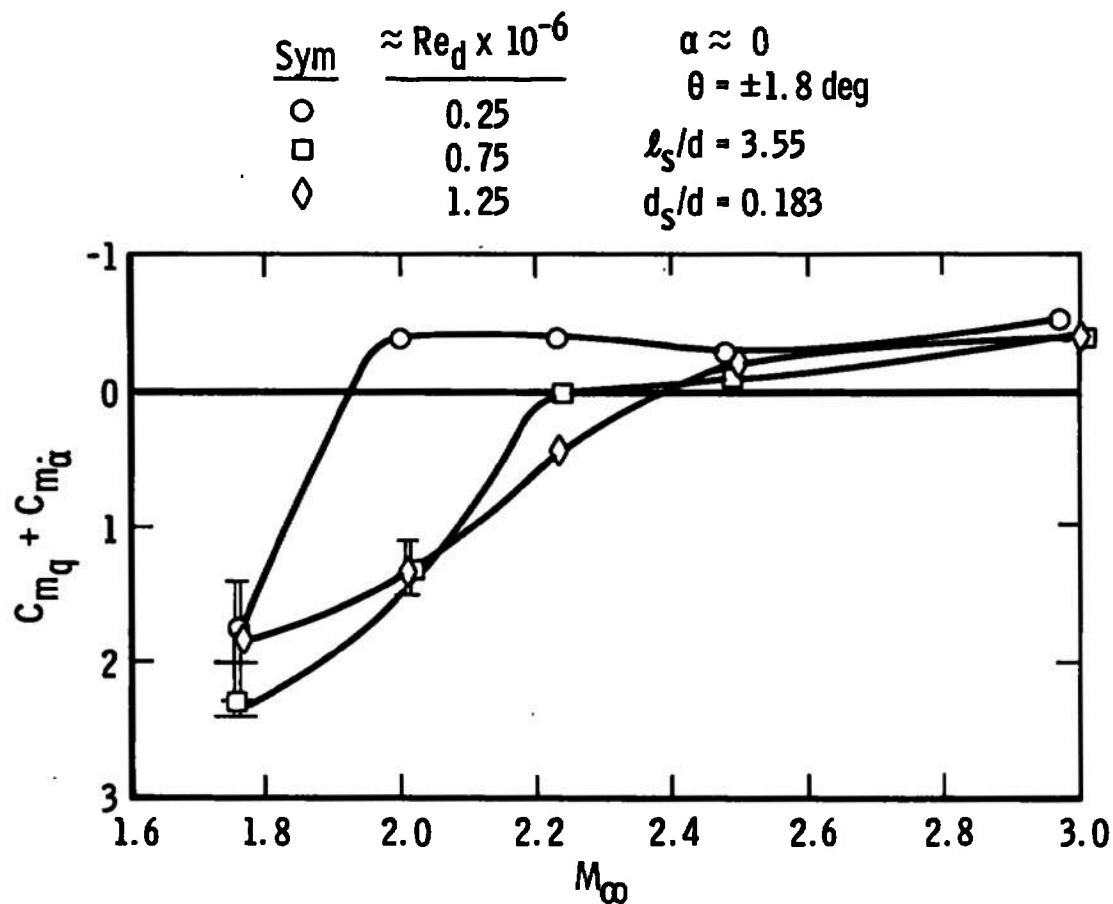
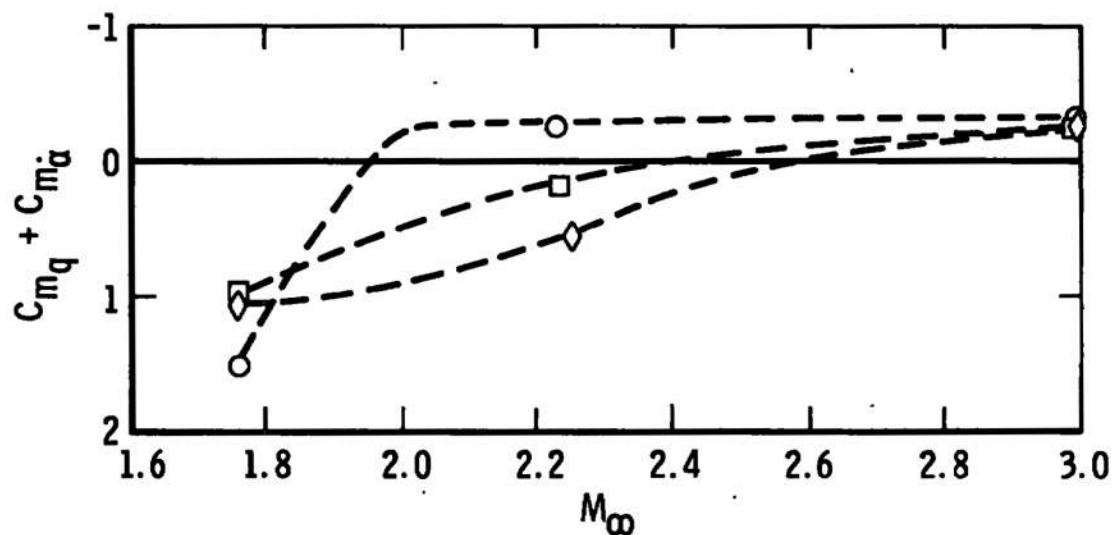
b. Config. 5000, $\omega d/2V_\infty \approx 0.021$ to 0.016 c. Config. 4000, $\omega d/2V_\infty \approx 0.032$ to 0.025

Fig. 35 Concluded

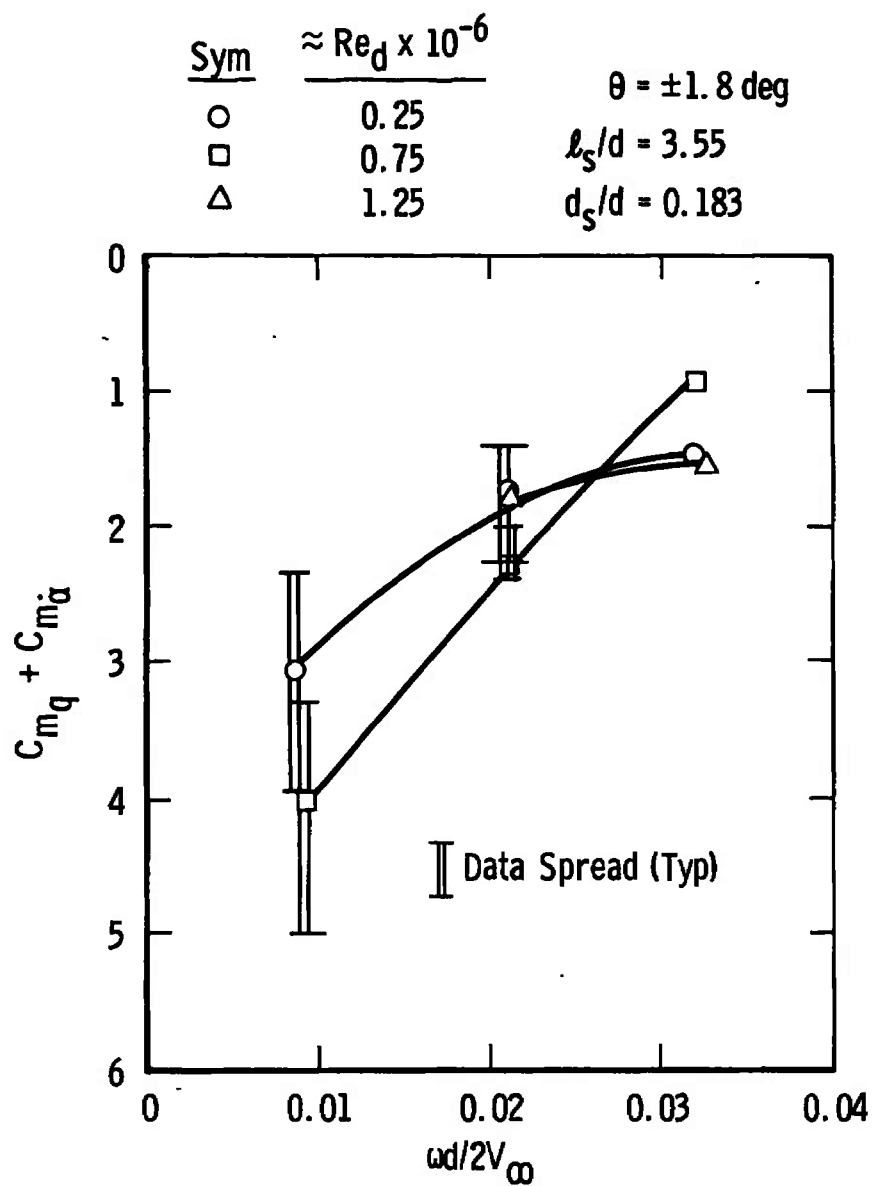
a. $M_{\infty} = 1.76$

Fig. 36 Damping-in-Pitch Derivatives as a Function of Reduced Frequency Parameter, BLDT Config., $\alpha \approx 0$

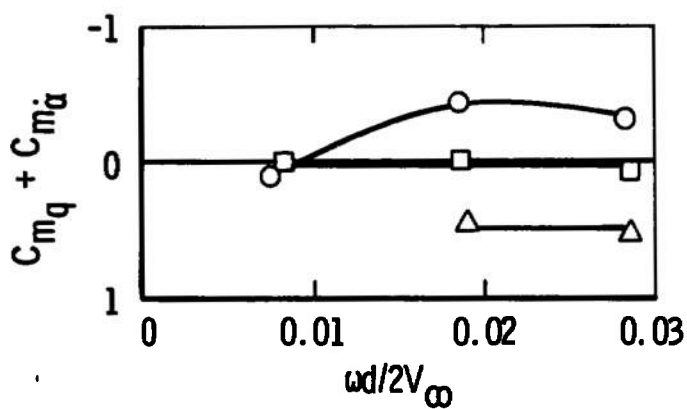
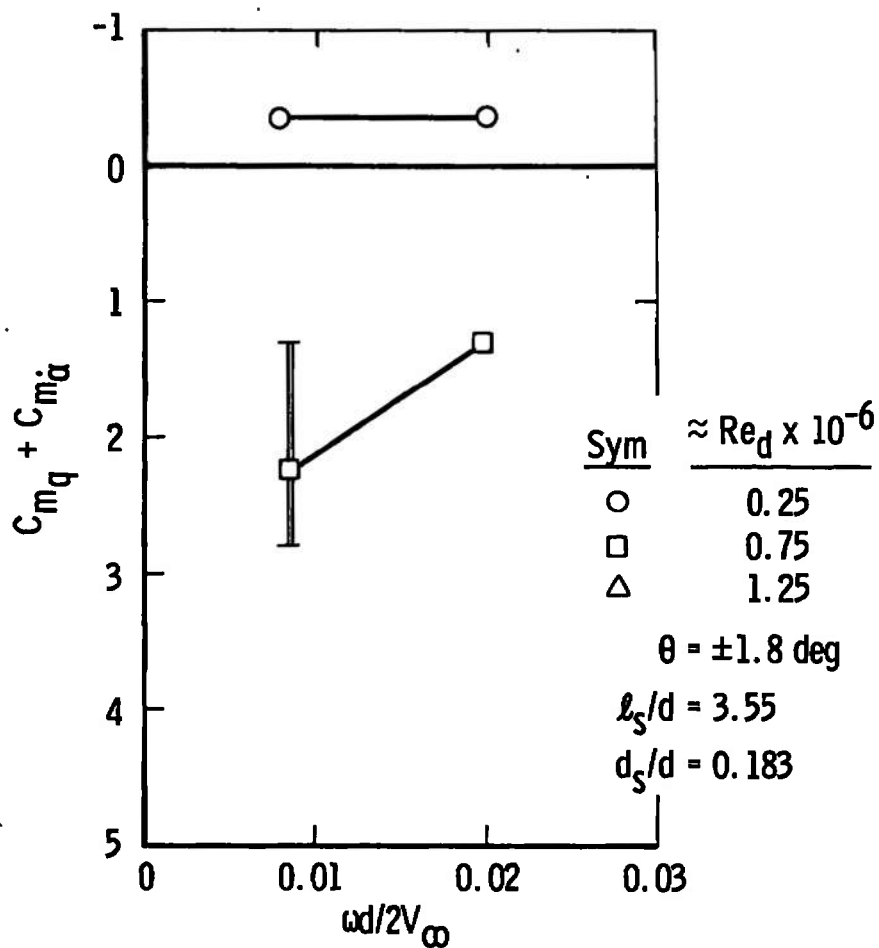
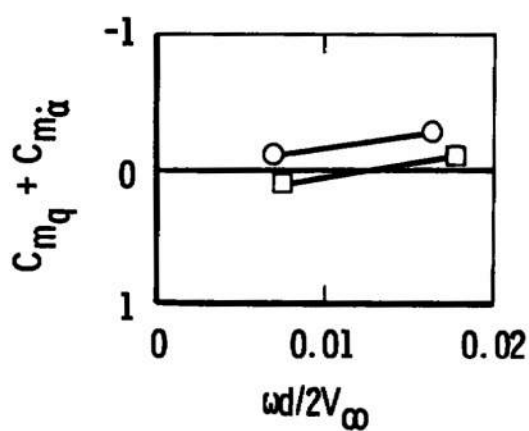
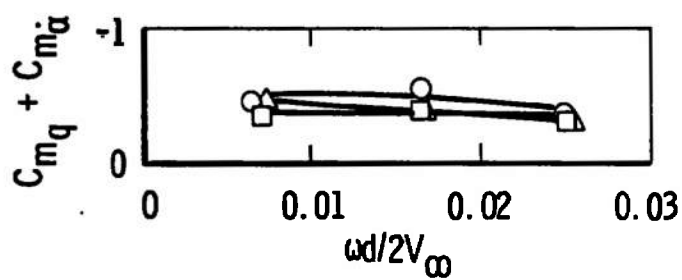


Fig. 36 Continued

Sym	$\approx Re_d \times 10^{-6}$	$\theta = \pm 1.8 \text{ deg}$ $l_s/d = 3.55$ $d_s/d = 0.183$
○	0.25	
□	0.75	
△	1.25	



d. $M_\infty \approx 2.50$



e. $M_\infty \approx 3.00$
Fig. 36 Concluded

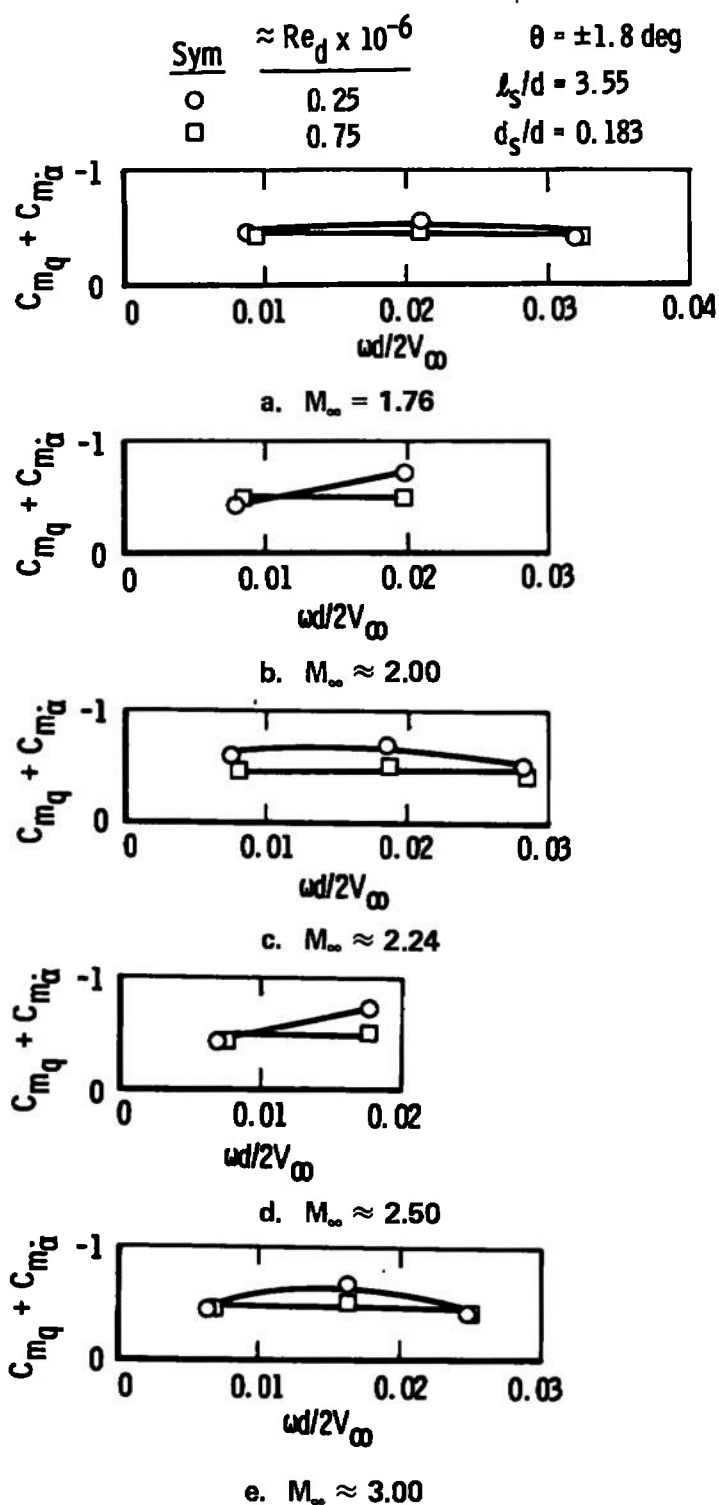
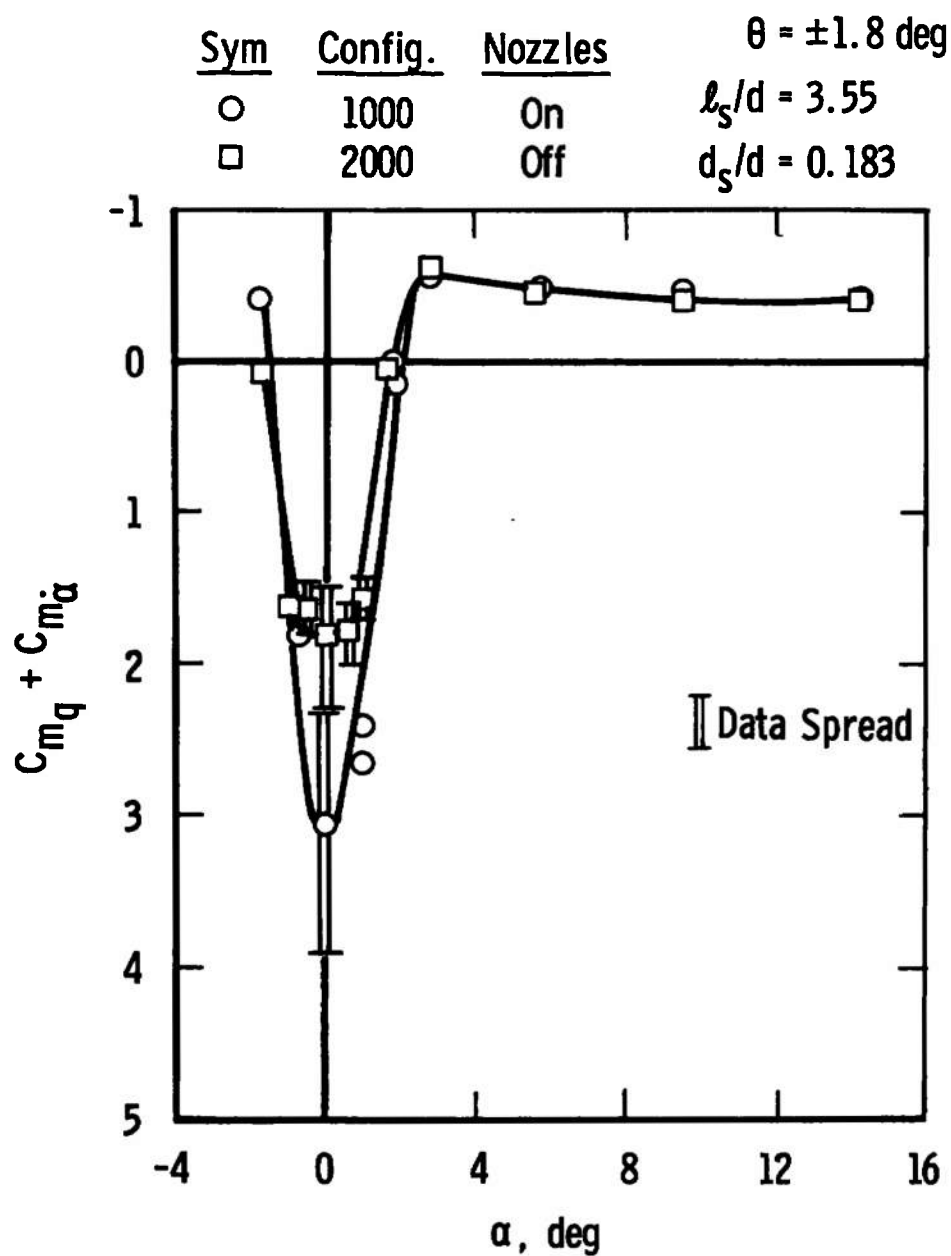
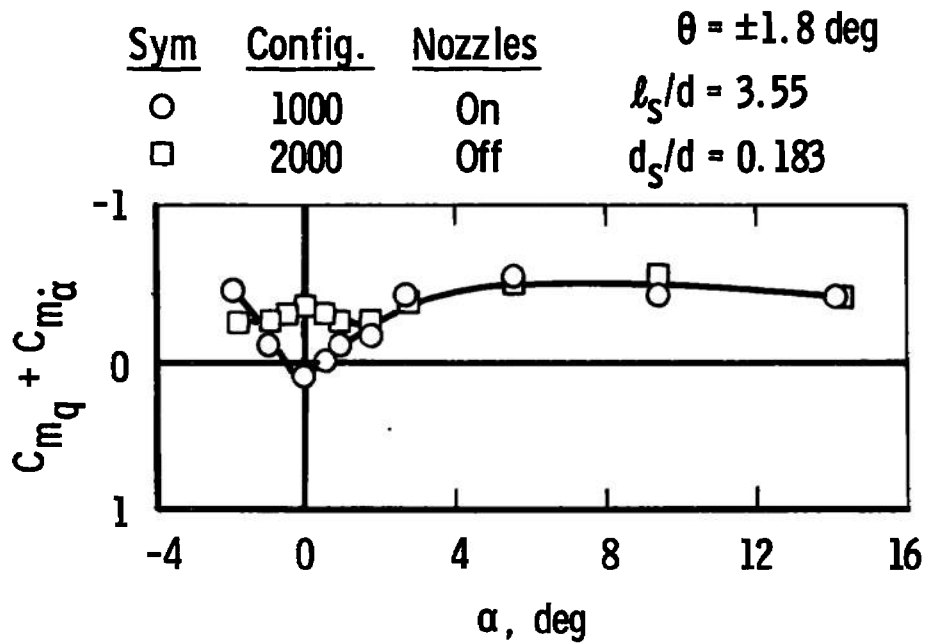


Fig. 37 Damping-in-Pitch Derivatives as a Function of Reduced Frequency Parameter, BLDT Config., $\alpha \approx 6 \text{ deg}$

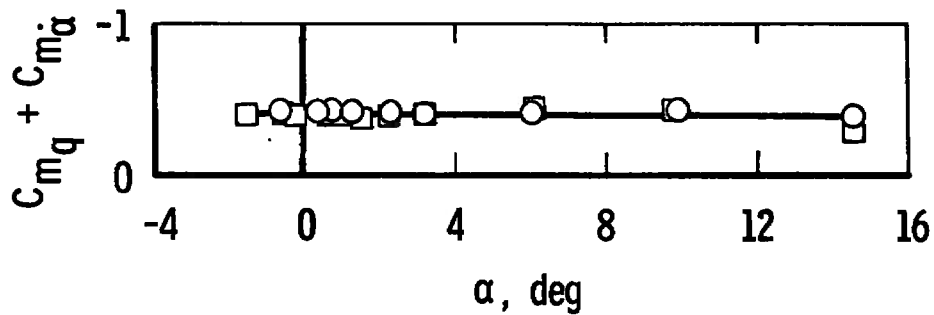


a. $M_\infty = 1.76$, $\omega d/2V_\infty \approx 0.0087$

Fig. 38 Effect of Nozzles on Damping-in-Pitch Derivatives, BLDT Config.,
 $Re_d \approx 0.25 \times 10^6$, $\omega d/2V_\infty \approx 0.007$

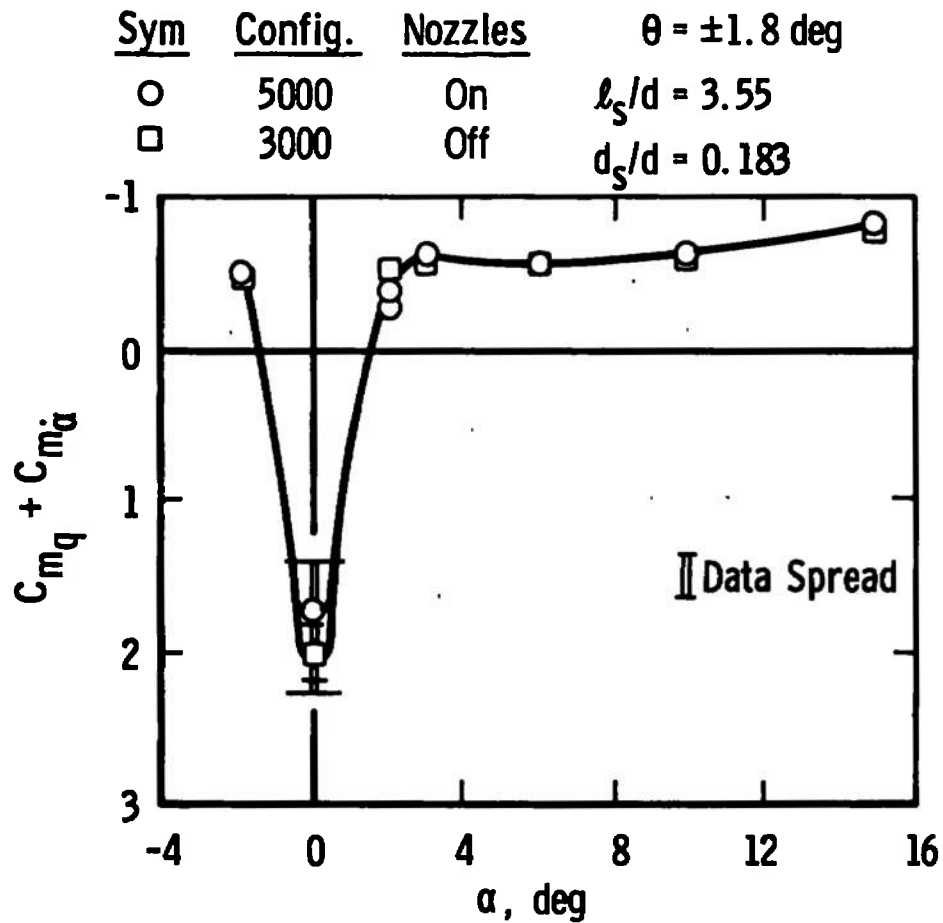


b. $M_\infty = 2.23$, $\omega d/2V_\infty \approx 0.0073$

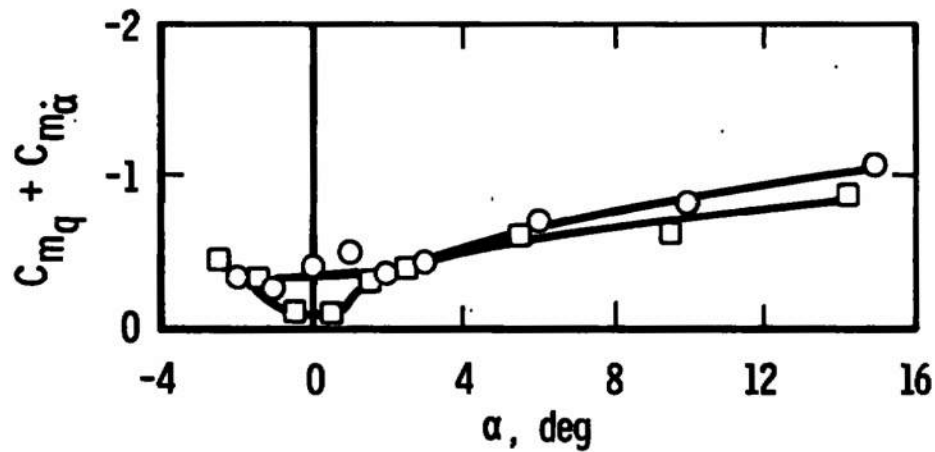


c. $M_\infty = 2.99$, $\omega d/2V_\infty \approx 0.0064$

Fig. 38 Concluded

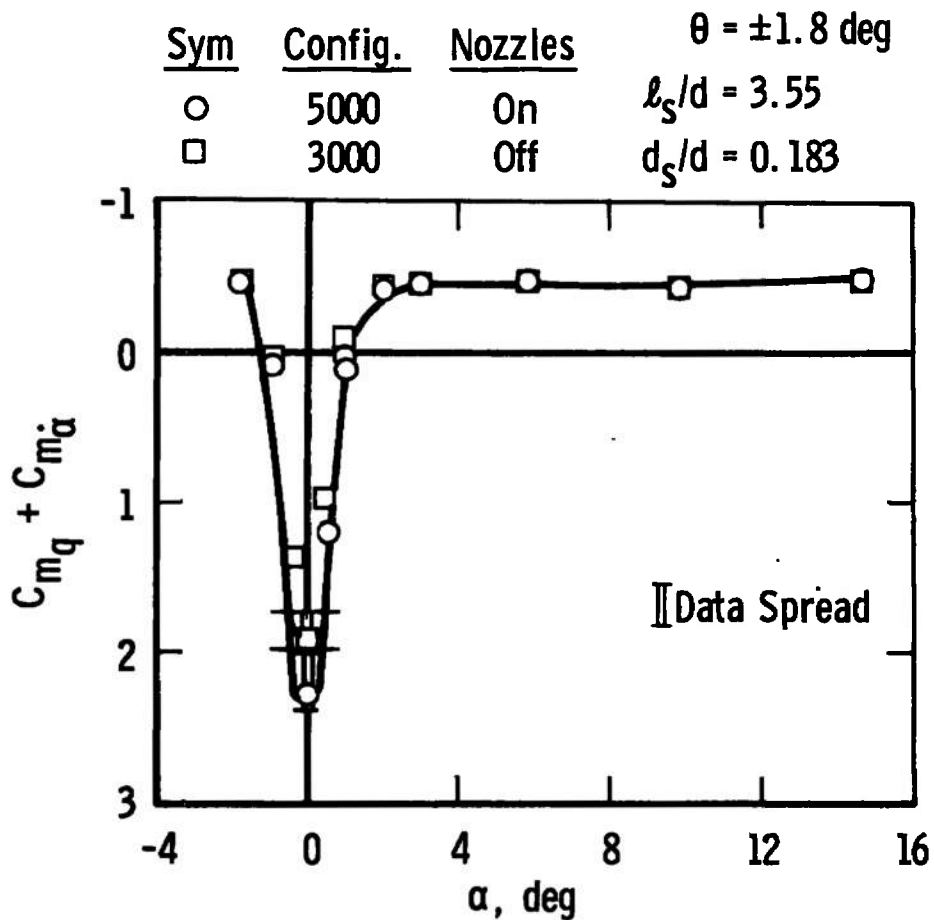


a. $M_\infty = 1.76$, $\omega d/2V_\infty \approx 0.021$

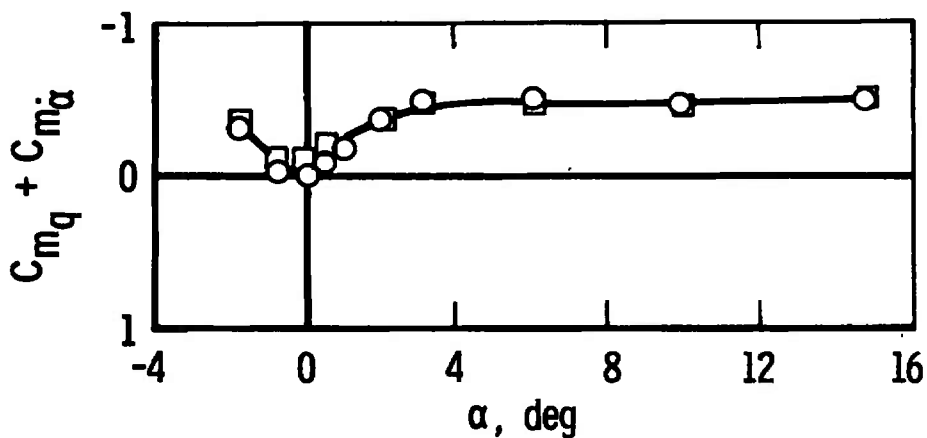


b. $M_\infty = 2.23$, $\omega d/2V_\infty \approx 0.019$

Fig. 39 Effect of Nozzles on Damping-in-Pitch Derivatives, BLDT Config., $Re_d \approx 0.25 \times 10^6$, $\omega d/2V_\infty \approx 0.02$

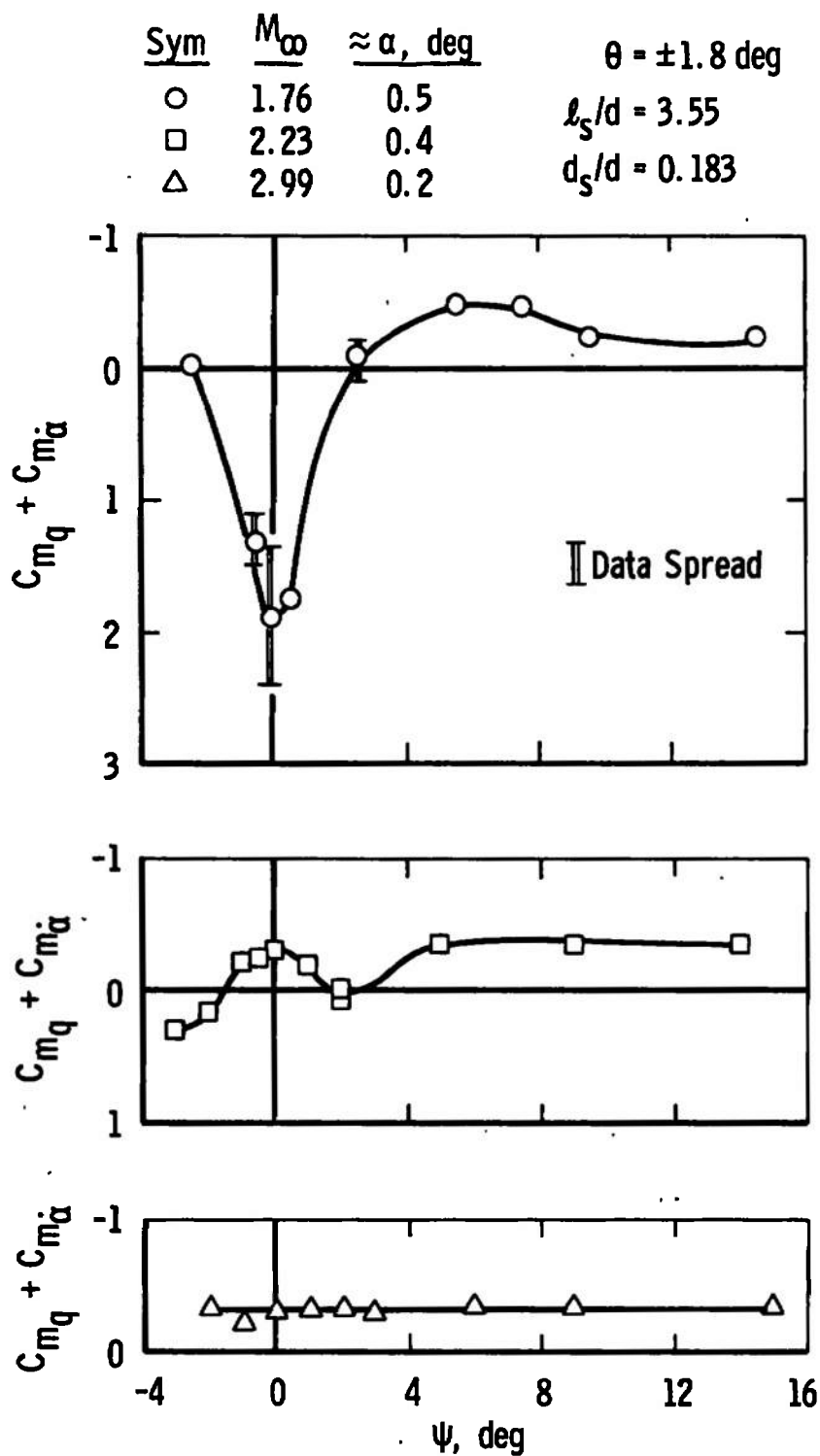


a. $M_\infty = 1.76$, $\omega d/2V_\infty \approx 0.021$

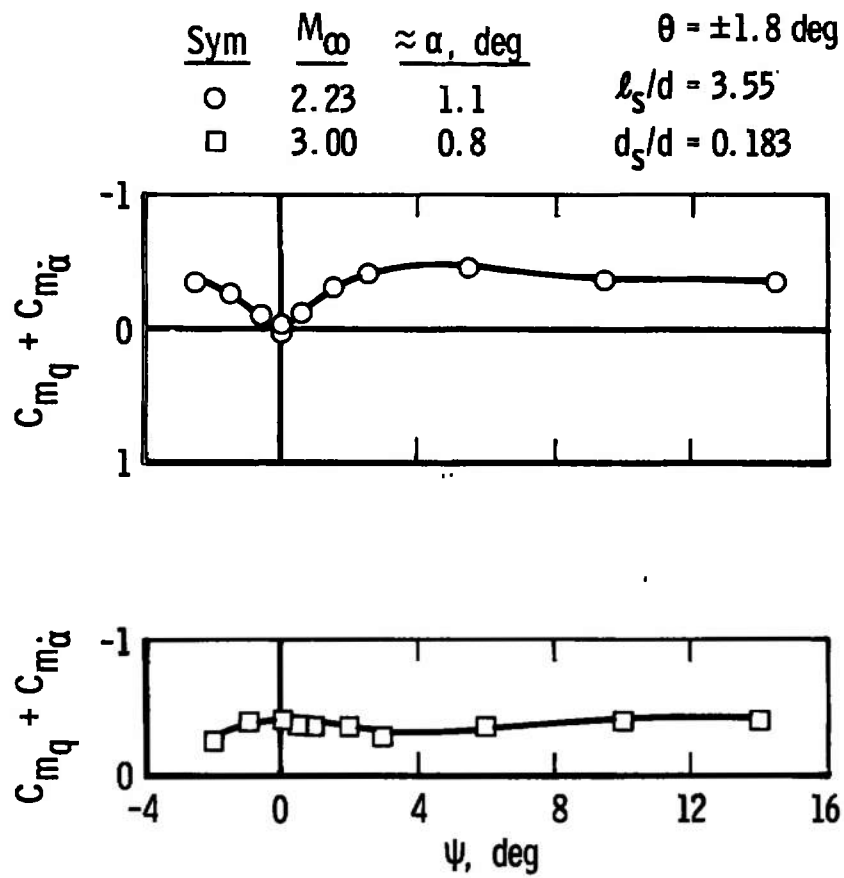


b. $M_\infty = 2.24$, $\omega d/2V_\infty \approx 0.019$

Fig. 40 Effect of Nozzles on Damping-in-Pitch Derivatives, BLDT Config., $Re_d \approx 0.75 \times 10^6$, $\omega d/2V_\infty \approx 0.02$



a. $Re_d \approx 0.26 \times 10^6$
 Fig. 41 Damping-in-Pitch Derivatives as a Function of Yaw Angle,
 BLDT Config. 1090



b. $Re_d \approx 0.75 \times 10^6$
 Fig. 41 Concluded

TABLE I
FREE-FLIGHT DRAG DATA

Group	Model Physical Data				Mach Number		Re _d × 10 ⁻⁶		C _D
	Weight, lb	Nozzles	Z _h , in.	Z _{cg} , in.	Free Stream	Model	Free Stream	Model	
2	0.1398	On	0	0	1.72	1.66	0.248	0.239	1.61
4	0.1385	↓	↓	↓	↓	1.61	0.746	0.699	1.68
7	0.1399	↓	↓	↓	↓	1.59	1.206	1.116	1.39
14	0.1389	↓	↓	↓	↓	1.61	1.002	0.937	1.44
15	0.1435	↓	0.021	0.021	↓	1.64	0.497	0.474	1.49
17	0.1501	↓	0.042	0.042	↓	1.64	0.497	0.474	1.59
18	0.1398	↓	0.034	0	↓	1.59	1.254	1.161	1.37
19	0.1366	↓	0	↓	2.00	1.93	0.258	0.249	1.62
20	0.1389	↓	↓	↓	↓	1.91	0.498	0.476	1.54
21	0.1393	↓	↓	↓	↓	1.88	0.747	0.704	1.73
23	0.1401	↓	↓	↓	2.21	2.15	0.240	0.233	1.58
24	0.1399	↓	↓	↓	↓	2.12	0.485	0.465	1.58
25	0.1383	↓	↓	↓	↓	2.10	0.718	0.684	1.59
26	0.1395	↓	↓	↓	↓	2.08	0.982	0.923	1.60
27	0.1385	↓	↓	↓	↓	2.06	1.222	1.138	1.68
28	0.1413	↓	0.021	0.021	↓	2.11	0.484	0.463	1.73
31	0.1394	↓	0	0	2.49	2.42	0.250	0.243	1.72
32	0.1399	↓	↓	↓	2.50	2.40	0.504	0.483	1.79
34	0.1383	Off	↓	↓	↓	2.40	0.499	0.479	1.74
35	0.1388	On	↓	↓	2.98	2.91	0.256	0.250	1.54
36	0.1387	↓	↓	↓	3.00	2.88	0.767	0.736	1.58

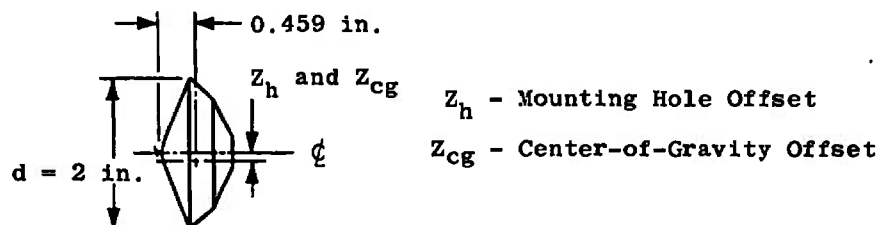


TABLE II
TUNNEL CONDITIONS FOR FREE-FLIGHT TEST

Group	M_∞	$Re_d \times 10^{-6}$	p_O , psia	T_O , °R	q_∞ , psia	V_∞ , ft/sec
2	1.72	0.248	5.01	526	2.04	1531
4	↓	0.746	15.10	527	6.15	1533
7		1.206	24.29	525	9.89	1530
14		1.002	20.18	525	8.21	1530
15		0.497	10.02	525	4.08	1530
17		0.497	10.03	525	4.08	1531
18		1.254	25.30	525	10.30	1531
19	2.00	0.258	5.81	525	2.08	1674
20	↓	0.498	11.21	526	4.01	1674
21		0.747	16.83	526	6.02	1674
23	2.21	0.240	5.93	525	1.87	1764
24	↓	0.485	11.91	523	3.75	1761
25		0.718	17.55	521	5.53	1757
26		0.982	24.15	523	7.60	1761
27		1.222	30.23	525	9.52	1765
28		0.484	11.99	526	3.77	1766
31	2.49	0.250	7.14	527	1.84	1871
32	2.50	0.504	14.22	521	3.64	1864
34	2.50	0.499	14.19	524	3.63	1869
35	2.98	0.256	9.31	524	1.62	2006
36	3.00	0.767	28.10	523	4.82	2008

TABLE III
DYNAMIC STABILITY TEST SUMMARY

<u>Configuration</u>	<u>Schedule</u> (See Table IV)	<u>$\approx \omega d / 2V_{\infty} \times 10^2$</u>	<u>$\approx \alpha$, deg</u>
721M ↓	A2†	3.64	-3.0 to 9.2
	A4†	3.67	-3.0 to 9.2
	A7†	3.70	-3.0 to 9.1
	B2†	3.39	-3.0 to 9.7
	B3†	3.40	-3.0 to 9.6
	C2	3.20	-3.0 to 9.8
	C4	3.23	-3.0 to 9.6
	C6	3.23	-3.0 to 9.5
	C8†	3.26	-3.0 to 5.5
	E1†	2.91	-3.0 to 9.8
	E2†	2.92	-3.0 to 9.7
	E3†	2.95	-3.0 to 9.5
	E4†	2.96	-3.1 to 7.4
1000 ↓	A1	0.85	-1.8 to 14.2
	A3†	0.87	-1.6 to 13.8
	A5	0.91	-1.5 to 13.2
	A6†	0.95	0 to 12.9
	A8*	0.98	0 to 12.7
	B1	0.77	-0.9 to 15.2
	B4	0.84	-0.4 to 13.5
	B5*	0.91	2.0 to 13.9
	C1	0.73	-2.0 to 14.1
	C5	0.80	0.4 to 14.2
	C7*	0.85	1.5 to 13.9
	D1	0.70	-1.9 to 14.2
	D2†	0.73	-1.0 to 14.5
	D3	0.76	-1.3 to 13.6
	D4†	0.78	-0.8 to 13.5
	F1	0.64	-0.5 to 14.6
	F2†	0.66	-1.0 to 14.5
	F3†	0.69	-0.8 to 14.4
	F4†	0.71	-0.5 to 14.2
	F5†	0.73	0.6 to 14.0

†Portions of data presented.

*Data not presented.

Note: $\pm \theta$ range ≈ 0.6 to 2.4 deg

TABLE III (Continued)

Configuration	Schedule (See Table IV)	$\approx \omega d / 2V_{\infty} \times 10^2$	$\approx \alpha$, deg
1045	A1*	0.84	-1.6 to 2.2
↓	C1*	0.74	-1.6 to 14.8
	F1*	0.64	-1.7 to 14.8
1090	A1*	0.86	-2.5 to 14.4
↓	A5*	0.92	-3.5 to 14.4
	A8*	1.00	-3.5 to 14.4
	C1*	0.74	-3.0 to 14.0
	C5*	0.81	-2.5 to 14.4
	C7*	0.86	-2.6 to 14.4
	F1*	0.64	-2.0 to 15.0
	F3*	0.69	-2.0 to 15.0
	F5*	0.74	-2.0 to 15.0
2000	A1	0.85	-1.9 to 14.1
↓	C1	0.74	-1.9 to 14.1
	C7*	0.85	0.4 to 13.8
	F1	0.64	-1.5 to 14.6
2300	A1	0.84	-1.9 to 14.1
↓	A5*	0.92	-1.5 to 13.2
	A8*	0.98	1.8 to 6.3
	C1†	0.74	-2.4 to 13.6
	C5†	0.80	-0.8 to 13.9
	C7†	0.85	0 to 13.3
	F1†	0.64	-1.5 to 14.6
	F5†	0.73	-0.4 to 14.0
2301	A5*	0.91	-2.1 to 5.5
2302	A5*	0.91	-1.2 to 13.5
2700	A1	0.84	-1.9 to 14.1
↓	A3*	0.89	-1.0 to 6.0
	A5†	0.92	-0.6 to 13.5
	A8†	1.00	0 to 13.7
	C1†	0.74	-1.5 to 14.6
	C5†	0.80	-0.5 to 14.5
	C7*	0.86	0.8 to 13.8
	F1†	0.64	-1.5 to 14.6
	F3†	0.69	-0.8 to 14.3
	F5†	0.74	-0.3 to 14.0

TABLE III (Continued)

Configuration	Schedule (See Table IV)	$\approx \omega d / 2V_\infty \times 10^2$	$\approx \alpha$, deg
2900 ↓	A1	0.85	-1.9 to 14.1
	A5†	0.92	-1.8 to 13.1
	A8*	0.99	-1.5 to 12.1
	C1†	0.73	-0.5 to 14.1
	C5†	0.80	-1.5 to 13.8
	C7*	0.87	-1.0 to 12.9
	F1†	0.64	-1.5 to 14.6
	F3†	0.69	-0.7 to 14.2
	F5†	0.73	-0.4 to 14.0
3000 ↓	A1	2.11	-2.0 to 14.9
	A5	2.15	-1.9 to 14.6
	A8*	2.16	-1.7 to 14.6
	C1	1.86	-2.5 to 14.4
	C5	1.89	-1.7 to 14.7
	C7*	1.90	-1.7 to 14.6
3100 ↓	A1*	2.12	-1.9 to 14.9
	A5*	2.14	-1.8 to 14.7
	A8*	2.17	-1.6 to 14.5
3300 ↓	A1	2.13	-1.9 to 14.9
	A5†	2.14	-1.8 to 14.7
	A8†	2.16	-1.6 to 14.6
3400 ↓	A1†	2.12	0 to 9.9
	A8†	2.16	0.2 to 14.6
	C7†	1.90	-1.6 to 14.6
3600	A1*	2.12	0
3700 ↓	A1	2.12	-2.0 to 14.8
	A5†	2.14	-1.9 to 14.7
	A8†	2.17	-2.6 to 14.6
	C1†	1.86	-1.9 to 15.0
3900 ↓	A1	2.12	-2.0 to 14.8
	A5†	2.15	-1.8 to 14.7
	A8†	2.17	-1.7 to 14.5
	C1†	1.86	-1.9 to 14.9
	C5*	1.88	-1.8 to 14.7
	C7*	1.90	-2.1 to 14.1

TABLE III (Concluded)

Configuration	Schedule (See Table IV)	$\approx \omega d / 2V_{\infty} \times 10^2$	$\approx \alpha$, deg
4000 ↓	A1	3.22	-3.0 to 14.9
	A5†	3.25	-1.9 to 5.9
	A8†	3.27	-2.0 to 1.9
	C1	2.82	-2.0 to 5.9
	C5†	2.84	-1.9 to 5.9
	C7†	2.85	-1.9 to 5.9
	F1	2.48	-2.0 to 9.9
	F3†	2.49	-1.9 to 5.9
	F5†	2.50	-1.9 to 5.9
5000 ↓	A1	2.12	-1.9 to 14.9
	A3†	2.12	-1.9 to 5.9
	A5	2.13	-1.7 to 14.7
	A6†	2.15	-1.7 to 5.9
	A8†	2.16	-1.7 to 14.6
	B1	1.96	-1.9 to 14.8
	B4	1.98	-1.8 to 14.7
	B5†	2.00	-1.6 to 14.6
	C1	1.85	-1.9 to 14.9
	C5	1.87	-1.8 to 14.7
	C7†	1.88	-1.6 to 14.6
	D1	1.76	-1.9 to 14.9
	D2†	1.77	-1.9 to 5.9
	D3	1.77	-1.9 to 14.7
	D4†	1.78	-1.9 to 5.9
	D5†	1.80	-1.7 to 14.6
	F1	1.64	-1.9 to 14.9
	F3	1.64	-1.8 to 14.8
	F5†	1.66	-1.7 to 9.8
6700 ↓	A1	3.22	-2.0 to 5.9
	A5†	3.25	-2.9 to 14.7
	A8†	3.28	-1.9 to 5.9
	C5†	2.85	-4.9 to 5.9
	F1†	2.49	-2.0 to 5.9
	F5†	2.51	0 to 5.9
6900	A5†	3.25	-2.9 to 14.8
6900	A8†	3.28	-1.9 to 5.9

TABLE IV
TUNNEL CONDITIONS FOR DYNAMIC STABILITY TEST

<u>Schedule</u>	<u>M_∞</u>	<u>Re_d x 10⁻⁶</u>	<u>p₀, psia</u>	<u>T₀, °R</u>	<u>q_∞, psia</u>	<u>V_∞, ft/sec</u>
A1	1.76	0.26	1.95	560	0.78	1604
A2		0.42	3.17	562	1.27	1607
A3		0.49	3.66	562	1.47	1607
A4		0.68	5.06	560	2.03	1604
A5		0.75	5.58	560	2.23	1604
A6		1.05	7.82	560	3.13	1604
A7		1.09	8.12	560	3.25	1604
A8		1.24	9.29	561	3.72	1606
B1	2.00	0.25	2.05	561	0.73	1731
B2		0.43	3.53	560	1.26	1729
B3	2.01	0.69	5.69	560	2.02	1734
B4		0.75	6.20	561	2.20	1736
B5	2.02	1.23	10.22	562	3.61	1742
C1	2.23	0.25	2.29	562	0.71	1835
C2		0.43	3.93	561	1.22	1833
C3		0.54	4.98	560	1.54	1832
C4		0.71	6.48	560	2.01	1832
C5		0.75	6.89	562	2.14	1835
C6	2.25	1.10	10.21	562	3.12	1843
C7		1.22	11.39	563	3.49	1845
C8		1.49	13.78	561	4.22	1842
D1	2.46	0.25	2.58	559	0.68	1918
D2	2.47	0.50	5.17	561	1.35	1925
D3	2.48	0.75	7.75	560	2.01	1926
D4	2.49	1.01	10.49	561	2.70	1932
D5	2.50	1.25	13.09	561	3.35	1935
E1	2.75	0.43	5.15	561	1.08	2014
E2		0.70	8.31	561	1.75	2014
E3		1.10	13.07	560	2.75	2013
E4		1.48	17.68	562	3.72	2016
F1	2.99	0.25	3.38	566	0.58	2088
F2	3.00	0.49	6.79	567	1.16	2093
F3		0.74	10.23	567	1.75	2093
F4		0.98	13.55	567	2.32	2093
F5	3.01	1.24	17.12	565	2.91	2091

UNCLASSIFIED

Security Classification

DOCUMENT CONTROL DATA - R & D

(Security classification of title, body of abstract and indexing annotation must be entered when the overall report is classified)

1. ORIGINATING ACTIVITY (Corporate author) Arnold Engineering Development Center Arnold Air Force Station, Tennessee 37389		2a. REPORT SECURITY CLASSIFICATION UNCLASSIFIED	
		2b. GROUP N/A	
3. REPORT TITLE DAMPING-IN-PITCH AND DRAG CHARACTERISTICS OF THE VIKING CONFIGURATION AT MACH NUMBERS FROM 1.6 THROUGH 3			
4. DESCRIPTIVE NOTES (Type of report and inclusive dates) Final Report - June 21 to August 18, 1971			
5. AUTHOR(S) (First name, middle initial, last name) Bob L. Uselton and Arthur R. Wallace, ARO, Inc.			
6. REPORT DATE May 1972		7a. TOTAL NO. OF PAGES 104	7b. NO. OF REFS 19
8a. CONTRACT OR GRANT NO.		9a. ORIGINATOR'S REPORT NUMBER(S) AEDC-TR-72-56	
b. PROJECT NO.		9b. OTHER REPORT NO(S) (Any other numbers that may be assigned this report) ARO-VKF-TR-72-10	
c. Program Element 921E-5			
d.			
10. DISTRIBUTION STATEMENT Approved for public release; distribution unlimited.			
11. SUPPLEMENTARY NOTES Available in DDC.		12. SPONSORING MILITARY ACTIVITY NASA, Langley Research Center, Langley AFB, VA 32265	
13. ABSTRACT Wind tunnel tests were conducted to substantiate earlier test results from another AEDC facility and to determine the dynamic stability characteristics of the Viking-Balloon Launched Decelerator Test (BLDT) configuration. Measurements were made as the model oscillated from ± 2.4 to ± 0.6 deg at angles of attack ranging from -3.5 to 15.2 deg. Data were obtained at nominal free-stream Mach numbers from 1.76 to 3 at free-stream Reynolds number, based on maximum model diameter, ranging from 0.25×10^6 to 1.49×10^6 . The dynamic instabilities at zero angle of attack which were found during the previous tests were verified by the present tests. For angles of attack of 3 to 15 deg at all Mach numbers, the BLDT configuration was dynamically stable, and the damping derivatives were generally independent of the test variables. Free-flight drag coefficients show good agreement with coefficients obtained from tests on a similar configuration with a sting-supported model.			

UNCLASSIFIED

Security Classification

14.	KEY WORDS	LINK A		LINK B		LINK C	
		ROLE	WT	ROLE	WT	ROLE	WT
	VIKING spacecraft						
	Mars (planet)						
	Unmanned spacecraft						
	Scientific spacecraft						
	Aerodynamic stability						
	Supersonic flow						
	Wind tunnel tests						
	Drag						
	Aerodynamic damping						

UNCLASSIFIED

Security Classification